creative commons

COMMONS DEED

저작자표시-비영리-변경금지 2.0 대한민국

이용자는 아래의 조건을 따르는 경우에 한하여 자유롭게

- 이 저작물을 복제, 배포, 전송, 전시, 공연 및 방송할 수 있습니다.

다음과 같은 조건을 따라야 합니다:

저작자표시. 귀하는 원저작자를 표시하여야 합니다.

비영리. 귀하는 이 저작물을 영리 목적으로 이용할 수 없습니다.

변경금지. 귀하는 이 저작물을 개작, 변형 또는 가공할 수 없습니다.

- 귀하는, 이 저작물의 재이용이나 배포의 경우, 이 저작물에 적용된 이용허락조건을 명확하게 나타내어야 합니다.
- 저작권자로부터 별도의 허가를 받으면 이러한 조건들은 적용되지 않습니다.

저작권법에 따른 이용자의 권리는 위의 내용에 의하여 영향을 받지 않습니다.

이것은 이용허락규약(Legal Code)을 이해하기 쉽게 요약한 것입니다.

Disclaimer

dCollection

이학박사 학위논문

Topological phases in quasi-one-dimensional bismuth halides Bi_4X_4 (X= I, Br)

준일차원 비스무트 할라이드 Bi_4X_4 (X= I, Br)의 위상적 상

2022년 8월

서울대학교 대학원

물리천문학부

윤 치 호

Topological phases in quasi-one-dimensional bismuth halides Bi_4X_4 (X= I, Br)

준일차원 비스무트 할라이드 Bi_4X_4 (X= I, Br)의 위상적 상

지도교수 민 홍 기

이 논문을 이학박사 학위논문으로 제출함

2022년 6월

서울대학교 대학원
물리천문학부
윤 치 호

윤치호의 이학박사 학위논문을 인준함

2022년 7월

위 원 장	유재준	(인)
부위원장	민홍기	(인)
위 원	김기훈	(인)
위 원	양범정	(인)
위 원	정재일	(인)

Abstract

Topological phases in quasi-one-dimensional bismuth halides Bi_4X_4 (X= I, Br)

Chiho Yoon
Department of Physics and Astronomy
The Graduate School
Seoul National University

Since the successful exfoliation of graphene, researchers have been paying a great attention on van der Waals materials, a stack of layers or chains of atoms held together by weak van-der-Waals-like forces. Thanks to the weak interlayer or interchain bonding, a multilayer with an arbitrary thickness can be made from van der Waals materials. Very intriguingly, van der Waals material multilayers exhibit completely different physics as the number of stacked layers changes. In this dissertation, we investigate two kinds of van der Waals materials Bi_4X_4 (X=Br, I) and Bernal stacked multilayer graphene, focusing on the stacking-dependent topological properties and the effect of the electron-electron interaction.

In the first part, we focus on a family of quasi-one-dimensional materials Bi_4X_4. Bi_4X_4 are prototype weak topological insulators (TI) in the β phase. For the α phases, recent high-throughput database screening suggests that Bi_4Br_4 is a rare higher-order TI (HOTI) whereas Bi_4I_4 has trivial symmetry indicators. Here we show that in fact the two α phases are both pristine HOTIs yet with distinct termination-dependent hinge state patterns by performing first-principles calculations, analyzing coupled-edge dimerizations, inspecting surface lattice structures, constructing tight-binding models, and establishing boundary topological invariants. We reveal that the location of inversion center dictates Bi_4Br_4 (Bi_4I_4) to feature opposite (the same) dimerizations of a surface or intrinsic (bulk or extrinsic) origin at two side cleavage surfaces. We also conduct various experiments including the angle-resolved photoemission spectroscopy, gate-tunable transport, and the scanning tunneling microscopy to examine our predictions. Given the superior hinges along atomic chains, the structural transition at room temperature, and the extreme anisotropies in three axes, our results not only imply the possible existence of many topological materials beyond the scope of the current scheme for the classification of topological materials, but also establish a new TI paradigm and a unique material platform for exploring the interplay of geometry, symmetry, topology, and interaction.

In the second part, we analyze the ordered phases of Bernal stacked multilayer graphene in the presence of interaction induced band gaps due to sublattice symmetry breaking potentials, whose solutions can be analyzed in terms of light-mass and heavy-mass pseudospin doublets which have the same Chern numbers but opposite charge polarization directions. The application of a perpendicular external electric field reveals an effective Hund's rule for the ordering of the sublattice pseudospin doublets in a tetralayer, while a similar but more complex phase diagram develops with increasing layer number.

Keywords : Topological materials, van der Waals systems, thin films

Student Number : 2015-20342

List of Contents

Abstract . . . . **i**

List of Contents . . . . **viii**

List of Figures . . . . **xxii**

List of Tables . . . . **xxiv**

Chapter 1 Introduction **1**

Chapter 2 Preliminaries **5**

2.1 Topological insulators 5

2.1.1 Time-reversal-invariant topological insulators 5

2.1.2 Fu-Kane criterion 8

2.1.3 Topological crystalline insulator 11

2.1.4 Higher-order topological insulator 12

2.2 Boundary states and the surface Green’s function 15

Chapter 3 Topological phases in quasi-one-dimensional bismuth halides Bi_4X_4 (X = I, Br) **25**

3.1 Introduction 25

3.2 Crystal structures 30

3.2.1 Crystal structure of β-Bi_4X_4 32

3.2.2 Crystal structure of α-Bi_4Br_4 33

3.2.3 Crystal structure of α-Bi_4I_4 34
3.2.4 Atomic dimerization in α-Bi_4X_4 35
3.3 Low-energy band structures 36
3.4 Effective tight-binding models 40
3.4.1 β-Bi_4X_4 model 41
3.4.2 α-Bi_4Br_4 model 44
3.4.3 α-Bi_4I_4 model 45
3.5 Bulk band topology analysis 46
3.5.1 Symmetry indicators of Bi_4X_4 47
3.5.2 Unit cell doubling of β-Bi_4X_4 48
3.6 Topological boundary states of α-Bi_4X_4 51
3.6.1 Helical hinge and gapless surface states of α-Bi_4Br_4 51
3.6.2 Helical hinge states of α-Bi_4I_4 56
3.7 Band topology of α-Bi_4X_4 with open boundaries 60
3.7.1 Coupled edge construction 61
3.7.2 Surface models and the SSH dimerization 64
3.7.3 Surface topological invariants 67
3.7.4 Boundary-obstructed phase in α-Bi_4I_4 69
3.7.5 Domain wall argument 70
3.8 Experiments 72
3.8.1 Room-temperature topological phase transition in Bi_4I_4 72
3.8.2 Gate-Tunable Transport in α-Bi_4I_4 Field Effect Transistors 75

3.8.3 Stacking-dependent room-temperature quantum spin Hall edge states in α-Bi_4Br_4 thin-films 77
3.9 Discussion 81

Chapter 4 Broken sublattice symmetry states in Bernal stacked multilayer graphene 85
4.1 Introduction 85
4.2 Effective model and electron-electron interaction 87
4.3 Interaction-driven gapped phases in Bernal stacked tetralayer graphene 89
4.3.1 Ground states with broken sublattice symmetry . . . 89
4.3.2 Spin-valley degrees of freedom 91
4.4 Electric field induced "Hund's rule" and Hall effects 94
4.4.1 Flavor antiferro states 95
4.4.2 Flavor ferri and ferro states 96
4.4.3 Multiple hysteresis of layer charge polarization . . . 98
4.5 Generalization to thicker multilayer stacks 99
4.6 Discussion 102

Chapter 5 Conclusion 105

Appendix A Topological phases in quasi-one-dimensional bismuth halides Bi_4X_4 (X = I, Br) 107
A.1 Crystal structure data 107
A.2 Model fitting 107
A.3 More accurate α-Bi_4I_4 model 109

A.4 Extended winding number 111

A.5 Density of states of finite-sized α-Bi_4X_4 113

Appendix B Broken sublattice symmetry states in Bernal stacked multilayer graphene 117

B.1 Ground-state configurations for 6-layer graphene 117

B.2 Effect of the remote hopping terms 118

Bibliography 121

Abstract in Korean 133

List of Figures

Figure 2.1. History of topological insulators 6

Figure 2.2. Schematic picture for the formation of a TI from the band inversion. The red and blue dots on the TRIM indicate the signs of the inversion parity eigenvalues. . . . 10

Figure 2.3. Higher-order order topological insulators. d and k indicates the system dimension and the order of the topological phase, respectively. The yellow region in the figures indicate the region where the gapless topological boundary states are localized. 15

Figure 2.4. Principal layers of graphene with (a) the armchair edges and (b) the zigzag edges when only the nearest neighbor hoppings are considered. (c,d) Principal layers of graphene with the next nearest neighbor hoppings. Here, the red and green colors indicate the two inequivalent sites in a graphene unit cell. 21

Figure 2.5. Edge spectral densities of (a) the armchair and (b) the zigzag edges. 23

Figure 3.1. (a) An atomic chain as the building block of $\mathrm{Bi_4X_4}$. The purple (brown) balls are the Bi (X) atoms. (b) A (001) monolayer of $\mathrm{Bi_4X_4}$. The black diamond is a primitive unit cell. The red dots are possible inversion centers. The dashed red line is a mirror plane. (c)-(e) Left panels: the bulk structures of β-$\mathrm{Bi_4X_4}$, α-$\mathrm{Bi_4Br_4}$, and α-$\mathrm{Bi_4I_4}$ viewed from the $\bar{\boldsymbol{b}}$ axis. The solid black lines sketch the primitive unit cells. The X atoms are omitted for better illustration. The green bubbles indicate the dimerization patterns of the NN inter-edge tunnelings. The red dots are possible inversion centers. Right panels: the side monolayers in the dashed black frames in the left panels viewed from the $\boldsymbol{a}$ axis. 31

Figure 3.2. The 3D bulk and (001) monolayer ribbon band structures of (a) β-$\mathrm{Bi_4Br_4}$, (b) α-$\mathrm{Bi_4Br_4}$, (c) α-$\mathrm{Bi_4I_4}$, and (d) β-$\mathrm{Bi_4I_4}$. The SOC is not included in the top panels but included in the middle and bottom panels. The size of red (blue) dots indicates the weight of the p_x orbital of $\mathrm{Bi_{in}}$ ($\mathrm{Bi_{ex}}$) atoms. The ± signs label the inversion eigenvalues at the L and M points, with the inversion centers in (001) layers in (a), (b), and (d) but in the middle of two adjacent layers in (c). The green lines are the helical edge states (degenerate for two edges in (a), (b), and (d)), implying that the four (001) monolayers are all 2D $\mathbb{Z}_2$ TIs. 37

Figure 3.3. The band evolution at the L and M points near the Fermi energies of $\mathrm{Bi}_4\mathrm{X}_4$. From left to right, we consider the electronegativity of the atomic orbitals, the splitting due to the (010) mirror symmetry, the formation of bonding and anti-bonding states as a result of the intra- and inter-chain couplings, and the possible band inversion driven by the SOCs. The details are explained in the text. 38

Figure 3.4. The band structures (black) and band inversions (±) of (a) β-$\mathrm{Bi}_4\mathrm{Br}_4$, (b) α-$\mathrm{Bi}_4\mathrm{Br}_4$, (c) α-$\mathrm{Bi}_4\mathrm{I}_4$, and (d) β-$\mathrm{Bi}_4\mathrm{I}_4$ in Fig. 3.2 fitted by our effective tight-binding models (red) evaluated by the set of parameter values in Appendix A.2. 40

Figure 3.5. The inversion eigenvalues of the occupied bands at the TRI momenta for the β phase WTI, modeled by Eqs. (3.2) and (3.5). Different inversion centers and primitive unit cells are chosen in (a) and (c). Illustrating the band inversions in α-$\mathrm{Bi}_4\mathrm{Br}_4$ and α-$\mathrm{Bi}_4\mathrm{I}_4$, respectively, (b) and (d) are the doubled unit cell counterparts of (a) and (c). In the bottom panels, the solid lines, dashed boxes, and red dots denote the (001) layers, unit cells, and inversion centers, respectively. 49

Figure 3.6. The helical hinge states of α-Bi$_4$Br$_4$ under four different scenarios of (001) surface terminations. (a)-(d) The label on the top of each column indicates the layer stacking order of the considered system in the $\boldsymbol{c}$ axis, and the red letters denote the extra (001) layer(s) compared with the case in (a). Upper panels: schematics of the helical hinge states in the $\boldsymbol{b}$ (chain) direction and the Dirac surface states at the (010) and $(0\bar{1}0)$ surfaces. The green regions are the gapless boundaries, and each red cross denotes a surface Dirac cone. Middle panels: calculated band structures by using the MLWF. All the four systems are of finite size in the $\boldsymbol{a}$ and $\boldsymbol{c}$ directions and periodic in the $\boldsymbol{b}$ direction. The zero energy is set at the 0 meV in Fig. 3.2(b). The green lines are the helical hinge states, and the black lines are the gapped surface states. Because of the unbroken inversion symmetry in odd-layer systems, all the bands are doubly degenerate in (a) and (c). Lower panels: calculated spatial densities for the helical hinge states at the energy indicated by the dashed lines in the middle panels. 52

Figure 3.7. (a) Gapless (010) surface states of pristine α-Bi$_4$Br$_4$ and (b) gapped (010) surface states of α-Bi$_4$Br$_4$ with a C_2-asymmetric TRI surface potential. The constant-energy contours with a spacing of 0.5 meV are obtained by the surface Green's function calculations of the MLWF for a semi-infinite system. The zero energy is set at the 0 meV in Fig. 3.2(b). 55

Figure 3.8. The helical hinge states of α-Bi$_4$I$_4$ under four different scenarios of (001) surface terminations. (a)-(d) The label on the top of each column indicates the layer stacking order of the considered system in the $2\boldsymbol{c}-\boldsymbol{a}$ axis, and the red letters denote the extra (001) layer(s) compared with the case in (a). Upper panels: schematics of the helical hinge states in the $\boldsymbol{b}$ (chain) direction. The green regions are the gapless boundaries. Middle panels: calculated band structures by using the MLWF. All the four systems are of finite size in the $\boldsymbol{a}$ and $2\boldsymbol{c}-\boldsymbol{a}$ directions and periodic in the $\boldsymbol{b}$ direction. The zero energy is set at the 0 meV in Fig. 3.2(c). The green lines are the helical hinge states, and the black lines are the gapped surface and bulk states. Because of the unbroken inversion symmetry in even-layer systems, all the bands are doubly degenerate in (a) and (c). Lower panels: calculated spatial densities for the helical hinge states at the energy indicated by the dashed lines in the middle panels. 58

Figure 3.9. (a)-(c) The possible inversion centers (or twofold rotation axes) of Bi_4X_4 and the dimerization patterns of the coupled edge states at the two side surfaces. The black and blue lines denote the B- and A-type (001) layers. The red dots denote the inversion centers (or twofold rotation axes). The green dots denote the helical edge states in the $\boldsymbol{b}$ (chain) direction. The double solid and single dashed red lines denote the stronger and weaker NN inter-edge tunnelings. (d) All possible (001) surface terminations: one for the β phase and four for each α phase. The green lines denote the Dirac surface states, and the green dots denote the helical hinge states. 63

Figure 3.10. Schematics of inversion symmetric (a) α-Bi_4Br_4 and (b) α-Bi_4I_4 samples with or without helical hinge states. The relative signs of the mass term gapping the two surface Dirac cones are indicated in red. The hinge states along the domain walls switching the mass signs are indicated in green. (The other two hinge state patterns for α-Bi_4Br_4 are not shown. The $\mathcal{C}_2$ symmetry is not considered here.) 71

Figure 3.11. (a) Temperature-dependent resistivity data for both cooling and warming curves. The inset is the enlarged view showing the hysteresis behavior of the first-order transition. (b) Measured dispersions in α-Bi$_4$I$_4$ along high symmetry cuts. (c) Calculated bulk band structure of α-Bi$_4$I$_4$ projected onto the (001) surface. (d),(e) Same as (b),(c) but for β-Bi$_4$I$_4$. A clear doubling of the bulk valence bands is evident from β-Bi$_4$I$_4$ to α-Bi$_4$I$_4$ in both the measured and calculated dispersions. All measurement temperatures are as indicated. 73

Figure 3.12. Surface states evolution across the phase transition. (a) Band image along the k_b-axis on the (001) surface of α-Bi$_4$I$_4$ as well as its corresponding EDC stacks. The red EDC corresponds to $k_b = 0$. The green dots track the peak positions of the bulk band which reveal a gap opening of $\sim$85 meV. (b) Same as (a) but of β-Bi$_4$I$_4$. A gap opens at $k_b = 0$ of $\sim$100 meV. (c) Band image along the k_b-axis on the (201) surface of α-Bi$_4$I$_4$ as well as its corresponding EDC stacks. The blue dots track the surface state which reveal a $\sim$35 meV gap opening. (d) Same as (c) but the (100) surface of β-Bi$_4$I$_4$. A gapless Dirac surface state is observed. 74

Figure 3.13. (a) Side view of an AB-bilayer. The hybridization of edge state is destructive, as illustrated by the lighter color of the edge states (red spheres). (b) Construction of a higher-order topological insulator based on the hybridization mechanism in (a). (c) Spectroscopic imaging of the crystalline steps. The bottom panel shows the topographic image of two-step edges. The middle panel shows the corresponding differential conductance map obtained at energy outside the insulating gap. The top layer shows the corresponding differential conductance map obtained at energy inside the insulating gap, revealing pronounced edge states. (d) Topographic image of two adjacent bilayer atomic step edges forming a trench. (e) Differential spectra taken at the left AB bilayer step edge (red), right AB bilayer step edge (violet), and away from the edges (blue). Red and violet dots in panel (d) denote the respective positions on the left and right AB edges where the differential spectra are taken. (f) Differential conductance map, taken at $V = 0$ mV and -75 mV [marked with color-coded arrows in the differential spectra in panel (e)] shown in two layers. $V = 0$ mV and -75 mV, both of which are inside the insulating gap. 78

Figure 3.14. Calculated bilayer and twenty-layer step-edge states. (a) The edge-projected band structure for a (001) twenty-layer ribbon on the top surface of α-Bi_4Br_4. The cyan bands are from the bulk and (001) surfaces of the system. The orange bands are from the (100) and ($\bar{1}$00) side surfaces of the ribbon. The red bands are the gapless hinge states. Due to the inversion asymmetry of even-layer systems, the bands are singly degenerate at each k_b. The ribbon is infinitely long in the b direction and 50-chain wide in the a direction. (b) The same as a but for a bilayer ribbon. The two helical edge states from the two monolayers are gapped at one side (orange) but remain gapless at the other side (red). (c) The real space schematics of the surface and hinge/edge states in [(a) and (b)]. (d) Calculated edge gap of (001) even-layers. . 80

Figure 4.1. Electronic structure and zero-energy wavefunction configurations near the K or K' valley for ABAB tetralayer graphene obtained respectively from (a), (c) the non-interacting continuum model and (b), (d) a self-consistent Hartree-Fock calculation. Two pseudospin doublets are labeled by “Light” or “Heavy” depending on their effective mass of the energy band. In the case of non-interacting model, all four spin/valley flavors have the same wavefunction configuration with localized wavefunctions on the gray sublattices, as shown in (c). When electron-electron interactions are turned on, the sublattice symmetry is broken for both doublets transferring charges either from A to B sublattices or vice versa, as indicated in red (positive charge) and blue (negative charge) color in (d). The $(\downarrow, \Uparrow)$ and $(\uparrow, \Downarrow)$ labels represent two possible configurations of opposite charge polarization towards the top and bottom layers corresponding to the light and heavy mass bands. 90

Figure 4.2. Schematic picture of the ground-state configuration and corresponding spontaneous Hall effect at zero external electric field for three possible flavor antiferro states: LAF, QSH and QAH. Arrows in the square box and numbers below the box at each spin/valley flavor represent pseudospin polarizations and corresponding Chern numbers, respectively, whereas the arrows above the box indicate the corresponding net current directions expected in the Hall measurement. 93

Figure 4.3. The evolution of the layer antiferromagnetic state under a perpendicular external electric field, keeping the flavor degeneracy of the system. Arrows in the square box and numbers below the box at each spin/valley flavor represent pseudospin polarizations and corresponding Chern numbers, respectively, whereas the arrows above the box indicate the corresponding net current directions expected in the Hall measurement. The change in the charge polarization by applying a perpendicular electric field is denoted by the dashed circle. 94

Figure 4.4. The evolution of ABAB tetralayer graphene under a perpendicular external electric field for (a) a flavor ferri state with the minority pseudospin configuration ($\uparrow$, $\Downarrow$) on K'_{d} and (b) a flavor ferro state with ($\downarrow$, $\Uparrow$) for all four flavors. Arrows in the square box and numbers below the box at each spin/valley flavor represent pseudospin polarizations and corresponding Chern numbers, respectively, whereas the arrows above the box indicate the corresponding net current directions expected in the Hall measurement. The change in the charge polarization by applying a perpendicular electric field is denoted by the dashed circle. 97

Figure 4.5. (Left) External field dependence of the total charge polarization ζ defined in Eq. (4.5) for flavor antiferro (top), ferri (middle) and ferro (bottom) states. The solid and dashed lines indicate evolutions of states from two different initial states with reversed polarization direction for each pseudospin. For each solid line, the pseudospin configurations are depicted. (Right) Zoomed view of the dashed rectangular area in the left panel. 99

Figure 4.6. (a) Energy band gap as a function of the number of layers in the absence of a perpendicular electric field. The energy gaps of even (odd) number of layers are denoted by red (blue) circles. (b) The lowest total energy states in the presence of electric field. Flavor antiferro, ferri, and ferro states are colored in blue, red, and gray, respectively. The pseudospin polarization directions are written in increasing effective mass order. 100

Figure A.1. (a) Stacking registry of α-Bi$_4$I$_4$. The dashed boxes are the primitive unit cells. The red dots are the inversion centers. (b) and (c) are two adjacent layers in the same and different unit cells, respectively, viewed from the $\boldsymbol{c}-\boldsymbol{a}/2$ axis. The zigzag lines sketch the atomic chains. The solid and dashed lines denote the upper and lower layers. The blue and gray dots are the centers of the unit cells of individual layers. $\boldsymbol{d}$, $\boldsymbol{d}-\boldsymbol{a}_1$, $\boldsymbol{d}-\boldsymbol{a}_2$, and $\boldsymbol{c}-\boldsymbol{d}$ connect the centers of two adjacent layers. The green arrows are vectors connecting different inter-layer NNs. Based on Table A.1, the layer spacing is nearly uniform, and $\boldsymbol{d}$ is close to $\boldsymbol{c}/2+\boldsymbol{a}/4$; the spacing variation in (a) and the layer mismatch in (c) are exaggerated. 110

Figure A.2. The trajectory of $(h_x(q), h_y(q))$ in Eq. (A.5). 112

Figure A.3. (a) (201) surface states of α-Bi_4I_4. The zero energy is set at the 0 meV in Fig. 3.2(c). (b) The DOS of α-Bi_4I_4 rod which is periodic in the $\boldsymbol{b}$ direction, 1000-unit-cell long in the $\boldsymbol{a}$ and $\boldsymbol{c}$ direction. (c), (d) The DOS of α-Bi_4Br_4 and α-Bi_4I_4 near the surface gap. The systems in Figs. 3.6 and 3.8 are used here. 114

Figure B.1. The phase diagram for the ground state configuration of tetralayer graphene on α and γ_2 plane. Here, the gap (remote-hopping) dominant region denotes a region where the ground state is (not) described by the sublattice symmetry breaking and the effective Hund's rule. 120

List of Tables

Table 4.1. Spontaneous quantum Hall conductivities in units of e^2/h for the antiferro states in Bernal stacked tetralayer graphene under a perpendicular external electric field. Here, $E_{\mathrm{c1}} = 0.025$ mV/Å and $E_{\mathrm{c2}} = 0.879$ mV/Å. . . . 95

Table 4.2. Spontaneous quantum Hall conductivities in units of e^2/h under a perpendicular external electric field in ABAB tetralayer for the ferri and ferro states in Fig. 4.4. Here, $E_{c1+}^{\mathrm{ferri}} = 0.019$, $E_{c2+}^{\mathrm{ferri}} = 0.943$, $E_{c1-}^{\mathrm{ferri}} = 0.031$, and $E_{c2-}^{\mathrm{ferri}} = 0.815$ meV/Å for the ferri state, whereas $E_{c1+}^{\mathrm{ferro}} = 0.013$ and $E_{c1-}^{\mathrm{ferro}} = 0.753$ meV/Å for the ferro state. . . 98

Table A.1. Crystal structure data of $\mathrm{Bi_4X_4}$. For α-$\mathrm{Bi_4I_4}$, the second line gives the values of the angle θ_2' and the distance $\mathrm{Bi}'_{\mathrm{in}}$-$\mathrm{Bi}'_{\mathrm{ex}}$. For α-$\mathrm{Bi_4Br_4}$, the two lines list the parameter values of the two symmetry unrelated (001) layers, respectively. Note that $\alpha = \gamma = 90^\circ$ and that conventional unit cells are used. 108

Table A.2. A set of parameter values in units of meV for the $\mathrm{Bi_4X_4}$ models in Sec. 3.4 that can well fit the band inversions and band structures given by the MLWF data. 109

Table B.1. Charge polarizations and corresponding Chern numbers in the presence of a perpendicular electric field in Bernal stacked 6-layer graphene for the LAF state. The pseudospins are written in increasing effective mass order from the left to the right. Here, $E_{\mathrm{c1}}^{(6)} = 0.017$, $E_{\mathrm{c2}}^{(6)} = 0.251$, and $E_{\mathrm{c3}}^{(6)} = 0.281$ meV/Å. Red arrows indicate flipped pseudospin polarizations with field. 118

Table B.2. Spontaneous quantum Hall conductivities in units of e^2/h for the antiferro states in Bernal stacked 6-layer graphene under a perpendicular external electric field. . 119

Chapter 1

Introduction

Since the first successful exfoliation of a two-dimensional (2D) material graphene [1, 2], researchers have been paying a great attention to van der Waals materials in the last two decades of the twenty-first century. Van der Waals materials is a stacking of 2D layers or 1D chains of atoms held together by weak van-der-Waals-like forces. Thanks to the weak interlayer or interchain bonding, one can reach the mono- or few-layer limit, where the physical properties of the material changes dramatically as the number of layers changes. Especially in the case of multilayer graphene, various types of chiral 2D electron gases are realized near the charge neutral point, which plays as a fertile ground for the interesting many-body physics [3]. In addition to the study of few-layer systems, recently the researchers have been building the heterostructures, a stacking of different 2D crystals on the top of each other [4]. By stacking different systems, we expect to engineer a system unforeseen in the nature. And even more, very recently researchers discovered that stacking 2D materials with a little bit of 'twist' also leads to the unforeseen physical systems. The most famous example is the bilayer graphene system with a twist of the magic angle of $\sim 1.1^\circ$, where the unconventional superconductivity is observed [5–7].

On the other hand, around the same time, a new paradigm 'topological phase of matter' was rising in condensed matter physics. In 2004, Kane and Mele [8, 9] proposed that the the spin-orbit interaction can lead to the new phase called 'topological insulator' (TI) and soon this phase was verified in the HgTe/CdTe quantum well [10, 11] and even in a natural material Bi_2Se_3 [12]. The discovery of TI has highlighted the importance of the topology in condensed matter systems and then numerous new topological phases of matter like topological crystalline insulators, topological semimetals, topological and superconductors has been proposed until very recently.

A TI is characterized by gapless helical states at the boundary of the system. As long as time-reversal symmetry is protected, the gapless helical states are robust against perturbation and these boundary states carry spin Hall current. Not only a TI but also most of the topological phases of matter are characterized by the unique boundary states which cannot be realized in the bulk alone. This aspect of the topological phases is called the 'bulk-boundary correspondence'. As the novel physical features like the spin current and Majorana zero modes occur at the boundaries due to the bulk-boundary correspondence, the boundary physics has become very important recently. In fact, van der Waals materials can play as excellent platforms for the study of the boundaries, since the clean cleavage planes or edges are expected due to the weak interlayer or interchain bonding. Among van der Waals materials, quasi-one-dimensional (quasi-1D) materials especially have been highlighted recently because the natural cleavage surfaces can be obtained in multiple of directions, which is crucial for the verification of the weak TI and the higher-order TIs.

In this dissertation, we discuss two van der Waals materials $\mathrm{Bi_4X_4}$ (X=Br, I) family and Bernal stacked multilayer graphene, focusing on their topological properties dependent on the stacking structures, *e.g.* the number of stacked layers and the boundary termination. In the first part, Chap. 3, we discuss how are the various phases of $\mathrm{Bi_4X_4}$ are related to each other from the crystal structures and the bulk band structure topology analysis. We also show that the α phases of $\mathrm{Bi_4X_4}$ exhibit novel stacking-dependent topological helical hinge states, some of which cannot be understood by the conventional TI theories. In the second part, Chap. 4, we study the ground states of Bernal stacked multilayer graphenes under the (mean-field) electron-electron interaction. We find interaction-driven energy gaps in Bernal stacked even-layer graphenes. The gapped ground states are topological and the non-trivial topology is characterized by the non-zero Chern numbers near the K/K' valleys. We further investigate the effect of the external electric field and find that various interaction-driven topological phases can be tuned by applying the external electric field.

Chapter 2

Preliminaries

2.1 Topological insulators

Over the past two decades, the study on the topological phases of matter has been very rapidly grown, as shown in Fig. 2.1. Without a doubt, topological phases of matter have taken the condensed matter physics community by storm. In this section, we briefly introduce TIs and their variants, and ways to diagnose them. Following the history of TI, we show how the concept of the TI can be extended to the topological crystalline insulator and further to the higher-order TI.

2.1.1 Time-reversal-invariant topological insulators

According to Hasan and Kane in the celebrated review Ref. [13], "*Topological insulators are electronic materials that have a bulk band gap like an ordinary insulator but have protected conducting states on their edge or surface.*". This intriguing phenomenon is in fact not so new, since it is one of the characteristics of an integer quantum Hall insulator (IQHE). However, until very recently, this phenomenon has been overlooked by most of the people, partly because the IQHE phase only occurs under a very strong

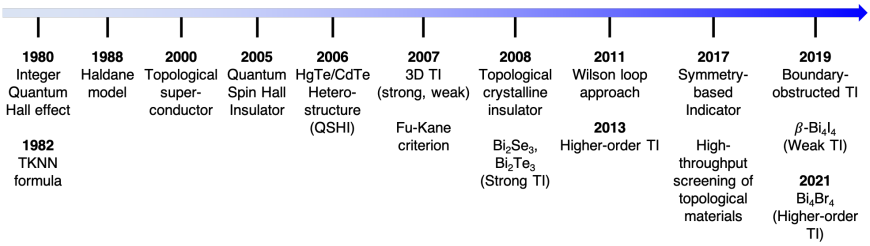
1980
Integer Quantum Hall effect
1982
TKNN formula
1988
Haldane model
2000
Topological super-conductor
2005
Quantum Spin Hall Insulator
2006
HgTe/CdTe Hetero-structure (QSHI)
2007
3D TI (strong, weak)
Fu-Kane criterion
2008
Topological crystalline insulator
Bi_2Se_3, Bi_2Te_3 (Strong TI)
2011
Wilson loop approach
2013
Higher-order TI
2017
Symmetry-based Indicator
High-throughput screening of topological materials
2019
Boundary-obstructed TI
β-Bi_4I_4 (Weak TI)
2021
Bi_4Br_4 (Higher-order TI)

Figure 2.1: History of topological insulators

magnetic field and not found in a natural material without an external field. Although Haldane demonstrated that the Landau level is not a necessary for the IQHE by introducing the so-called Haldane model [14], this model had got less attention for a long time since it required unrealistic fine-tuned magnetic flux into a unit cell. In 2005, Kane and Mele discovered a new type of topological insulator (TI) called the “quantum spin Hall insulator” (QSHI) or simply a 2D TI [8, 9]. This phase was firstly demonstrated in a graphene with the significant spin-orbit coupling (SOC). In Ref. [8], Kane and Mele carefully investigated the edge states of a graphene nano-ribbon. Interestingly, the graphene nano-ribbon exhibit gapless edge states with a point-wise double degeneracy and this persists as long as the bulk band gap remains opened and time-reversal symmetry is not broken. Soon, they realized that this degeneracy is not accidental, not limited to the graphene model. They found that this system is “topologically distinct” from a trivial insulator.

Kane and Mele found that if s_z, the spin along the z-axis, commutes with the model Hamiltonian for graphene with the SOC, the model is nothing but two copies of the Haldane models, where each copy has the opposite sign in the quantum Hall conductance. Thus, though this system may exhibit trivial quantum Hall coefficient, this system is topologically non-trivial since each sector in s_z exhibit non-trivial quantum Hall conductances. The non-triviality of this system can be simply characterized by quantized spin Hall conductivity, where

$$\sigma^s_{xy} = \frac{1}{2}(\sigma^{\uparrow}_{xy} - \sigma^{\downarrow}_{xy}) = n_s \frac{e^2}{h}. \tag{2.1}$$

However, s_z conservation does not happen in a generic realistic system and thus the topological characterization of the system using Eq. (2.1) should fail. Nevertheless, the gapless edge states exists with or without the s_z breaking terms and there would be a way to diagnose this non-trivial phase. In the milestone paper Ref. [9], Kane and Mele derived a new “topological” invariant to characterize the newly phase found in graphene. This invariant is defined up to $\mathbb{Z}_2$ and the robustness of the invariant is protected by time-reversal symmetry. The invariant is defined from the “Pffafian” of the sewing matrix that relates the occupied eigenstates of two different momenta $\boldsymbol{k}$ and $-\boldsymbol{k}$.

Soon after the discovery of the QSHI phase in 2D, three groups independently discovered that the QSHI phase can be extended to the 3D systems, which we now call by the “topological insulator” [15–17]. In the case of the 3D TIs, the topological phases are classified by four $\mathbb{Z}_2$ indices, which are usually written as $(\nu_0; \nu_1\nu_2\nu_3)$. The first index ν_0 is called the strong index and the other three indices are called the weak indices. If ν_0

is non-trivial, this system is called a strong TI and exhibit gapless surface Dirac cones at any side surfaces as long as time-reversal symmetry is not broken and the 3D bulk gap remains opened. If ν_0 is trivial and at least one of the weak indices is non-trivial, this system is called a weak TI. A weak TI exhibit gapless surface states at the surfaces whose normal is not parallel to $(\nu_1\nu_2\nu_3)$. The weak TI phase is “weak” in the sense that it additionally requires the protection of discrete translational symmetry along the directions parallel to the surface.

Since this seminal work by Kane and Mele, a number of studies have been conducted to realize this new topological phase experimentally. Although Kane and Mele first discovered the QSHI phase in graphene, graphene was shown to have a negligible SOC [18] immediately after the discovery of the QSHI phase and was excluded from the candidate for the experimental realization. Nevertheless, starting from the HgTe/CdTe heterostructure in 2006 [10, 11] and $\mathrm{Bi_2Se_3}$ in 2009 [19], a considerable number of materials have been revealed as TIs. As of 2022, approximately 53% of the all non-magnetic stoichiometric materials are shown to be topological at the Fermi energy and 88% of them are shown to have at least one topological property in the whole energy range [20].

2.1.2 Fu-Kane criterion

Although Kane and Mele successfully proved that the QSHI phase is a new topological phase of matter, There were some problems in Kane and

Mele's expression for the $\mathbb{Z}_2$ topological invariant which hindered the search for TIs. Firstly, the expression for the $\mathbb{Z}_2$ topological invariant derived by Kane and Mele is very difficult to calculate, since the smooth gauge choice in the whole Brillouin zone was required and thus the formula for the $\mathbb{Z}_2$ invariant was incompatible with complicated models like the first principle calculations. Secondly, the physical meaning of the $\mathbb{Z}_2$ topological invariant is not obvious in Kane and Mele's formula, as the invariant was derived within the mathematical framework of K-theory.

In 2007, Fu and Kane showed that these problems can be completely resolved if an insulator has additional spatial inversion symmetry [15]. They showed that if a system has inversion symmetry, very complicated expressions for the $\mathbb{Z}_2$ topological invariants in 2D and 3D TIs become nothing but the multiplication of the inversion eigenvalues of occupied states at the time-reversal-invariant momenta (TRIMs). To be explicit, the $\mathbb{Z}_2$ invariant ν in a 2D TI and the $\mathbb{Z}_2$ invariants $(\nu_0;\nu_1\nu_2\nu_3)$ are given as the following:

$$\begin{aligned}(-1)^{\nu} &= \prod_{i=1}^{4}\delta_i,\\ (-1)^{\nu_0} &= \prod_{i=1}^{8}\delta_i,\\ (-1)^{\nu_k} &= \prod_{n_k=1,n_{j\neq k}=0,1}\delta_{i=(n_1n_2n_3)},\end{aligned} \tag{2.2}$$

where

$$\delta_i = \prod_{m=1}^{N}\xi_{2m}(\Gamma_i), \tag{2.3}$$

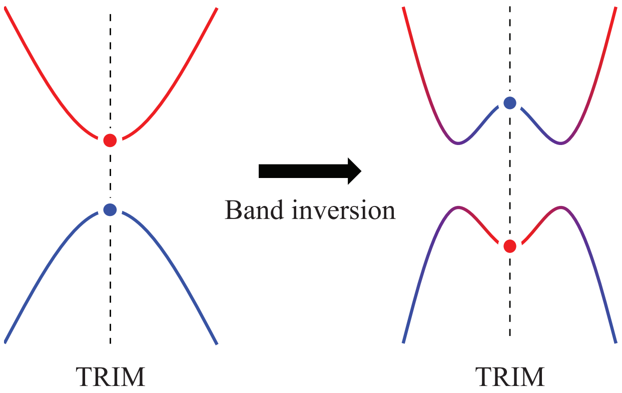

Figure 2.2: Schematic picture for the formation of a TI from the band inversion. The red and blue dots on the TRIM indicate the signs of the inversion parity eigenvalues.

and here Γ_i is the i-th TRIM among the 8 (4) TRIMs in a 3D (2D) system, $2N$ is the number of occupied bands, and ξ_{2m} is the inversion parity eigenvalue of $2m$-th occupied band. We assume that $2m$-th and $(2m-1)$-th bands are the Kramer's degeneracy partners at each TRIM. As shown in Eqs. (2.2) and (2.3), the topological invariants can be directly calculated only by knowing the inversion parities at the TRIMs and does not require any complicated process like gauge fixing.

As a result of this striking simplification, the search for topological materials was dramatically boosted and soon various materials like $\mathrm{Bi}_{1-x}\mathrm{Sb}_x$, α-Sn, SnTe, and $\mathrm{Bi_2Se_3}$ have been newly suggested as a TI. More importantly, thanks to the simple expression for the $\mathbb{Z}_2$ invariants, a very common mechanism called the "band inversion" which makes a system a TI has been clarified. Suppose we have an insulator which has a small direct gap at a TRIM and large direct gaps at other TRIMs and suppose that the valance band and the conduction band has different inversion parity eigenvalues at the TRIM with a small direct gap, as shown in the left side of Fig. 2.2. Then one can derive a phase transition between the trivial insulator and the TI phases, by applying a potential to the original system which results in the shift of the valance band top to the conduction band and the conduction band bottom to the valance band which is shown in the right side of Fig. 2.2. The application of such potential may correspond to the chemical substitution in experiment, or turning on the SOC or the crystal field in theoretical calculations. One of the prototypical examples would be the realization of the 3D TI phase in $\mathrm{Bi}_{1-x}\mathrm{Sb}_x$ by varying x.

2.1.3 Topological crystalline insulator

As discussed above, the TI phase is protected by only time-reversal symmetry Θ, which satisfies $\Theta^2 = -1$. But, in the study of the prototypical TI $\mathrm{Bi}_{1-x}\mathrm{Sb}_x$, Teo, Fu, and Kane discovered that mirror symmetry can lead to the additional topological structure of the bulk band structures [21]. The additional structure protected by mirror symmetry is similar to the model for graphene with the s_z conservation we discussed in Sec. 2.1.1. Suppose we have a system with time-reversal symmetry Θ and mirror symmetry $M_z = -is_z$. Then the Hamiltonian on the mirror-invariant plane in the momentum space can be expressed by

$$H(\boldsymbol{k}) = \begin{pmatrix} H_{+i}(\boldsymbol{k}) & 0 \\ 0 & H_{-i}(\boldsymbol{k}) \end{pmatrix}, \tag{2.4}$$

where $H_{\pm i}(\boldsymbol{k})$ is a subspace of the basis for $H(\boldsymbol{k})$ with mirror eigenvalue $M_z = \pm i$. In this case, each sector $H_{\pm i}(\boldsymbol{k})$ can be considered as an insulator without time-reversal symmetry. Then similar to the spin Chern number in Eq. (2.1), we can define the "mirror Chern number" $N_M = \frac{1}{2}(N_{+i} - N_{-i}) \in \mathbb{Z}$ where $N_{\pm i}$ is the Chern number of $H_{\pm i}(\boldsymbol{k})$, and a system with non-zero N_M will exhibit N_M surface Dirac cones on the mirror-invariant surfaces. For a time-reversal-invariant system with mirror symmetry, the $\mathbb{Z}_2$ invariant ν_0 is given by $\nu_0 = N_M \bmod 2$. This implies that although the $\mathbb{Z}_2$ invariant ν_0 is trivial, the system can be topologically non-trivial with finite $N_M \in 2\mathbb{Z}$ with the aid of mirror symmetry. This discovery broadened the concept of the TI to the new topological phases protected by crystalline symmetries, called the "topological crystalline insulator" (TCI) [22]. The TCI phase was firstly identified in SnTe, $\mathrm{Pb}_{1-x}\mathrm{Sn}_x\mathrm{Se}$, and $\mathrm{Pb}_{1-x}\mathrm{Sn}_x\mathrm{Te}$, which have four Dirac cones on the (001) surface [23].

2.1.4 Higher-order topological insulator

For the almost two decades since the discovery of TI and TCI, a number of studies have proven that the topological phases are not rare and occurs in many of materials on an ordinary basis. Meanwhile, many new approaches have been tried to broaden our understanding of topological insulators. Below, we introduce two different point of view on the topological (crystalline) insulators.

Since the pioneering work by Fu and Kane in 2006 [24], topological (crystalline) insulator phase has been identified as a phenomenon that an insulator exhibiting non-trivial flow of charge along a certain direction in the momentum space, which generalizes the “charge pump” argument in the IQHE system. This motivated people to develop the “Wilson loop” method [25], which can diagnose the topological insulator phase by tracking the charge polarization of the eigenstates in the occupied bands.

On the other hand, people also tried to understand topological insulator phase in the viewpoint of “obstruction”. It is well known that a non-zero Chern number in a IQHE system is an obstruction to smoothly defining the wave function throughout the entire Brillouin zone. Fu and Kane [24] showed that the obstruction is not a unique property of the IQHE phase but also happening in a TI. Motivated by Fu and Kane, now the presence of the obstruction is often considered as a definition rather than a property of the topological insulator phase. From the viewpoint of the obstruction, one can understand the topological insulator phase as an insulator that is not an atomic insulators at which a smooth gauge choice in the wave function is possible.

This new definition of topological insulator phase allowed the automated classification of all the possible topological (crystalline) insulator phases and several groups independently reported new ways to classify all the topological insulators since 2017 [26–31]. One of the pioneering approach is “topological quantum chemistry” [28]. In this work, Bradlyn *et al.*considered all the atomic insulators and their band representations at the high-symmetry points, lines, and planes. If the band representations at each high-symmetry sites are connected in such a way that they form a "disconnected" graph, this system is found to be topological if the disconnected bands are partly occupied.

Another very important approach is called the "symmetry-based indicator", which was invented independently in Refs. [26] and [27]. Instead of investigating the band representation at the high-symmetry sites, the symmetry-based indicator investigates the symmetry eigenvalues at the high-symmetry sites. Then the symmetry eigenvalues of the band structures can be expressed as a "vector" which characterizes a band structures. In Ref. [27], the authors diagnosed topological insulators as non-trivial elements of the quotient group $X_{\mathrm{BS}} = \{\mathrm{BS}\}/\{\mathrm{AI}\}$, where $\{\mathrm{BS}\}$ ($\{\mathrm{AI}\}$) is the vector space of all the possible insulator (atomic insulator) spanned by the vectors containing symmetry eigenvalue information. This method can be understood as a generalization of the Fu-Kane criterion and very powerful in many cases since the topological phases can be diagnosed only from the symmetry eigenvalues.

From the high-throughput calculations, many new TIs have been discovered. However, some of the newly discovered TIs does not show the bulk-boundary correspondence, i.e. they lack gapless surface states even though the bulk band structures are clearly distinct from the atomic insulators as the obstruction exists. One example is the "topological axion insulator", which is characterized by the topological magnetoelectric effect with an effective action which integrates $\mathbf{E} \cdot \mathbf{B}$ over the (3+1)-D space [32]. Around 2017, people started to realize that for some TCIs, bulk-boundary

	$k = 1$	$k = 2$	$k = 3$
$d = 3$	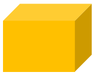	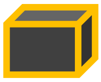	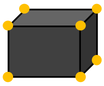
$d = 2$	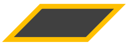	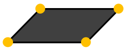	
$d = 1$	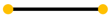		

Figure 2.3: Higher-order order topological insulators. d and k indicates the system dimension and the order of the topological phase, respectively. The yellow region in the figures indicate the region where the gapless topological boundary states are localized.

correspondence can appear at boundaries of more than one dimension lower, as shown in Fig. 2.3 [33–43]. Such TCIs are called the “higher-order topological insulators” (HOTIs), where the order of topological insulators is defined by the codimension of the region where the gapless states are localized. The HOTI phase is originally suggested around 2013 in the study of the boundary states [33], although the higher-order boundary states were not considered as the bulk-boundary correspondence at that time. The higher-order topological phase was experimentally observed in pure bismuth [39] and α-Bi_4Br_4 [44, 45] very recently.

2.2 Boundary states and the surface Green’s function

One of the most striking characteristics of the topological phases of matter is the bulk-boundary correspondence: the non-trivial band topology is characterized by the unique boundary states. For example, a time-reversal-invariant 2D TI is characterized by the gapless helical edge states and a 3D Weyl semimetal exhibit line-shaped states at the Fermi energy called Fermi arcs. Thus, an efficient way to observe the boundary states with the given bulk band structures is necessary in the study of the topological phases of matter. There are many ways to investigate boundary states and each method has advantages and limitations. In this section, we introduce three methods which will be used in this thesis.

The most straightforward method to get the boundary states would be constructing the finite-sized tight-binding Hamiltonian directly from the bulk Hamiltonian. This method has various advantages. Firstly, it is very simple to construct a finite-sized Hamiltonian from the bulk Hamiltonian. Secondly, one can easily add arbitrary boundary conditions. Thirdly, the wave functions of the boundary states can be obtained. However, in many cases, the computation cost is tremendous for this method. For example, a 2D system which has the finite length of N_x unit cells along the x axis has N_x times larger columns and rows than the 2D bulk Hamiltonian and solving the eigenvalue problem of the finite-sized system takes N_x^3 times larger than the bulk system. But to have the boundary states well-defined, we require N_x to be as large as possible so it is not easy to overcome the computational cost.

Another method is performing the substitution $k_\perp \rightarrow -i\partial_\perp$ to the continuum limit of the tight-binding Hamiltonian, where $\perp$ indicates the surface normal direction. Unlike the construction of the finite-sized Hamiltonian, this method starts from the bulk Hamiltonian. Thus this method has a strong advantage to the finite-sized system method that one can analytically study the characteristics of the boundary states. Due to this advantage, this method has been widely used to study the boundary states of the topological materials [19, 46, 47]. However, this method has clear limitations as well. Firstly, this method only applies to the continuum limit and thus only the band structure near a certain point can be investigated. Secondly, this method is not universal. Depending not only on the Hamiltonian but also on the boundary conditions, one should solve different differential equations and this is usually a difficult task.

Lastly, we introduce a quick iterative method to obtain the boundary band states utilizing the surface Green's function. We will follow Refs. [48, 49] below. Similar to the finite-sized Hamiltonian method, we construct a Hamiltonian with the boundary using the bulk Hamiltonian. However, this time, we focus on the Green's function. We will show that we can obtain the boundary contribution of the Green's function of the semi-infinite system with a time complexity proportional to $\log_2 N_x$, which converges much faster than directly solving the finite-sized Hamiltonian.

Let us consider a 3D system. For other dimensions, the discussion is similar. We firstly construct a finite-sized Hamiltonian with m-unit-cell-long along $\mathbf{r}_\perp$ direction from the $n \times n$ bulk Hamiltonian, where the basis is given by

$$\Psi(\mathbf{k}_\parallel) = [\phi^{11}, \phi^{12}, \cdots, \phi^{1n}, \cdots, \phi^{m1}, \phi^{m2}, \cdots, \phi^{mn}]^T, \tag{2.5}$$

and $\phi^{ij}(\mathbf{k}_{\|})$ is j-th atomic orbital in the i-th unit cell along the finite-length direction. For convenience, we introduce the concept called the “principal layer”. A principal layer is formed by a group of atomic layers in such a way that only nearest-interlayer coupling between principal layers exist. Then the finite-sized Hamiltonian which is constructed from a n-band bulk Hamiltonian and has n_{prin} unit cells per a principal layer would be expressed by

$$H_{\text{fin}}(\mathbf{k}_{\|}) = \begin{pmatrix} H_{00} & H_{01} & 0 & 0 & 0 & \cdots \\ H_{10} & H_{11} & H_{12} & 0 & 0 & \cdots \\ 0 & H_{21} & H_{22} & H_{23} & 0 & \cdots \\ 0 & 0 & H_{32} & H_{33} & H_{34} & \cdots \\ 0 & 0 & 0 & H_{43} & H_{44} & \cdots \\ \vdots & \vdots & \vdots & \vdots & \vdots & \ddots \end{pmatrix}, \tag{2.6}$$

where $H_{ij}(\mathbf{k}_{\|})$ is the $(n \times n_{\text{prin}}) \times (n \times n_{\text{prin}})$ block matrix that contains the hopping between i-th and j-th principal layers and 0-th layer is the outermost principal layer. By the definition of the principal layer, $H_{ij} = 0$ for $|i - j| > 1$.

We now consider the Green’s function of the finite-sized Hamiltonian, which is defined by

$$[\omega - H_{\text{fin}}(\mathbf{k}_{\|})]G(\mathbf{k}_{\|}, \omega) = I. \tag{2.7}$$

Similar to the H_{ij} in Eq. (2.6), we define G_{ij} by the block in the Green’s function G that corresponds to the coupling between orbitals in i-th and j-th principal layer. Then we get the following equations from the first column of Eq. (2.7):

$$\begin{aligned}
(\omega - H_{00})G_{00} &= I + H_{01}G_{10} \\
(\omega - H_{00})G_{10} &= H_{01}^{\dagger}G_{00} + H_{01}G_{20} \\
&\vdots \\
(\omega - H_{00})G_{n0} &= H_{01}^{\dagger}G_{n-1,0} + H_{01}G_{n+1,0}
\end{aligned} \tag{2.8}$$

Here, for simplicity, we made an assumption of an ideal surface, i.e., $H_{00} = H_{11} = \cdots$ and $H_{01} = H_{12} = H_{23} = \cdots$. After some algebra, one can derive the following equations from Eq. (2.8):

$$\begin{aligned}
G_{10} &= t_0G_{00} + \tilde{t}_0G_{20} \\
G_{20} &= t_1G_{00} + \tilde{t}_1G_{40} \\
&\vdots \\
G_{2^n0} &= t_nG_{00} + \tilde{t}_nG_{2^{n+1}0},
\end{aligned} \tag{2.9}$$

where

$$\begin{aligned}
t_i &= (I - t_{i-1}\tilde{t}_{i-1} - \tilde{t}_{i-1}t_{i-1})^{-1}t_{i-1}^2 \\
\tilde{t}_i &= (I - t_{i-1}\tilde{t}_{i-1} - \tilde{t}_{i-1}t_{i-1})^{-1}\tilde{t}_{i-1}^2
\end{aligned} \tag{2.10}$$

and

$$
\begin{aligned}
t_0 &= (\omega - H_{00})^{-1} H_{01}^{\dagger} \\
\tilde{t}_0 &= (\omega - H_{00})^{-1} H_{01}.
\end{aligned}
\tag{2.11}
$$

From Eq. (2.9), we get

$$G_{10} = (t_0 + \tilde{t}_0 t_1 + \tilde{t}_0 \tilde{t}_1 t_2 + \cdots) G_{00} + \tilde{t}_n G_{2^{n+1}0}. \tag{2.12}$$

Since $G_{2^{n+1}0} \to 0$ very rapidly as n increases, we get $G_{10} \sim T G_{00}$ for large n, where the transfer matrix T is given by

$$T = t_0 + \tilde{t}_0 t_1 + \tilde{t}_0 \tilde{t}_1 t_2 + \cdots + \tilde{t}_0 \tilde{t}_1 t_2 \tilde{t}_3 \cdots \tilde{t}_{n-1} t_n. \tag{2.13}$$

Finally, by putting $G_{10} = T G_{00}$ into Eq. (2.8), we get the surface contribution G_{00} of the Green's function,

$$G_{00} = (\omega - H_{00} - H_{01} T)^{-1}. \tag{2.14}$$

We can extract some information of the system from Eq. (2.14). One of the simplest and the most important example is the spectral density of the surface states:

$$N(\mathbf{k}_{\parallel}, \epsilon) = -\frac{1}{\pi} \mathrm{Tr}\, G_{00}(\mathbf{k}_{\parallel}, \epsilon + i\eta). \tag{2.15}$$

Before we end this section, we demonstrate how to get that the edge

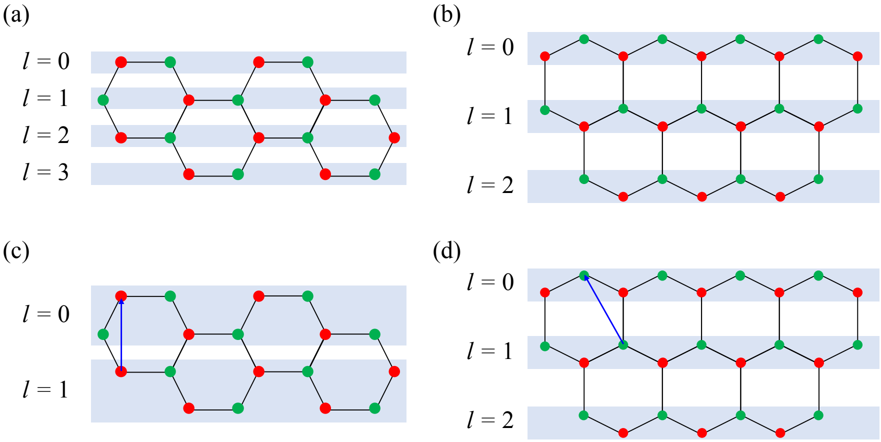

Figure 2.4: Principal layers of graphene with (a) the armchair edges and (b) the zigzag edges when only the nearest neighbor hoppings are considered. (c,d) Principal layers of graphene with the next nearest neighbor hoppings. Here, the red and green colors indicate the two inequivalent sites in a graphene unit cell.

state of a monolayer graphene using the Green's function method as an example. The simplest tight-binding model Hamiltonian for a monolayer consists of only the nearest neighbor hopping terms, which is given by

$$H = \begin{pmatrix} 0 & f(k) \\ f^{\dagger}(k) & 0 \end{pmatrix}, \tag{2.16}$$

where $f(\mathbf{k}) = -t_0[e^{\frac{ik_y a}{\sqrt{3}}} + 2\cos(\frac{k_x a}{2})e^{\frac{-ik_y}{2\sqrt{3}}}]$. We consider two kinds of edges of graphene. One is the armchair edge and the other is zigzag edge, which are shown in the uppermost edges of Figs. 2.4(a) and 2.4(b), respectively. Since we only consider the nearest neighbor hoppings, the principal layers are easily determined as shown in Figs. 2.4(a) and 2.4(b). What if the next nearest neighbor hopping terms, the hopping between two red sites or two green sites [shown as blue arrows in Figs. 2.4(c) and 2.4(d)], are considered? In the case of the armchair edges, the number of layers in a principal layer is doubled, as the blue arrow in Fig. 2.4(c) corresponds to the hopping between $l = 0$ and $l = 2$ in Fig. 2.4(a). On the other hand, the number of layers in a principal layer remains the same in the case of the zigzag edges.

Once we set the principal layers, one can straightforwardly get H_{00} and H_{01} from the geometry given in Fig. 2.4. For the armchair edges, we have

$$H_{00} = -t_0 \begin{pmatrix} 0 & 1 \\ 1 & 0 \end{pmatrix}, \quad H_{01} = -t_0 \begin{pmatrix} 0 & 1 \\ e^{-ik_x\sqrt{3}a} & 0 \end{pmatrix}, \tag{2.17}$$

and for the zigzag edges, we have

$$H_{00} = -t_0 \begin{pmatrix} 0 & 1+e^{-ik_xa} \\ 1+e^{ik_xa} & 0 \end{pmatrix}, \quad H_{01} = -t_0 \begin{pmatrix} 0 & 0 \\ 1 & 0 \end{pmatrix}. \tag{2.18}$$

Putting the equations into Eqs. (2.14) and (2.15), we can get the edge spectral densities of the armchair and the zigzag edges, which are shown in Fig. 2.5. We see only the bulk band projection in Fig. 2.5(a). However in Fig. 2.5(b), we can observe the zero edge modes indicated by the white arrows, which is a famous characteristic of the zigzag edge graphene.

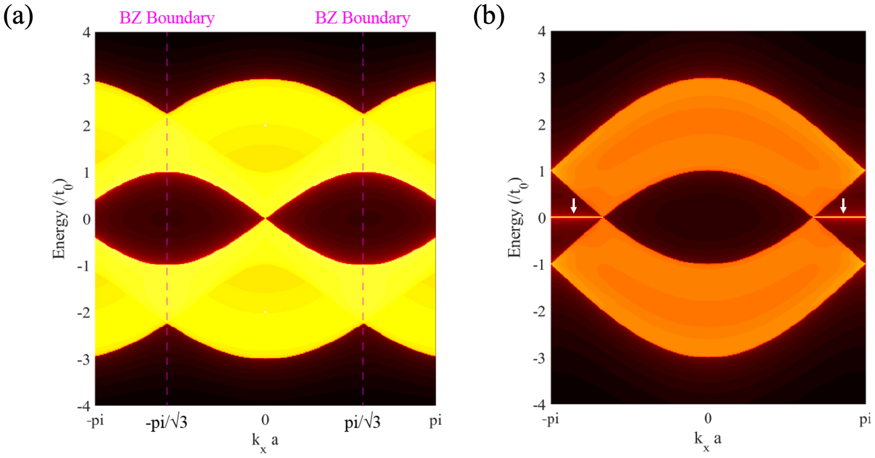

Figure 2.5: Edge spectral densities of (a) the armchair and (b) the zigzag edges.

Chapter 3

Topological phases in quasi-one-dimensional bismuth halides Bi_4X_4 (X = I, Br)

3.1 Introduction

Geometry, symmetry, topology, and interaction are fundamental themes in physics. Their interplay governs microscopic laws of individual particles and macroscopic phenomena of many-particle systems. As a paradigm in condensed matter physics, Kane-Mele topological insulators (TI) exist in 2D and 3D but not in 0D and 1D, dictated by the time-reversal ($\mathcal{T}$) and gauge symmetries in spin-orbit-coupled systems [8, 16, 17, 50]. For a 3D (2D) TI, the nontrivial $\mathbb{Z}_2$ topological invariant of a gapped bulk state implies the presence of a symmetry-protected gapless 2D (1D) surface (edge) state. Having taken the electronics community by storm, not only has this spirit topologically classified all insulators, (semi-)metals, and superconductors with various different symmetries and dimensions [13, 51–53], but it has also substantially inspired the study of classical systems that address photonic, acoustic, mechanical, and even equatorial waves [54–58].

Fascinatingly, higher-order TIs (HOTI) and topological superconductors have emerged recently [33–43]. They host protected gapless states at boundaries of more than one dimension lower. In fact, they can be best exemplified by simple models of $\mathbb{Z}_2$ TIs under suitable symmetry breaking. In the original work by Zhang, Kane, and Mele (ZKM) [33], when the $\mathcal{T}$ symmetry is broken for a 3D TI, one chiral hinge mode propagates along any hinge that reverses the sign of Hall conductivity of two magnetic gapped surfaces. In more recent studies, when the gauge symmetry is broken for a 2D TI, two Majorana corner modes are bound to any corner that reverses the sign of induced pairing of two superconducting gapped edges [41, 42]. While the former may be realized in Sm-doped $\mathrm{Bi_2Se_3}$ or $\mathrm{MnBi_{2\mathit{n}}Te_{3\mathit{n}+1}}$ in a magnetic field, its thin-film limit as the first quantum anomalous Hall effect has been achieved in Cr-doped $\mathrm{(Bi,Sb)_2Te_3}$ [59–62]. While the latter may be materialized in the 112-family of iron pnictides such as $\mathrm{Ca_{1-\mathit{x}}La_{\mathit{x}}FeAs_2}$, its 3D counterpart with helical Majorana hinge modes has appeared to be confirmed in $\mathrm{FeTe_{0.55}Se_{0.45}}$ [63–65]. HOTIs also have been realized in experiments by engineering the systems like electric circuits [66, 67], photonic crystals [68–70], and sonic crystals [71–73]. Moreover, HOTIs have been experimentally verified in pure materials, bismuth [39] and $\mathrm{MTe_2}$ (M=W, Mo) [43, 74, 75], although both are semimetals. These progresses urge a more ambitious question: does there exist any *pristine* HOTI, i.e., a material with a *global* bulk band gap and a *natural* gapless hinge state in the *absence* of any symmetry-breaking perturbation?

Following the theory of topological quantum chemistry or symmetry indicators [26–28, 76, 77], high-throughput screening of nonmagnetic topological materials has been performed in the Inorganic Crystal Structure Database [78], and thousands of candidates have been identified [29–31]. Unfortunately, only a handful of them are HOTIs with helical hinge states. According to the high-throughput screening calculations [29], the list of most plausible candidates for HOTIs with global band gaps and helical hinge states includes α-Bi_4Br_4 (but not α-Bi_4I_4), KHgSb (with hourglass surface states), Bernal graphite (with a band gap $\sim$ 0.025 meV), IV-VI semiconductors (with Dirac surface states) and BaTe in rocksalt structure, $ThTaN_3$ in perovskite structure, $La_2Hf_2O_7$ in pyrocholore structure, and antiperovskite oxides A_3BO (A = Ca, Sr, Ba, Yb and B = Ge, Sn, Pb)[1]. Even though the list is short, extra efforts including more accurate calculations and more physical understanding are necessary to narrow down it to those not only truly topological but also experimentally feasible [79]. As a rare yet prime example, it has been predicted that α-Bi_4Br_4 is a HOTI with $\mathbb{Z}_4 = 2$ whereas α-Bi_4I_4 has completely trivial symmetry indicators [29–31, 80, 81]. In this chapter, by using various of different computational and analytical approaches, we explicitly demonstrate that both α-Bi_4Br_4 and α-Bi_4I_4 are HOTIs with helical hinge states, though with sharp distinction in their hinge state patterns. Given that the symmetry indicators of α-Bi_4I_4 are indeed trivial, significantly, our results imply that there are likely to be many topological materials beyond the scope of the current scheme for the classification of topological materials like symmetry indicators or topological quantum chemistry and awaiting to be discovered.

Bi_4X_4 (X = Br, I) are quasi-1D van der Waals materials, and each can be viewed as a periodic stack of atomic chains. In the case of Bi_4I_4, two phases are found to be stable [82], where the low- and high-temperature phases are called α-Bi_4I_4 and β-Bi_4I_4, respectively. On the other hand, only one phase has been observed in Bi_4Br_4 so far, but recently, the crystal that substituted iodine with bromine in β-Bi_4I_4 has been theoretically demonstrated to be stable [83]. We refer to the former phase as α-Bi_4Br_4 and the later phase as β-Bi_4Br_4. The β phase has been predicted as a prototype weak TI (WTI) [83], as confirmed by angle-resolved photoemission spectroscopy (ARPES) [84]. Strain can further tune the β phase between WTI, strong TI (STI), and normal insulator [83]. Superior to layered WTIs, the quasi-1D WTI is granted two natural cleavage surfaces in which the distinct surface hallmarks defining WTI can be inspected [83]. Here we show that our revealed hinge states of the two α phases propagate along the natural cleavage hinges, i.e., in the chain direction. This extraordinary property would greatly facilitate the experimental detections of the hinge states. Interestingly, intrinsic superconductivity has already been reported for both Bi_4Br_4 and Bi_4I_4 [85–88]. This enables possible topological superconductivity to arise from an intrinsic proximity effect. More remarkably for Bi_4I_4, the structural transition turns out to be around 300 K [82, 84, 89–91]. Thus, our identifying α-Bi_4I_4 as a HOTI not only uncovers a thermal phase transition between the first- and second-order TIs but also implies that the topological surface/hinge states of Bi_4I_4 can be switched at room temperature, a property that may be exploited for potential applications.

---

[1] Hongming Weng (private communication).

This chapter is organized as follows. In Sec. 3.2, we discuss the crystal structures of $\mathrm{Bi_4X_4}$. Starting from the simplest β-$\mathrm{Bi_4X_4}$, we investigate the more complicated crystal structures of α-$\mathrm{Bi_4Br_4}$ and α-$\mathrm{Bi_4I_4}$. In the end of Sec. 3.2, we remark the atomic dimerization pattern along the (001) direction which is closely related to HOTI phases. In Sec. 3.3, we discuss the low energy band structures based on the density functional theory (DFT) calculation. We explain the band evolution at various stages and show that the band inversions that make $\mathrm{Bi_4X_4}$ system topological are driven by the spin-orbit coupling (SOC). Based on the crystal structures and the low-energy electronic band structures, we construct the effective tight-binding (TB) models for $\mathrm{Bi_4X_4}$ in Sec. 3.4. We first construct the effective TB model of a (001) layer of $\mathrm{Bi_4X_4}$, which serves as a building block of the 3D $\mathrm{Bi_4X_4}$. Then we construct the effective TB model for the simplest stacking of (001) layers, β-$\mathrm{Bi_4X_4}$, and derive the effective TB model for the α phases based on the β phases. In Sec. 3.5, we investigate the bulk band topology using the symmetry-based indicators [26, 27, 77]. From our observation that the α phases can be derived from the β phases by the unit cell doubling in the real space or the Brillouin zone-folding in the reciprocal space, we explain the bulk-obstructed HOTI phase in α-$\mathrm{Bi_4Br_4}$ and the triviality of α-$\mathrm{Bi_4I_4}$ in the periodic boundary conditions. In Sec. 3.6, we investigate the boundary states of $\mathrm{Bi_4X_4}$. Here we demonstrate that the 3D bulk band analysis like the symmetry-based indicator cannot explain the non-trivial boundary states. Especially we show that α-$\mathrm{Bi_4I_4}$ exhibit topological hinge states even though its 3D bulk Hamiltonian is trivial. Since the non-trivial topology of $\mathrm{Bi_4X_4}$ cannot be fully captured by the periodic 3D bulk Hamiltonian, we analyze the band topology at the surface Hamiltonian in Sec. 3.7. We observe the analogy between the surface Hamiltonians of α-Bi_4X_4 and the celebrated Su-Schrieffer-Heeger (SSH) model [92]. Motivated by the SSH model, we introduce surface topological invariants which can fully capture the topological boundary states in α-Bi_4X_4. Finally in Sec. 3.8, we discuss one of our recent experimental projects on Bi_4X_4 which strongly supports our theory.

This chapter is largely based on my publications, Refs. [45, 93].

3.2 Crystal structures

Both the α and β phases of Bi_4X_4 crystallize in the same monoclinic space group C^3_{2h} ($C2/m$). They have three spatial symmetries: inversion ($\mathcal{P}$), (010) mirror reflection ($\mathcal{M}_b$), and twofold rotation around the $\boldsymbol{b}$ axis ($\mathcal{C}_2$). Given that $\mathcal{C}_2 = \mathcal{M}_b\mathcal{P}$, only two of the three symmetries are independent. The building block of Bi_4X_4 is an atomic chain with strongly covalent bonds between bismuth atoms. Each chain consists of four inequivalent Bi atoms and four inequivalent X atoms. As shown in Fig. 3.1(a), the two internal (external) Bi atoms are denoted by $\mathrm{Bi_{in}}$ and $\mathrm{Bi'_{in}}$ ($\mathrm{Bi_{ex}}$ and $\mathrm{Bi'_{ex}}$), and the angles between different Bi-Bi bonds are denoted by four θ's. The chains are oriented in the $\boldsymbol{b}$ direction and stacked via the van der Waals forces in the $\boldsymbol{a}$ and $\boldsymbol{c}$ directions [82, 83, 94].

We note that Bi_4X_4 has two natural cleavage surfaces. For β-Bi_4Br_4, the inter-layer binding energy for the (001) and (100) planes are respectively

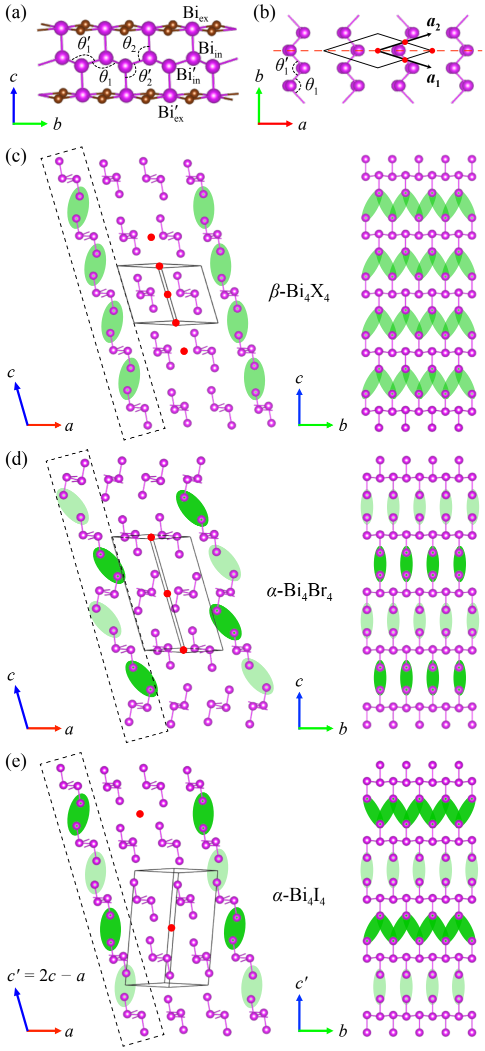
(a)
Bi_ex
θ′_1
θ_2
Bi_in
θ_1
θ′_2
Bi′_in
Bi′_ex
c
b
(b)
a_2
a_1
θ′_1
θ_1
b
a
(c)
β-Bi_4X_4
c
a
c
b
(d)
α-Bi_4Br_4
c
a
c
b
(e)
α-Bi_4I_4
c′ = 2c − a
a
c′
b

Figure 3.1: (a) An atomic chain as the building block of $\mathrm{Bi_4X_4}$. The purple (brown) balls are the Bi (X) atoms. (b) A (001) monolayer of $\mathrm{Bi_4X_4}$. The black diamond is a primitive unit cell. The red dots are possible inversion centers. The dashed red line is a mirror plane. (c)-(e) Left panels: the bulk structures of β-$\mathrm{Bi_4X_4}$, α-$\mathrm{Bi_4Br_4}$, and α-$\mathrm{Bi_4I_4}$ viewed from the $\bar{\boldsymbol{b}}$ axis. The solid black lines sketch the primitive unit cells. The X atoms are omitted for better illustration. The green bubbles indicate the dimerization patterns of the NN inter-edge tunnelings. The red dots are possible inversion centers. Right panels: the side monolayers in the dashed black frames in the left panels viewed from the $\boldsymbol{a}$ axis.

20 and 25 meV/Å^2 (slightly larger than that of graphite and smaller than that of MoS_2) [83]. These values are consistent with the fact that for the interchain distances c is slightly larger than $a/2$ as detailed in Appendix A.1. For the other three materials, the binding energies are in the same range. Nevertheless, this unique property of quasi-1D materials highlights the β phase as a prototype WTI [83] that bears surface selective hallmarks. Moreover, the absence of dangling bonds for hinges between the two cleavage surfaces renders the two α phases ideal platforms for exploring HOTIs that host helical hinge states.

3.2.1 Crystal structure of β-Bi_4X_4

While β-Bi_4I_4 has been experimentally synthesized [82, 84, 95], β-Bi_4Br_4 is a designed material [83] based on the same crystal structure of β-Bi_4I_4. The dynamic stability of β-Bi_4Br_4 has been demonstrated through the phonon spectrum calculations [83]. Nevertheless, their detailed crystal structure data are provided in Appendix A.1.

Each atomic chain is inversion symmetric in β-Bi_4X_4, as seen in Fig. 3.1(a). Under inversion, the $\mathrm{Bi_{in}}$ and $\mathrm{Bi_{ex}}$ atoms are reflected into the $\mathrm{Bi'_{in}}$ and $\mathrm{Bi'_{ex}}$ atoms, respectively. In addition, each chain is mirror-symmetric with respect to any (010) plane that contains the Bi atoms. The mirror and inversion symmetries dictate that $\theta_1 = \theta'_1$ and $\theta_2 = \theta'_2$, respectively.

Each (001) monolayer of β-Bi_4X_4 consists of equally spaced atomic chains in the $\boldsymbol{a}$ direction, as shown in Fig. 3.1(b). Two adjacent chains are displaced from each other by constant vectors $a_{1,2} = (\boldsymbol{a} \mp \boldsymbol{b})/2$. The monolayer is inversion- and mirror-symmetric, with the same inversion centers and mirror planes as its individual chains. In addition to the intra-chain inversion centers off the mirror planes, there exist inter-chain inversion centers in the mirror planes between two adjacent chains, as shown in Fig. 3.1(b). It follows that the monolayer is also invariant under a twofold rotation ($\mathcal{C}_2 = \mathcal{M}_b\mathcal{P}$) around the $\boldsymbol{b}$ axis across the inter-chain inversion centers.

As shown in Fig. 3.1(c), bulk β-Bi$_4$X$_4$ is a periodic stack of (001) layers in the $\boldsymbol{c}$ axis, which is normal to the $\boldsymbol{b}$ axis and 107.87° (β in Appendix A.1) above the $\boldsymbol{a}$ axis. Given that $\boldsymbol{c} \perp \boldsymbol{b}$, the bulk crystal has the same mirror planes as its individual monolayers. Remarkably, the bulk inversion center of β-Bi$_4$X$_4$ can be placed not only in a (001) layer but also in the middle of two adjacent layers, and likewise the twofold rotation axis.

3.2.2 Crystal structure of α-Bi$_4$Br$_4$

Each (001) monolayer of α-Bi$_4$Br$_4$ has the same crystal structure as that of β-Bi$_4$X$_4$, except for the slightly different lattice constants and intra-chain parameters listed in Appendix A.1. Unlike β-Bi$_4$X$_4$, two adjacent layers are not related by any symmetry, as shown in Fig. 3.1(d). For instance, although the two layers have the same inter-chain distance in the $\boldsymbol{a}$ axis, the key intra-chain parameters θ's are different for the two layers. As a result, the primitive unit cell consists of two (001) layers. Bulk α-Bi$_4$Br$_4$ has the same symmetries as β-Bi$_4$X$_4$: inversion, (010) mirror reflection, and twofold rotation around the $\boldsymbol{b}$ axis. However, the inversion center and the rotational axis of bulk α-Bi$_4$Br$_4$ can only be placed in a (001) layer. The detailed crystal structure data are provided in Appendix A.1.

3.2.3 Crystal structure of α-Bi$_4$I$_4$

For each atomic chain of α-Bi$_4$I$_4$, the (010) mirror symmetry is preserved such that $\theta_1 = \theta_1'$, whereas the inversion symmetry is broken as indicated by $\theta_2 \neq \theta_2'$. Even for a (001) monolayer of α-Bi$_4$I$_4$, only the mirror symmetry is present. For bulk α-Bi$_4$I$_4$, however, the inversion and twofold rotational symmetries are restored, as each symmetry relates two adjacent layers. Similar to α-Bi$_4$Br$_4$, the primitive unit cell of α-Bi$_4$I$_4$ consists of two (001) layers. Different from α-Bi$_4$Br$_4$, the inversion center and the rotational axis of bulk α-Bi$_4$I$_4$ can only be placed in the middle of two adjacent layers.

Bulk α-Bi$_4$I$_4$ exhibits a clear difference from the other three materials in how the (001) layers are stacked, as shown in Fig. 3.1(e). This is best indicated by the angle between the $\boldsymbol{c}$ and $\boldsymbol{a}$ axes, $\beta = 87.04^{\circ}$[2], which is significantly different from $\sim 107^{\circ}$ of the other three materials. If $\boldsymbol{c}' = 2\boldsymbol{c} - \boldsymbol{a}$ was the primitive lattice vector, the stacking direction would be the same as the other three materials, but there would be four layers per primitive unit cell. Nevertheless, there exists a shorter inter-layer lattice vector $\boldsymbol{c}$, and the true primitive unit cell only contains two layers. As such, the natural cleavage surface of α-Bi$_4$I$_4$, corresponding to the (100) surface of the other three materials, is the (201) surface [82]. The detailed crystal structure data are provided in Appendix A.1.

---

[2] Note that β can be either 87.04° or 92.96° for α-Bi$_4$I$_4$, and that conventionally the obtuse angle is chosen. Here we choose $\beta = 87.04^{\circ}$ instead for the consistency with the coordinates of the other three materials.

3.2.4 Atomic dimerization in α-Bi$_4$X$_4$

From the crystal structures in Fig. 3.1, the dimerization patterns at the side surfaces can be visualized clearly. For β-Bi$_4$X$_4$ in Fig. 3.1(c), the NN inter-edge tunnelings are the same at both the (100) and ($\bar{1}$00) side surfaces between any two adjacent (001) layers. Thus, the two surfaces share the same dimerization pattern resembling the critical point of the SSH model. For α-Bi$_4$Br$_4$ in Fig. 3.1(d), the highlighted NN inter-layer tunnelings are the same in the bulk between any two adjacent (001) layers. At the (100) and ($\bar{1}$00) side surfaces, however, the closer the Bi$_{\text{ex}}$/Bi$'_{\text{ex}}$ atoms are to the vacuum, the weaker their tunnelings are. This leads to opposite dimerization patterns at the two side surfaces. By sharp contrast, for α-Bi$_4$I$_4$ in Fig. 3.1(e), the highlighted NN inter-layer tunnelings are even evidently different in the bulk. It follows that the dimerization patterns at the (201) and ($\bar{2}0\bar{1}$) side surfaces are the same. This atomic dimerization plays a crucial role in the formation of topological hinge states in α-Bi$_4$X$_4$, which will be discussed in Sec. 3.7.

3.3 Low-energy band structures

With the crystal structures of $\mathrm{Bi_4X_4}$ in Fig. 3.1 and Appendix A.1, we carry out the DFT calculations to obtain their electronic band structures and analyze their topological band properties. The DFT calculations were performed by using the projector augmented wave method implemented in the Vienna *ab initio* simulation package [96] and the Perdew-Burke-Ernzerhof parametrization of the generalized gradient approximation for the exchange correlation potential [97, 98]. In order to obtain more accurate band gaps and band inversions, we apply the more sophisticated Heyd-Scuseria-Ernzerhof (HSE) hybrid functional method [99] to the calculations. We employ the DFT results and the Wannier90 code [100–102] to construct the maximally localized Wannier functions (MLWF) for the p orbitals of Bi and halogens. Based on the MLWF, we derive the electronic band structures in Figs. 3.6 and 3.8 for finite-size systems. The methods here are the same as those in our previous work [83]. Figure 3.2 displays the bulk band structures and band inversions for β-$\mathrm{Bi_4Br_4}$, α-$\mathrm{Bi_4Br_4}$, α-$\mathrm{Bi_4I_4}$, and β-$\mathrm{Bi_4I_4}$.

To better understand the physical mechanism of the non-trivial topology in $\mathrm{Bi_4X_4}$ family, now we explain the band evolution of $\mathrm{Bi_4X_4}$ at various stages [83, 103]. We first elucidate the case for the β phase and then generalize it to the α phase, as illustrated in Fig. 3.3.

Due to the large electronegativity of halogen atoms, the bands near the Fermi energy are mainly determined by the $6p$ orbitals of bismuth atoms. First, consider the (010) mirror symmetry. The p_y orbitals are decoupled

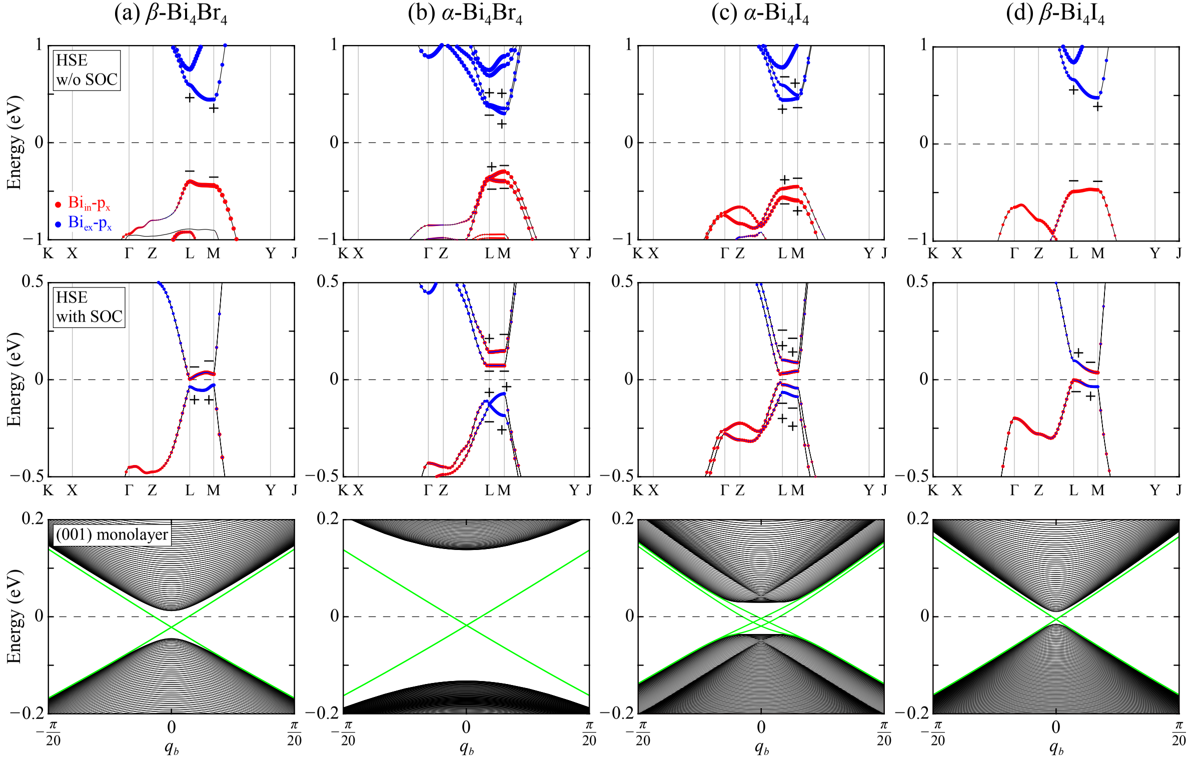

Figure 3.2: The 3D bulk and (001) monolayer ribbon band structures of (a) β-Bi$_4$Br$_4$, (b) α-Bi$_4$Br$_4$, (c) α-Bi$_4$I$_4$, and (d) β-Bi$_4$I$_4$. The SOC is not included in the top panels but included in the middle and bottom panels. The size of red (blue) dots indicates the weight of the p_x orbital of $\mathrm{Bi}_{\mathrm{in}}$ ($\mathrm{Bi}_{\mathrm{ex}}$) atoms. The ± signs label the inversion eigenvalues at the L and M points, with the inversion centers in (001) layers in (a), (b), and (d) but in the middle of two adjacent layers in (c). The green lines are the helical edge states (degenerate for two edges in (a), (b), and (d)), implying that the four (001) monolayers are all 2D $\mathbb{Z}_2$ TIs.

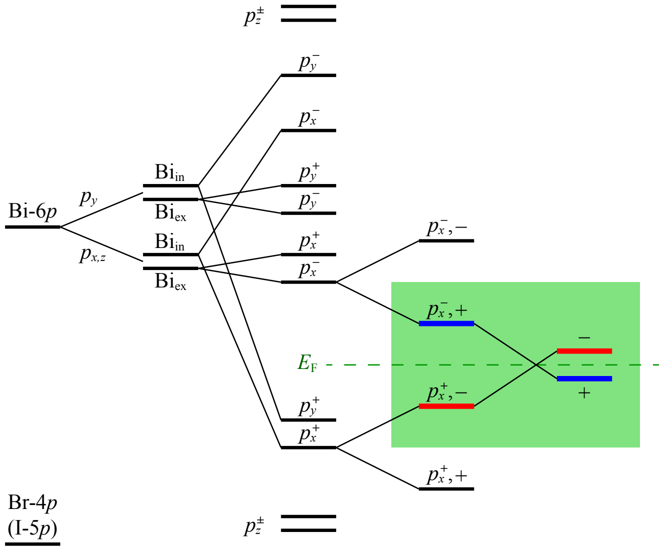

Figure 3.3: The band evolution at the L and M points near the Fermi energies of $\mathrm{Bi_4X_4}$. From left to right, we consider the electronegativity of the atomic orbitals, the splitting due to the (010) mirror symmetry, the formation of bonding and anti-bonding states as a result of the intra- and inter-chain couplings, and the possible band inversion driven by the SOCs. The details are explained in the text.

from the $p_{x,z}$ orbitals since their mirror eigenvalues are different. Given the atomic chain orientation, the energies of p_y orbitals are higher than those of $p_{x,z}$ orbitals; the hopping between p_y orbitals is of σ-type, whereas that between $p_{x,z}$ orbitals is of π-type. Then, consider the inversion symmetry in a chain. $\mathrm{Bi_{in/ex}}$ and $\mathrm{Bi'_{in/ex}}$ atoms are reflected to each other under inversion. They form the bonding and anti-bonding states split in energy: $|\mathrm{Bi_{in/ex}}, p_i^{\pm}\rangle = (|\mathrm{Bi_{in/ex}}, p_i\rangle \pm |\mathrm{Bi'_{in/ex}}, p_i\rangle)/\sqrt{2}$, where $i = x, y, z$.

Next, we count the stronger intra-chain couplings. Because of the short $\mathrm{Bi_{in}}$-$\mathrm{Bi'_{in}}$ distance, the energy splittings between states $|\mathrm{Bi_{in}}, p_x^{\pm}\rangle$ and between states $|\mathrm{Bi}_{\mathrm{in}}, p_y^{\pm}\rangle$ are large. On the contrary, the large $\mathrm{Bi}_{\mathrm{ex}}$-$\mathrm{Bi}'_{\mathrm{ex}}$ distance results in negligible energy splittings. However, states $|\mathrm{Bi}_{\mathrm{ex}}, p_{x,y}^{\pm}\rangle$ can be coupled to states $|\mathrm{Bi}_{\mathrm{in}}, p_{x,y}^{\pm}\rangle$ via the π-bonding and acquire splittings in the opposite fashion of $|\mathrm{Bi}_{\mathrm{in}}, p_{x,y}^{\pm}\rangle$. Due to the σ-bonding between states $|\mathrm{Bi}_{\mathrm{in}}, p_z^{\pm}\rangle$ and $|\mathrm{Bi}_{\mathrm{ex}}, p_z^{\pm}\rangle$, the p_z orbitals split and shift far away from the Fermi energy.

Moreover, we take into account the weaker inter-chain couplings. As the chains are closer in the $\boldsymbol{a}$ direction than in the $\boldsymbol{c}$ direction, the energy splitting mainly occurs within each (001) layer due to the couplings in the $\boldsymbol{a}$ direction. Two adjacent chains in the same layer can be related by the inversion symmetry, and their states $|\mathrm{Bi}_{\mathrm{in/ex}}, p_x^{\pm}\rangle$ form the bonding and anti-bonding states $|\mathrm{Bi}_{\mathrm{in/ex}}, p_x^{\pm}, \pm\rangle$, where the new $\pm$ signs denote the inversion eigenvalues. As a results, the states $|\mathrm{Bi}_{\mathrm{in}}, p_x^{+}, -\rangle$ and $|\mathrm{Bi}_{\mathrm{ex}}, p_x^{-}, +\rangle$ become the valence and conduction bands closest to the Fermi energy, respectively.

Finally, we include the effect of spin-orbit couplings (SOC). The SOCs mix the p_x orbitals with the $p_{y,z}$ orbitals that have the same inversion eigenvalues. As a result, band inversions occur near the Fermi energy at either one or both of the two TRI momenta L and M, and $\mathrm{Bi_4X_4}$ become topologically nontrivial.

The above picture for the β phase equally applies to α-$\mathrm{Bi_4Br_4}$, as its inversion center is also in a (001) layer. For α-$\mathrm{Bi_4I_4}$, as its inversion center is in the middle of two adjacent layers instead, the two pairs of $\pm$ signs above should be both interpreted as the labels of bonding and anti-bonding states.

(a) β-Bi$_4$Br$_4$ (b) α-Bi$_4$Br$_4$

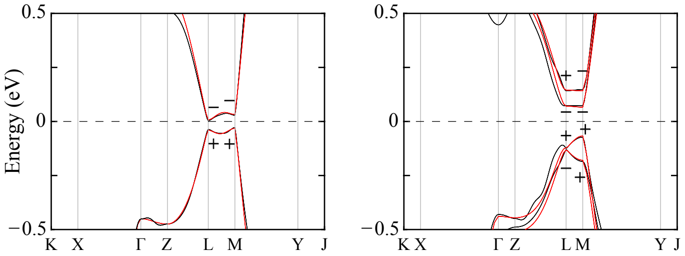

(c) α-Bi$_4$I$_4$ (d) β-Bi$_4$I$_4$

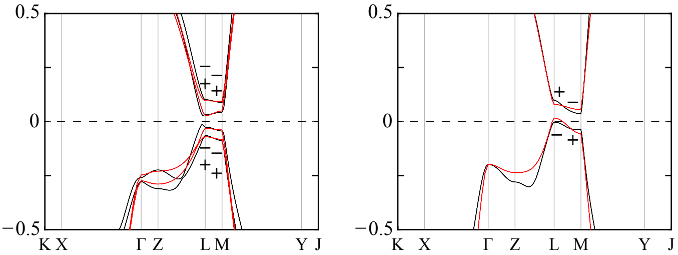

Figure 3.4: The band structures (black) and band inversions (±) of (a) β-Bi$_4$Br$_4$, (b) α-Bi$_4$Br$_4$, (c) α-Bi$_4$I$_4$, and (d) β-Bi$_4$I$_4$ in Fig. 3.2 fitted by our effective tight-binding models (red) evaluated by the set of parameter values in Appendix A.2.

For this reason, the NN inter-chain couplings along the $\boldsymbol{c}$ direction needs to be further considered for states $|\mathrm{Bi}_{\mathrm{in}}, p_x^+, -\rangle$ and $|\mathrm{Bi}_{\mathrm{ex}}, p_x^-, +\rangle$ to form the inversion eigenstates that are eventually band-inverted by the SOCs.

3.4 Effective tight-binding models

We construct the effective tight-binding model for both α- and β-Bi$_4$X$_4$ based on their crystal and band structures revealed in Secs. 3.2 and 3.3. We start from the construction of the WTI model for the β phase and then derive the models for the two distinct α phases by applying zone folding and Peierls distortion. With reasonable sets of parameter values in Appendix A.2, our models well fit the band inversions and band structures of the DFT data, as shown in Fig. 3.4.

3.4.1 β-Bi$_4$X$_4$ model

We choose a basis in which the three spatial symmetries discussed in Sec. 3.2 and the $\mathcal{T}$ symmetry can be specified as follows:

$$\mathcal{P} = \sigma_z, \;\; \mathcal{M}_b = is_y, \;\; \mathcal{C}_2 = \mathcal{M}_b\mathcal{P}, \;\; \mathcal{T} = i\mathcal{K}s_y, \tag{3.1}$$

where $\mathcal{K}$ is the complex conjugation. As such, the low-energy model for β-Bi$_4$X$_4$ can be built by using the four basis states $|+,\uparrow\rangle$, $|+,\downarrow\rangle$, $|-,\uparrow\rangle$, and $|-,\downarrow\rangle$, where $\pm$ and $\uparrow / \downarrow$ denote the eigenvalues of σ_z and s_z, respectively. As illustrated in Fig. 3.3, the $|\sigma_z = \pm\rangle$ states are mainly from the p_x orbitals of Bi$_{\text{in/ex}}$ atoms, and the $|s_z = \uparrow / \downarrow\rangle$ states are dominated by the electron spins.

We further assume that the four basis states are localized in (001) layers and consider only the NN (intra-layer) intra-chain, NN (intra-layer) inter-chain, and NN inter-layer (inter-chain) hopping processes, as well as the onsite potentials. It follows that the symmetries in Eq. (3.1) dictate the β

phase Hamiltonian to be

$$
\begin{aligned}
H^{\beta} = & H^{L} + 2(d_c + m_c\sigma_z)\cos q_3 + 2(t_c\sigma_x s_y + t''_c\sigma_y)\sin q_3, \\
H^{L} = & M\sigma_z + (t_a\sigma_y + t''_a\sigma_x s_y)(\sin q_1 + \sin q_2) \\
& + D + (t_b\sigma_x s_z + t''_b\sigma_x s_x)\sin(q_2 - q_1), \\
M = & m_0 + m_a(\cos q_1 + \cos q_2) + m_b\cos(q_2 - q_1), \\
D = & d_0 + d_a(\cos q_1 + \cos q_2) + d_b\cos(q_2 - q_1),
\end{aligned}
\tag{3.2}
$$

where H^L is the (001) monolayer Hamiltonian, $q_i = \boldsymbol{k}\cdot\boldsymbol{a}_i$, and $\boldsymbol{a}_{1,2} = (\boldsymbol{a} \mp \boldsymbol{b})/2$ and $\boldsymbol{a}_3 = \boldsymbol{c}$ are the primitive lattice vectors shown in Fig. 3.1.

For simplicity, we set $t''_a = t''_b = t''_c = 0$ in Eq. (3.2) hereafter. We may interpret $t_i \gg t''_i$ ($i = a, b, c$) as follows. As the $|\sigma_z = \pm\rangle$ states are mainly from the p_x orbitals, spin independent hopping processes dominate in the $\boldsymbol{a}$ direction, i.e., $t_a \gg t''_a$. As the contribution of p_z orbitals is negligibly weak at the Fermi energy, the SOC terms $\propto s_z$ dominate those $\propto s_{x,y}$, i.e., $t_b \gg t''_b$. Near the L and M points in Fig. 3.2(a), the bands in the absence of the SOCs become much steeper when the SOC effect is taken into account, i.e., $t_c \gg t''_c$.

To derive the α phase models, we apply zone folding to Eq. (3.2) by doubling the unit cell in the $\boldsymbol{c}$ direction. This model with two (001) layers per unit cell reads

$$
\begin{aligned}
\bar{H}^{\beta} = H^{L} + 2(d_c + m_c\sigma_z)\tau_x \cos\frac{q_3}{2} \\
+ 2t_c\sigma_x s_y \tau_x \sin\frac{q_3}{2},
\end{aligned}
\tag{3.3}
$$

where $\tau_z = \pm$ denote the even and odd (001) layers. Note that in this model the inversion operator becomes $\mathcal{P} = \sigma_z\tau_x$ for inversion center placed in the middle of two adjacent layers and remains $\mathcal{P} = \sigma_z$ for inversion center placed in a layer. In order to make this model periodic in q_3, we further perform the gauge transformation:

$$
\tilde{H}^{\beta} = U\bar{H}^{\beta}U^{-1}, \tag{3.4}
$$

where $U = (1 + \tau_z)/2 + e^{iq_3/2}(1 - \tau_z)/2$, and $\tau_z = \pm 1$ denote the two layers in a unit cell. Then we obtain

$$
\begin{aligned}
\tilde{H}^{\beta} = H^{L} + (d_c + m_c\sigma_z)[\tau_x + (\tau_x \cos q_3 + \tau_y \sin q_3)] \\
+ t_c\sigma_x s_y[\tau_y - (\tau_y \cos q_3 - \tau_x \sin q_3)],
\end{aligned}
\tag{3.5}
$$

in which the inversion operator remains $\mathcal{P} = \sigma_z\tau_x$ for inversion center placed in the middle of two adjacent layers and becomes $\mathcal{P} = \sigma_z(1+\tau_z)/2 + e^{iq_3}\sigma_z(1 - \tau_z)/2$ for inversion center placed in a layer. Note that $\boldsymbol{a}_3 = 2\boldsymbol{c}$ in both Eqs. (3.3) and (3.5).

For the models in Eqs. (3.2)-(3.5) to describe the WTI with band inversions at the M and L points, $(\pi, \pi, 0)$ and (π, π, π), $M_{\pi,\pi} < -2|m_c|$

and $M_{0,0}$, $M_{\pi,0} > 2|m_c|$ are dictated based on the Fu-Kane criterion [15]. The models for α-Bi_4Br_4 and α-Bi_4I_4 are derived below by introducing additional symmetry-allowed terms to the zone-folded β phase model. From the bulk perspective, these terms may seem secondary, as they simply shift the energies of bands and remove the accidental degeneracies of the zone-folded β phase model; when their energy scale is smaller than the gap along the ML line $\sim |M_{\pi,\pi} \pm 2m_c|$, the two α phase models are equivalent to the zone-folded β phase model, as shown in Sec. 3.5.2. More substantially, these terms reduce the translational and inversion symmetries by choosing a location for the inversion center. From the surface perspective, these terms are essential. They open the side surface band gaps in Sec. 3.7.2, yield the surface SSH models in Sec. 3.7.1, and validate the surface topological invariants in Sec. 3.7.3.

3.4.2 α-Bi_4Br_4 model

In contrast to the β phase, the primitive unit cell of α-Bi_4Br_4 consists of two (001) layers, and its inversion center can only be placed in a layer. Thus, Eq. (3.3) provides a reasonable, convenient starting point to construct the effective tight-binding model for α-Bi_4Br_4. Moreover, the even and odd (001) layers are nearly (001) mirror images of each other. Given $s_z H^L s_z = H^L$, the crystal symmetries, and the orbital characters, with the zeroth order corrections, α-Bi$_4$Br$_4$ can be described by

$$\begin{aligned}\bar{H}^{\alpha}_{\mathrm{BiBr}} &= \bar{H}^{\beta} + (d'_0 + m'_0\sigma_z)\tau_z + 2t'_c\sigma_y s_y \tau_y \sin\frac{q_3}{2} \\ &\quad + 2(d'_c + m'_c\sigma_z)s_y\tau_y\cos\frac{q_3}{2},\end{aligned} \tag{3.6}$$

for which $\mathcal{P} = \sigma_z$. In Eq. (3.6) the terms $\propto \tau_z$ characterize the differences between the even and odd layers, and the terms $\propto \tau_y$ are new SOCs. To make this model periodic in q_3, we further perform the same gauge transformation U used in Eq. (3.4) and obtain

$$\begin{aligned}H^{\alpha}_{\mathrm{BiBr}} = &\tilde{H}^{\beta} + (d'_0 + m'_0\sigma_z)\tau_z \\ &+ t'_c\sigma_y s_y[-\tau_x + (\tau_x\cos q_3 + \tau_y \sin q_3)] \\ &+ (d'_c + m'_c\sigma_z)s_y[\tau_y + (\tau_y\cos q_3 - \tau_x\sin q_3)],\end{aligned} \tag{3.7}$$

for which $\mathcal{P} = \sigma_z(1+\tau_z)/2 + e^{iq_3}\sigma_z(1-\tau_z)/2$.

3.4.3 α-Bi$_4$I$_4$ model

Although the primitive unit cell of α-Bi$_4$I$_4$ also consists of two (001) layers, different from α-Bi$_4$Br$_4$, its inversion center can only be placed in the middle of two adjacent layers. For this reason, while the even and odd layers are related to each other, the inter-layer spacings become not uniform any more. In this case, the inter-layer couplings become alternating in α-Bi$_4$I$_4$, and Eq. (3.5) is a more convenient starting point to construct its effective tight-binding model. Considering the alternating couplings, we find that α-

Bi_4I_4 can be described by

$$\begin{aligned} H^{\alpha}_{\mathrm{BiI}} = H^{L} &+ t\sigma_x\tau_z + t'\sigma_y s_y\tau_z + [(d_c + m_c\sigma_z)\tau_x \\ &+ (d'_c + m'_c\sigma_z)(\tau_x \cos q_3 + \tau_y \sin q_3)] \\ &+ \sigma_x s_y[t_c\tau_y - t'_c(\tau_y \cos q_3 - \tau_x \sin q_3)], \end{aligned} \tag{3.8}$$

for which $\mathcal{P} = \sigma_z\tau_x$. In Eq. (3.8), the terms $\propto \tau_z$ are extra symmetry-allowed zeroth order corrections and characterize the differences between the even and odd layers. Note that Eq. (3.8) does not count the relative shifts between adjacent layers within the $\boldsymbol{a}$-$\boldsymbol{b}$ plane. Appendix A.3 provides a more accurate model that takes into account this ignored effect. In fact, the more accurate model reduces to Eq. (3.8) near the ML line.

3.5 Bulk band topology analysis

Recent studies [29–31] on the high-throughput screening of nonmagnetic topological materials (based on topological quantum chemistry [28] or symmetry-based indicators [26, 27, 40, 76]) showed that α-Bi_4Br_4 is a HOTI and α-Bi_4I_4 is a trivial insulator (later we will show that it is actually topological). However, all the previous studies only provided numerical calculation results obtained from a large DFT data without detailed analysis of the band structures of α-Bi_4X_4. In this section, we show that our simple model Hamiltonians derived in Sec. 3.4 successfully reproduce not only the low-energy band structures but also the bulk band topology. Moreover, we find that the non-trivial (trivial) $\mathbb{Z}_4$ inversion symmetry indicator of α-$\mathrm{Bi}_4\mathrm{Br}_4$ (α-$\mathrm{Bi}_4\mathrm{I}_4$) can be obtained simply by the unit cell doubling in the real space or the zone-folding in the reciprocal space to β-$\mathrm{Bi}_4\mathrm{X}_4$. From this, we show that previously overlooked locations of inversion centers are very crucial in the determination of the non-trivial higher-order topology.

3.5.1 Symmetry indicators of $\mathrm{Bi}_4\mathrm{X}_4$

Informed by the band inversions in Fig. 3.2, we can obtain the symmetry indicators [27, 77] of the space group $C2/m$ (No. 12). The space group $C2/m$ is classified as a $P\bar{1}$-type space group in Ref. [77] and thus the symmetry indicators are given by $(\mathbb{Z}_2, \mathbb{Z}_2, \mathbb{Z}_2; \mathbb{Z}_4)$, where first three $\mathbb{Z}_2$ indices are the Fu-Kane weak indices [15], and the $\mathbb{Z}_4$ index is the total number of band inversions modulo 4 [27, 77]. From the DFT calculation, we find $(001; 2)$ for β-$\mathrm{Bi}_4\mathrm{Br}_4$, $(110; 1)$ for β-$\mathrm{Bi}_4\mathrm{I}_4$, and $(000; 2)$ for α-$\mathrm{Bi}_4\mathrm{Br}_4$ with their inversion centers placed in (001) monolayers and $(000; 0)$ for α-$\mathrm{Bi}_4\mathrm{I}_4$ with its inversion center placed in the middle of two adjacent (001) layers. β-$\mathrm{Bi}_4\mathrm{Br}_4$ is a prototype WTI that can be viewed as a periodic stack of 2D $\mathbb{Z}_2$ TIs with one TI layer per unit cell. While our calculation predicts β-$\mathrm{Bi}_4\mathrm{I}_4$ to be a STI, two recent ARPES experiments obtained contrasting conclusions: STI versus WTI [84, 95]. In fact, a small strain can tune β-$\mathrm{Bi}_4\mathrm{I}_4$ to a WTI [83], and the (001) monolayer of β-$\mathrm{Bi}_4\mathrm{I}_4$ is indeed a 2D $\mathbb{Z}_2$ TI as shown in Fig. 3.2. For the purpose of understanding the two α phases, we view the two β phases as the WTI with interlayer couplings much smaller than band gaps. Notably, in the same classification based on the symmetry indicators, while α-Bi$_4$Br$_4$ is a HOTI with $\mathbb{Z}_4 = 2$, α-Bi$_4$I$_4$ is topologically trivial in all possible classes. However, α-Bi$_4$I$_4$ is also a true HOTI as clearly evidenced in Fig. 3.8.

3.5.2 Unit cell doubling of β-Bi$_4$X$_4$

Now we show that the band inversions and symmetry indicators of the two α phases can be directly understood by applying zone folding to the β phase WTI yet choosing two different locations for their inversion centers.

Doubling the unit cell in the $\boldsymbol{c}$ axis folds the TRI momenta with $q_3 = \pi$ back to those with $q_3 = 0$. This implies that, due to the zone folding, all the band inversions in the $q_3 = \pi$ plane move to the corresponding TRI momenta in the $q_3 = 0$ plane. Moreover, at the new TRI momenta in the reduced Brillouin zone (BZ) with $q_3' = \pi$, the inversion eigenstates are symmetric and antisymmetric combinations of the band states at $q_3 = \pm\pi/2$ in the original BZ, i.e., $|q_3' = \pi, \pm\rangle = \left(|q_3 = \pi/2\rangle \pm |q_3 = -\pi/2\rangle\right)/\sqrt{2}$, where $\mathcal{P}\,|q_3 = \pm\pi/2\rangle = |q_3 = \mp\pi/2\rangle$ and q_1, $q_2 = 0$ or π implicitly. Consequently, the band states at the TRI momenta with $q_3' = \pi$ are four-fold degenerate, and for each degeneracy the two Kramers pairs have opposite inversion eigenvalues. This implies that the TRI momenta with $q_3' = \pi$ are irrelevant to the $\mathbb{Z}_2$ and $\mathbb{Z}_4$ indices.

When the inversion center is placed in a (001) monolayer, Fig. 3.5(a) sketches the two band inversions of the β phase WTI at $(\pi, \pi, 0)$ and (π, π, π) in the original BZ. This implies the symmetry indicators $(001; 2)$. For the

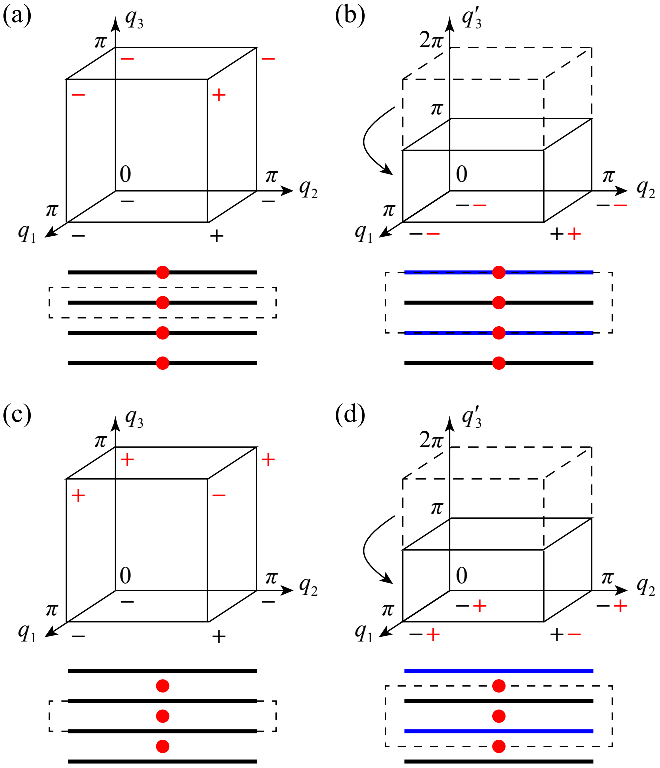

Figure 3.5: The inversion eigenvalues of the occupied bands at the TRI momenta for the β phase WTI, modeled by Eqs. (3.2) and (3.5). Different inversion centers and primitive unit cells are chosen in (a) and (c). Illustrating the band inversions in α-Bi$_4$Br$_4$ and α-Bi$_4$I$_4$, respectively, (b) and (d) are the doubled unit cell counterparts of (a) and (c). In the bottom panels, the solid lines, dashed boxes, and red dots denote the (001) layers, unit cells, and inversion centers, respectively.

same choice of inversion center, the two band inversions appear at $(\pi,\pi,0)$ in the reduced BZ as sketched in Fig. 3.5(b), and the symmetry indicators become $(000;2)$, which also characterizes α-Bi$_4$Br$_4$. When the inversion center is shifted to the middle of two adjacent (001) layers, the inversion operator acquires a factor e^{-iq_3}, and the inversion eigenvalues switch signs at the TRI momenta with $q_3 = \pi$. In this choice of inversion center, in addition to the band inversion at $(\pi, \pi, 0)$, there are three band inversions at $(0, 0, \pi)$, $(0, \pi, \pi)$, and $(\pi, 0, \pi)$, as sketched in Fig. 3.5(c). This implies the symmetry indicators $(001; 0)$. In the reduced BZ as sketched in Fig. 3.5(d), there is one band inversion at each TRI momentum in the $q_3 = 0$ plane, and the symmetry indicators become $(000; 0)$, which also characterizes α-Bi$_4$I$_4$.

Clearly, while the $\mathbb{Z}_2$ indices are not robust against the unit cell doubling, they remain the same under the inversion center shifting. By contrast, the $\mathbb{Z}_4$ index behaves in the opposite manner. Both Figs. 3.5(a) and 3.5(c) illustrate the band inversions of the β phase WTI, since its inversion center can be placed either in a (001) layer or between two adjacent layers. Moreover, Figs. 3.5(b) and 3.5(d) illustrate the band inversions of α-Bi$_4$Br$_4$ and α-Bi$_4$I$_4$, respectively, since the additional inter-layer couplings induced by the structure transitions are sufficiently weak compared with the bulk band gap of the β phase WTI. In fact, those weak couplings play two roles in determining the symmetry and topology of the two α phases. First, they reduce the translational symmetry, opening the side surface band gaps. Second, they reduce the inversion symmetry, fixing the inversion center locations. These two effects lead to $\mathbb{Z}_4 = 2$ for α-Bi$_4$Br$_4$ and $\mathbb{Z}_4 = 0$ for α-Bi$_4$I$_4$. More fundamentally, they together give rise to the surface SSH models in Sec. 3.7.1 and the surface topological invariants in Sec. 3.7.3

3.6 Topological boundary states of α-Bi$_4$X$_4$

In this section, we present the most intriguing features of α-Bi$_4$Br$_4$ and α-Bi$_4$I$_4$, i.e., the emergence of helical hinge states and their dependence on the (001) termination. In order to display the hinge states, We construct finite-size systems of the two materials by using the 3D *ab initio* tight-binding models obtained from the MLWF for the p orbitals of Bi and Br/I. (The computational methods are detailed in Sec. 3.3.)

As we have shown from the 3D bulk band structure analysis, the helical hinge states are expected in α-Bi$_4$Br$_4$ as long as inversion symmetry is protected. However, here we directly demonstrate that α-Bi$_4$Br$_4$ has stable helical hinge states in the even-layer systems where inversion symmetry is broken. More strikingly, we show that not only α-Bi$_4$Br$_4$ but also α-Bi$_4$I$_4$ also can exhibit stable helical hinge states, which is not expected from the bulk band structure analysis as $\mathbb{Z}_4 = 0$ in α-Bi$_4$I$_4$. The existence of the interesting termination-dependent hinge state patterns tells us that the 3D bulk band topology analysis is not enough for the complete understanding of the topological nature of α-Bi$_4$X$_4$.

3.6.1 Helical hinge and gapless surface states of α-Bi$_4$Br$_4$

α-Bi$_4$Br$_4$ has two (001) layers in a primitive unit cell and each (001) monolayer is a 2D $\mathbb{Z}_2$ TI (The crystal structure of α-Bi$_4$Br$_4$ is detailed in Sec. 3.2.). For convenience, we label the two layers as A and B. The inver-

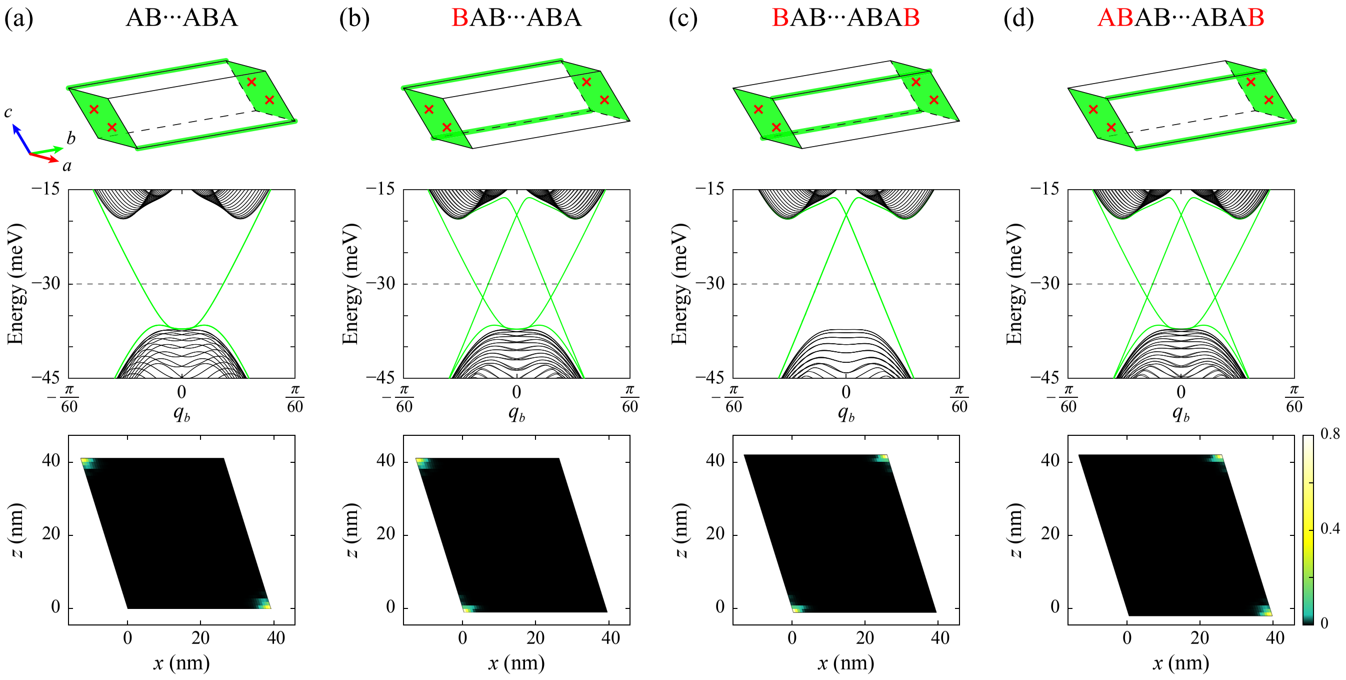

Figure 3.6: The helical hinge states of α-Bi$_4$Br$_4$ under four different scenarios of (001) surface terminations. (a)-(d) The label on the top of each column indicates the layer stacking order of the considered system in the $\boldsymbol{c}$ axis, and the red letters denote the extra (001) layer(s) compared with the case in (a). Upper panels: schematics of the helical hinge states in the $\boldsymbol{b}$ (chain) direction and the Dirac surface states at the (010) and $(0\bar{1}0)$ surfaces. The green regions are the gapless boundaries, and each red cross denotes a surface Dirac cone. Middle panels: calculated band structures by using the MLWF. All the four systems are of finite size in the $\boldsymbol{a}$ and $\boldsymbol{c}$ directions and periodic in the $\boldsymbol{b}$ direction. The zero energy is set at the 0 meV in Fig. 3.2(b). The green lines are the helical hinge states, and the black lines are the gapped surface states. Because of the unbroken inversion symmetry in odd-layer systems, all the bands are doubly degenerate in (a) and (c). Lower panels: calculated spatial densities for the helical hinge states at the energy indicated by the dashed lines in the middle panels.

sion center of α-Bi$_4$Br$_4$ is in a monolayer and thus the A-type and B-type layers are reflected to themselves under inversion, respectively. It follows that there are four possible scenarios of (001) termination, i.e., A-A, B-A, B-B, and A-B, and that they feature distinct patterns of helical hinge states, as depicted in the upper panels of Fig. 3.6.

In Fig. 3.6(a), the featured system is periodic in the $\boldsymbol{b}$ direction, 60-unit-cell long in the $\boldsymbol{a}$ direction, and 43-layer thick in the $\boldsymbol{c}$ direction with the A-A termination. Because the system has an odd number of (001) layers, from the perspective of 2D $\mathbb{Z}_2$ TI, there must be one pair of helical edge states in total in the $\boldsymbol{b}$ direction. Given the unbroken inversion symmetry, the pair must be degenerate in energy and localized in two hinges that are reflected to each other under inversion. The spectroscopic and spatial patterns of the pair of helical hinge states, calculated based on the MLWF, are presented in the middle and lower panels of Fig. 3.6(a).

The system in Fig. 3.6(b) has one extra (001) layer stacked to the bottom of the system in Fig. 3.6(a). As a result, one helical edge state of the extra TI layer annihilates the bottom hinge state in Fig. 3.6(a), whereas the other creates a new hinge state at the opposite side of the bottom in Fig. 3.6(b). As the inversion symmetry is broken in this even-layer system, the pair of hinge states are not related under inversion. In Fig. 3.6(c), one extra (001) layer is stacked to the top of the system in Fig. 3.6(b). In a similar fashion, the top hinge state in Fig. 3.6(b) is annihilated whereas a new hinge state emerges at the opposite side of the top in Fig. 3.6(c). Since the inversion symmetry is restored in this odd-layer system, the new pair of hinge states become symmetric and degenerate. In Fig. 3.6(d), the bottom of the system has one extra (001) layer compared to that in Fig. 3.6(c). As expected, this extra TI layer breaks the inversion symmetry and switches the bottom hinge state to the opposite side.

We note that, because of the $\mathbb{Z}_2$ character of 2D TI, the hinge states are gapped for the two even-layer scenarios yet remain gapless for the two odd-layer scenarios in the atomically thin limit. In the bulk limit, however, in each scenario the pair of hinge states are separate in space and gapless in energy. While the scenarios in Figs. 3.6(a) and 3.6(c) are the inversion symmetric time-reversal-invariant (TRI) TIs, which is consistent with the bulk analysis in Sec. 3.5 with the non-trivial symmetry indicator $\mathbb{Z}_4 = 2$, here we demonstrate explicitly in Figs. 3.6(b) and 3.6(d) that the existence of helical hinge states does not require the inversion symmetry. In fact, the hinge states in Figs. 3.6(a) and 3.6(c) are robust against inversion symmetry breaking, as long as the disturbance neither close the surface band gaps nor hybridize the helical states at different hinges (or edges). Indeed, following the ZKM theory [33], the hinge states of α-Bi$_4$Br$_4$ can also be demonstrated by applying a surface topological invariant or a surface domain-wall argument to the effective tight-binding models we derived in Sec. 3.4. The two demonstrations are provided in Sec. 3.7.

Evidently in Fig. 3.6, depending on its (001) termination, each scenario exhibits a distinct pattern of helical hinge states. In fact, the four scenarios in Fig. 3.6 are the elementary building blocks of α-Bi$_4$Br$_4$, and any many-layer system even with stacking faults or/and step edges can be decomposed

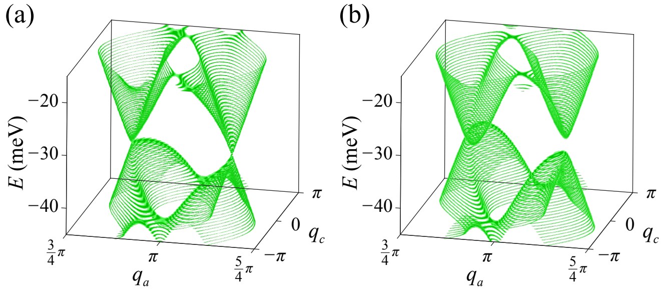

Figure 3.7: (a) Gapless (010) surface states of pristine α-Bi$_4$Br$_4$ and (b) gapped (010) surface states of α-Bi$_4$Br$_4$ with a C_2-asymmetric TRI surface potential. The constant-energy contours with a spacing of 0.5 meV are obtained by the surface Green's function calculations of the MLWF for a semi-infinite system. The zero energy is set at the 0 meV in Fig. 3.2(b).

into them. For instance, stacking Fig. 3.6(c) on top of Fig. 3.6(a) produces a scenario represented by Fig. 3.6(d). This fact can be verified easily by superimposing the two schematics in the upper panels or the two band structures in the middle panels. Intriguingly, stacking Fig. 3.6(c) on top of Fig. 3.6(d) yields one layer of stacking fault: effectively, one 2D TI layer is embedded into the interior of Fig. 3.6(d).

For completeness, we close this section by showing that α-Bi$_4$Br$_4$ also hosts protected surface states at the (010) and (0$\bar{1}$0) surfaces. The gapless surface Dirac cones are denoted as the red crosses in Fig. 3.6. Based on the surface Green's function calculations of the MLWF for a semi-infinite system, Fig. 3.7(a) features the two (010) surface Dirac cones of α-Bi$_4$Br$_4$, which are protected and related by the $\mathcal{C}_2$ symmetry. By contrast, a similar calculation for α-Bi$_4$I$_4$ reveals no gapless surface states, although it also has the $\mathcal{C}_2$ symmetry. Nevertheless, we confirm the previous finding [31, 81] of

α-Bi$_4$Br$_4$ being a rare topological crystalline insulator with a surface rotation anomaly [104] by the first-principles calculations as detailed in Sec. 3.3. One can further verify this result directly by evaluating a rotation invariant [104] or indirectly by using the symmetry indicators [31, 81] along with the inversion eigenvalues listed in Sec. 3.5.1.

Moreover, when the effects such as dangling bonds and surface reconstruction are ignored, the two surface Dirac points are identified at $(q_a, q_c) = \pm(0.861, 0.113)\pi$. When a TRI (010) surface potential that breaks the $\mathcal{C}_2$ symmetry is added in our calculation, the gapless Dirac cones in Fig. 3.7(a) become gapped, as shown in Fig. 3.7(b). This unambiguously demonstrates that it is the $\mathcal{C}_2$ symmetry that protects the (010) surface Dirac cones. We point out that it would be challenging to observe the gapless (010) surface states in experiment, because the (010) surface is not a natural cleavage plane, and because α-Bi$_4$Br$_4$ is extremely soft[3]. Most likely, the $\mathcal{C}_2$ symmetry would be broken by the (010) dangling bonds and surface reconstruction. Fortunately, the hinges states of our major interest are between two natural cleavage planes. This facilitates the future hinge state experiments.

3.6.2 Helical hinge states of α-Bi$_4$I$_4$

α-Bi$_4$I$_4$ is similar to α-Bi$_4$Br$_4$ in two aspects. First, the primitive unit cell of α-Bi$_4$I$_4$ also consists of two (001) layers, which we also label them as A and B. Thus, there are four possible scenarios of (001) termination, i.e., A-B, B-B, B-A, and A-A. Any many-layer system even with stacking faults or/and step edges can be decomposed into them. Second, each (001) monolayer of α-$\mathrm{Bi_4I_4}$ is also a 2D $\mathbb{Z}_2$ TI with a crystal structure similar to that of α-$\mathrm{Bi_4Br_4}$ as detailed in Sec. 3.2.

---

[3] Bing Lv (private communication).

However, in contrast to α-$\mathrm{Bi_4Br_4}$, the inversion center of α-$\mathrm{Bi_4I_4}$ is in the middle of two adjacent (001) layers. Since each of the A- and B-type layers is inversion-asymmetric and reflected to the other type under inversion, only even-layer systems are inversion symmetric. Significantly, although α-$\mathrm{Bi_4I_4}$ has $\mathbb{Z}_4 = 0$ as an inversion symmetric TRI insulator and trivial symmetry indicators in general [29–31], we explicitly show in Fig. 3.8 that it can host helical hinge states for three of its four possible (001) terminations.

In Fig. 3.8(a), the featured system is periodic in the $\boldsymbol{b}$ direction, 60-unit-cell long in the $\boldsymbol{a}$ direction, and 44-layer thick in the $2\boldsymbol{c} - \boldsymbol{a}$ direction with the A-B termination. The spectroscopic and spatial patterns of this system, calculated based on the MLWF, are presented in the middle and lower panels of Fig. 3.8(a). Clearly, this system of A-B termination does not host any gapless boundary state. This result is consistent with the fact that the system in Fig. 3.8(a) has an even number of 2D $\mathbb{Z}_2$ TIs from the 2D perspective and the fact that α-$\mathrm{Bi_4I_4}$ has trivial symmetry indicators from the 3D perspective [29–31]. The system of B-B termination in Fig. 3.8(b) has one extra (001) layer stacked to the bottom of the system in Fig. 3.8(a). The new system can be viewed as a 2D $\mathbb{Z}_2$ TI since it consists of an odd number of (001) layers. As a result, a pair of helical hinge states in the $\boldsymbol{b}$ direction emerges at the opposite sides of the bottom in Fig. 3.8(b). For the B-A termi-

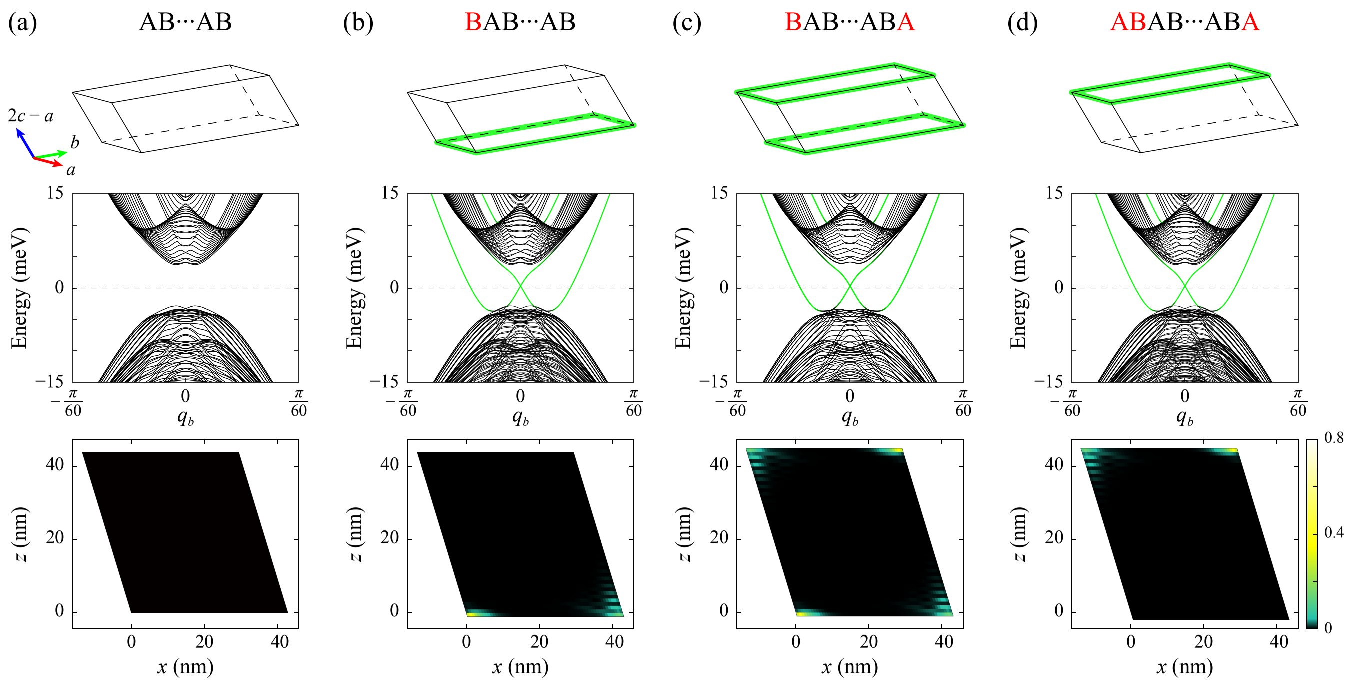

Figure 3.8: The helical hinge states of α-Bi$_4$I$_4$ under four different scenarios of (001) surface terminations. (a)-(d) The label on the top of each column indicates the layer stacking order of the considered system in the $2\boldsymbol{c} - \boldsymbol{a}$ axis, and the red letters denote the extra (001) layer(s) compared with the case in (a). Upper panels: schematics of the helical hinge states in the $\boldsymbol{b}$ (chain) direction. The green regions are the gapless boundaries. Middle panels: calculated band structures by using the MLWF. All the four systems are of finite size in the $\boldsymbol{a}$ and $2\boldsymbol{c} - \boldsymbol{a}$ directions and periodic in the $\boldsymbol{b}$ direction. The zero energy is set at the 0 meV in Fig. 3.2(c). The green lines are the helical hinge states, and the black lines are the gapped surface and bulk states. Because of the unbroken inversion symmetry in even-layer systems, all the bands are doubly degenerate in (a) and (c). Lower panels: calculated spatial densities for the helical hinge states at the energy indicated by the dashed lines in the middle panels.

nation in Fig. 3.8(c), one extra (001) layer is stacked to the top of the system in Fig. 3.8(b). In a similar fashion, a pair of helical hinge states emerges at the opposite sides of the top in Fig. 3.8(c), in addition to the pair at the bottom. This even-layer system is trivial from the perspectives of 2D $\mathbb{Z}_2$ TI and 3D symmetry indictors, yet it hosts helical hinge states at all the four hinges in the $\boldsymbol{b}$ direction. For the A-A termination in Fig. 3.8(d), the bottom of the system has one extra (001) layer compared to that in Fig. 3.8(c). As expected, the edge states of the extra TI layer annihilate the bottom hinge states in Fig. 3.8(c).

We note that the two odd-layer scenarios in Figs. 3.8(b) and 3.8(d) have neither the inversion symmetry nor the C_2 symmetry of the bulk as detailed in Sec. 3.2. In each scenario the pair of hinge states is not related by any symmetry. Intriguingly, the two scenario can be related under inversion, and thus all the features in Figs. 3.8(b) and 3.8(d) are the same, except that their hinge states are localized at the opposite hinges. Nevertheless, the three patterns of hinge states in Fig. 3.8 are all robust against inversion symmetry breaking, as long as the disturbance neither close the surface band gaps nor hybridize the helical states at different hinges (or edges). We stress that, whereas the hinge states of α-$\mathrm{Bi_4I_4}$ cannot be understood by the bulk symmetry indicators, they can be captured within the ZKM theory [33] by applying a surface topological invariant or a surface domain-wall argument to the effective tight-binding model, as shown in Sec. 3.7.

3.7 Band topology of α-Bi$_4$X$_4$ with open boundaries

The key features of α-Bi$_4$Br$_4$ and α-Bi$_4$I$_4$ presented in Figs. 3.6 and 3.8 are all calculated by using the DFT-based MLWF. In Secs. 3.6.1 and 3.6.2 we also deduce all these features based on the minimal numerical results, i.e., one of the four scenarios, and the knowledge of 2D $\mathbb{Z}_2$ TI. To further explain these appealing features, now we provide a computation-free surface argument based on the locations of inversion centers and the knowledge of 2D $\mathbb{Z}_2$ TI. (A similar argument also exists by considering the locations of twofold rotation axes.) Because each (001) monolayer is a 2D $\mathbb{Z}_2$ TI, the (100) side surface of β-Bi$_4$X$_4$ or α-Bi$_4$Br$_4$ can be viewed as a "chain" (in the $\boldsymbol{c}$ direction) of coupled helical edge states (in the $\boldsymbol{b}$ direction), and likewise the ($\bar{1}$00) side surface. This fact also applies to the (201) and $(\bar{2}0\bar{1})$ side surfaces of α-Bi$_4$I$_4$. (The subtle differences between the crystal structures of the two α phases are detailed in Sec. 3.2). This argument is analogous to the Su-Schrieffer-Heeger (SSH) model [92], and it is valid because the nearest-neighbor (NN) inter-layer edge tunnelings are much smaller than the bulk band gaps.

In this section, first we briefly explain how the SSH models are formed at the surfaces of Bi$_4$X$_4$ only from the symmetry analysis without explicit calculations and show that the termination-dependent hinge states can be easily understood from the SSH argument in Sec. 3.7.1. From the observation that the surface dimerization pattern plays a crucial role in the formation of helical hinge states in α-Bi$_4$X$_4$, we derive the side surface Hamiltonians and explicitly show the analogy with the SSH model in Sec. 3.7.2. Using the analogy with the SSH model, we derive the surface topological invariants, which can be used to characterize the topological properties of α-Bi$_4$X$_4$ under the open boundary conditions in Sec. 3.7.3. Then we comment on α-Bi$_4$I$_4$ as a recently proposed boundary-obstructed TI in Sec. 3.7.4. Lastly in Sec. 3.7.5, we introduce an alternative approach to understand the helical hinge state patterns in α-Bi$_4$X$_4$, the domain wall argument in the ZKM theory [33, 47].

3.7.1 Coupled edge construction

Consider first the WTI β-Bi$_4$X$_4$ [83, 84] depicted in Fig. 3.9(b). The primitive unit cell of β-Bi$_4$X$_4$ consists of only one (001) layer. The inversion center can be placed in a monolayer or in the middle of a bilayer. As a result, the inversion symmetry restricts the NN inter-edge tunnelings to be the same between any two adjacent edges at any side surface. Given that the tunnelings are weak, each side surface states can be viewed as a 1D Dirac cone along k_b dispersing weakly along k_c; the Dirac cone is gapless only at the TRI points $k_c = 0$ and π. This is exactly what has been predicted in a previous theory [83] and observed in a recent experiment [84]. Therefore, both the (100) and ($\bar{1}$00) side surfaces are gapless, independent of the number of (001) layers, as sketched in Fig. 3.9(d). This is analogous to the critical point of the SSH model. Remarkably, the β phase (an equally spaced chain of edge states) does undergo a Peierls transition (i.e., dimerization) to an α phase (dimerized chain of edge states) at low temperature [83]. The critical temperature of Bi_4I_4 turns out to be room temperature [82, 84, 89–91]. There may exist an edge-state Peierls' theorem to explain the instability.

In the case of α-Bi_4Br_4, the inversion center can only be placed in a (001) layer. Consequently, as depicted in Fig. 3.9(a), the inversion symmetry only relates the NN upper A-lower B tunneling at one side surface to the NN lower A-upper B tunneling at the other side surface, and the NN upper A-lower B and lower A-upper B tunnelings at the same side surface generally have different strengths. This gives rise to the unique dimerization pattern in Fig. 3.9(a): the two side surfaces exhibit opposite dimerizations. Following the spirit of SSH model, the dimerizations gap the strongly coupled edge states, and any weakly coupled one left by a (001) surface termination yields a helical hinge state. As showcased in Fig. 3.9(d), there are four possible terminations, and each has a distinct pattern of hinge states. This explains the four scenarios of hinge states featured in Fig. 3.6.

In the case of α-Bi_4I_4, by contrast, the inversion center can only be placed between two adjacent layers. Accordingly, as depicted in Fig. 3.9(c), the NN upper A-lower B tunnelings at different side surfaces are related by the inversion symmetry, and likewise the NN lower A-upper B tunnelings. Yet, the two tunnelings generally have different strengths. It follows that the two side surfaces exhibit the same dimerization. Moreover, the strongly coupled edge states become gapped, leaving the weakly coupled ones at the hinges gapless. As showcased in Fig. 3.9(d), there are four possible terminations, and three yield distinct hinge states while one is trivial. This explains the four scenarios of hinge states featured in Fig. 3.8.

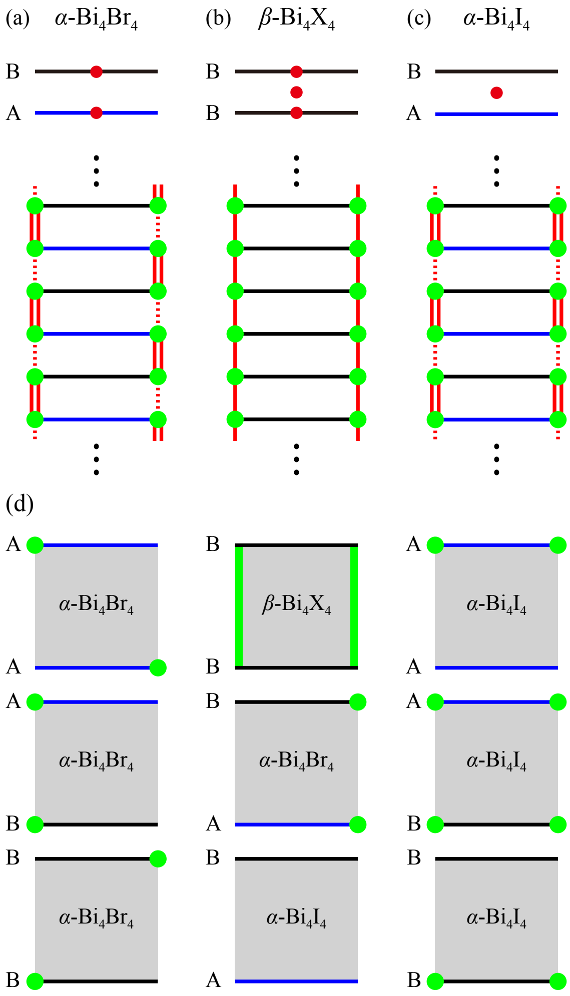
(a) α-Bi4Br4
(b) β-Bi4X4
(c) α-Bi4I4
B
A
B
B
B
A
(d)
A
α-Bi4Br4
A
B
β-Bi4X4
B
A
α-Bi4I4
A
A
α-Bi4Br4
B
B
α-Bi4Br4
A
A
α-Bi4I4
B
B
α-Bi4Br4
B
B
α-Bi4I4
A
B
α-Bi4I4
B

Figure 3.9: (a)-(c) The possible inversion centers (or twofold rotation axes) of Bi_4X_4 and the dimerization patterns of the coupled edge states at the two side surfaces. The black and blue lines denote the B- and A-type (001) layers. The red dots denote the inversion centers (or twofold rotation axes). The green dots denote the helical edge states in the $\boldsymbol{b}$ (chain) direction. The double solid and single dashed red lines denote the stronger and weaker NN inter-edge tunnelings. (d) All possible (001) surface terminations: one for the β phase and four for each α phase. The green lines denote the Dirac surface states, and the green dots denote the helical hinge states.

Clearly, a key difference between the two α phases is whether the two side surfaces exhibit the same or opposite dimerizations. For α-$\mathrm{Bi_4Br_4}$, because of the opposite dimerizations at the two side surfaces, there always exists two unpaired edge states, one at the top and the other at the bottom, independent of the termination. This is rooted in the fact that its inversion center can only be placed in a (001) layer. For α-$\mathrm{Bi_4I_4}$, because of the same dimerization at the two side surfaces, the unpaired edge states always appear in pair at the top or bottom (or both). This originates from the fact that its inversion center can only be placed between two adjacent layers. We point out that compelling evidence of the revealed surface dimerization patterns in the two α phases is provided by their crystal structures in Fig. 3.1 and effective surface models in Eqs. (3.12) and (3.14).

3.7.2 Surface models and the SSH dimerization

Following the ZKM theory [33, 47], we can impose the topological boundary conditions in the (100) and $(\bar{1}00)$ directions and obtain the surface states for the two cases. This allows us to derive the surface SSH models in Fig. 3.9, formulate a surface topological invariant determining the hinge state patterns in Figs. 3.6 and 3.8, and characterize the topological distinctions between the two α phases.

We start from the β phase WTI that has two band inversions, one at M point $(\pi, \pi, 0)$ and one at L point (π, π, π). Near the ML line, Eq. (3.2) yields the following (100) and $(\bar{1}00)$ surface Hamiltonians

$$h^{\beta} = D_{\pi,\pi} + \eta t_b s_z q_b + 2d_c \cos q_3 + 2\eta t_c s_y \sin q_3, \tag{3.9}$$

where $D_{\pi,\pi} = d_0 - 2d_a + d_b$. Note that the (100) and $(\bar{1}00)$ surface states are the eigenstates of σ_x with $\eta = \pm$ eigenvalues, respectively [47]. As a result, those terms anticommuting with σ_x in Eq. (3.2) only produce hybridization between the two surfaces [33], which is negligibly weak when the two surfaces are well separated, and can thus be safely ignored in Eq. (3.9). In fact, the two surface models in Eq. (3.9) can be constructed by directly considering the symmetries in Eq. (3.1) and the orbitals in Fig. 3.3. Each surface model in Eq. (3.9) describes two connected gapless Dirac cones respecting the $\mathcal{M}_b$ symmetry, one at $(0, 0)$ and the other at $(0, \pi)$ with different Dirac-point energies. The two surface models in Eq. (3.9) can be related by the $\mathcal{P}$ or $\mathcal{C}_2$ symmetry.

Similar to Eq. (3.5), we apply zone folding to Eq. (3.9) by doubling the unit cell in the $\boldsymbol{c}$ direction and obtain

$$\begin{aligned}\tilde{h}^{\beta} &= D_{\pi,\pi} + \eta t_b s_z q_b + d_c[\tau_x + (\tau_x \cos q_3 + \tau_y \sin q_3)] \\ &\quad + \eta t_c s_y[\tau_y - (\tau_y \cos q_3 - \tau_x \sin q_3)]. \end{aligned} \tag{3.10}$$

It is clear that the two Dirac surface states in Eq. (3.9) are folded into $(0, 0)$ in Eq. (3.10), and that they remain gapless. Moreover, from the terms $\propto \tau_{x,y}$

in Eq. (3.10), the inter-layer tunneling-up and -down matrices read

$$T^{\beta,\pm} = d_c \mp i\eta s_y t_c, \tag{3.11}$$

which implies no surface dimerization since $|T^{\beta,+}| = |T^{\beta,-}|$. The gapless nature and the absence of dimerization agree well with the edge construction in Sec. 3.7.1 that the WTI side surface models are analogous to the critical point of the SSH model.

In the same fashion, Eqs. (3.7) and (3.8) respectively yield the (100) and $(\bar{1}00)$ surface Hamiltonians of α-Bi$_4$Br$_4$

$$h^{\alpha}_{\mathrm{BiBr}} = \tilde{h}^{\beta} + d'_c s_y[\tau_y + (\tau_y \cos q_3 - \tau_x \sin q_3)] + d'_0 \tau_z, \tag{3.12}$$

with the inter-layer tunneling-up and -down matrices

$$T^{\alpha,\pm}_{\mathrm{BiBr}} = d_c - i s_y (d'_c \pm \eta t_c), \tag{3.13}$$

and the (201) and $(\bar{2}0\bar{1})$ surface Hamiltonians of α-Bi$_4$I$_4$

$$\begin{aligned} h^{\alpha}_{\mathrm{BiI}} = {} & D_{\pi,\pi} + \eta t_b s_z q_b + [d_c \tau_x + d'_c(\tau_x \cos q_3 + \tau_y \sin q_3)] \\ & + \eta s_y [t_c \tau_y - t'_c(\tau_y \cos q_3 - \tau_x \sin q_3)] + \eta t \tau_z, \end{aligned} \tag{3.14}$$

with the inter-layer tunneling-up and -down matrices

$$T^{\alpha,+}_{\mathrm{BiI}} = d_c - i\eta s_y t_c, \quad T^{\alpha,-}_{\mathrm{BiI}} = d'_c + i\eta s_y t'_c. \tag{3.15}$$

Evidently, surface dimerization is present in Eqs. (3.12) and (3.14), as $|T_{\mathrm{BiBr}}^{\alpha,+}| \neq |T_{\mathrm{BiBr}}^{\alpha,-}|$ and $|T_{\mathrm{BiI}}^{\alpha,+}| \neq |T_{\mathrm{BiI}}^{\alpha,-}|$. Similarly in the two cases, the dimerization gaps the two surface states at $(0,0)$ in Eq. (3.10). Differently, the dimerization is characterized by $\eta t_c d_c'$ in Eq. (3.12) and by $|d_c| - |d_c'|$ and $|t_c| - |t_c'|$ in Eq. (3.14); the former only exists at the surfaces, whereas the latter even exists in the bulk. Moreover, for the two spins ($s_y = \pm$) the dimerization patterns are the same in both cases, however, for the two side surfaces ($\eta = \pm$) the dimerization patterns are the same for α-Bi$_4$I$_4$ but opposite for α-Bi$_4$Br$_4$. All these results agree well with the edge construction in Sec. 3.7.1 and the atomic dimerization in Sec. 3.2.4.

3.7.3 Surface topological invariants

From the analysis above, it is clear that a mirror (or s_y-resolved) winding number [105] can be used to characterize the topological properties of the two surface models in Eqs. (3.12) and (3.14). This is allowed because in the $\boldsymbol{c}$ direction these surface models are 1D tight-binding models. Applying the results in Appendix A.4 here and considering the terms $\propto \tau_{x,y}$ at $q_b = 0$ only, we obtain

$$\gamma_{\mathrm{BiBr}}^{\eta,s_y} = \Theta\left(-\eta t_c d_c'\right) \tag{3.16}$$

for the model in Eq. (3.12) and

$$\gamma_{\mathrm{BiI}}^{\eta,s_y} = \Theta\left(\sqrt{{d_c'}^2 + {t_c'}^2} - \sqrt{{d_c}^2 + {t_c}^2}\right) \tag{3.17}$$

for the model in Eq. (3.14), with Θ the Heaviside function.

For both α-Bi_4Br_4 and α-Bi_4I_4, their winding numbers are independent of s_y. This implies that the topological invariants and dimerization patterns are robust against the $\mathcal{M}_b$ symmetry breaking. At the two opposite side surfaces, the winding numbers are different for α-Bi_4Br_4 but the same for α-Bi_4I_4. Both conclusions are consistent with the dimerization analyses in Secs. 3.2.4, 3.7.1, and 3.7.2. Although a winding number is gauge dependent, the differences in winding number between the two opposite side surfaces (of the same α phase) and between the two different α phases are both gauge invariant.

The terms $\propto \tau_z$ in Eqs. (3.12) and (3.14) break the chiral symmetry and seem to make the winding numbers in Eqs. (3.16) and (3.17) meaningless. In general, as the chiral symmetry breaking produces particle-hole asymmetry, a zero-energy bound state implied by a nontrivial winding number is not necessarily pinned to the middle of band gap and can be removed perturbatively. However, this is not the case here. The pairs of zero modes implied by the nontrivial winding numbers become dispersive across the surface band gaps in the presence of the terms $\propto q_b$[4] and form helical hinge states with gapless Dirac points at $q_b = 0$, which is protected by the $\mathcal{T}$ symmetry.

We stress that the validity of the topological invariants in Eqs. (3.16) and (3.17) requires the presence of the $\mathcal{T}$ symmetry and the surface band gaps whereas it does not rely on the presence of the $\mathcal{P}$, $\mathcal{M}_b$, or $\mathcal{C}_2$ symmetry.

---

[4] This is inherited from the monolayer TIs. In other words, terms $\propto$ sin q_b can not ensure the same protection.

3.7.4 Boundary-obstructed phase in α-Bi$_4$I$_4$

The topological phase in α-Bi$_4$I$_4$ is the boundary-obstructed TI (BOTI) proposed very recently [106]. The BOTI is defined by a topological phase which does not have any bulk obstruction but has an obstruction at the boundary. Thus, the BOTI can be deformed into a trivial insulator without closing the bulk gap, but the boundary gap is closed instead.

α-Bi$_4$I$_4$ clearly exhibits such property, which can be easily shown from the model Hamiltonian in Eq. (3.8). Considering the boundary conditions, one finds that the bulk model for the A-B termination of α-Bi$_4$I$_4$ [Fig. 3.8(a)] is related to the model for the B-A termination [Fig. 3.8(c)] by a transformation which shifts the unit cell by $\boldsymbol{c}/2$: $d_c, m_c, t_c \leftrightarrow d'_c, m'_c, t'_c$ and $t, t' \rightarrow -t, -t'$. Since the zone-folding argument discussed in Sec. 3.5.2 agrees with the DFT data, the deviation of α-Bi$_4$I$_4$ from β-Bi$_4$I$_4$ is not large enough to close the bulk gap. Thus, the bulk models for the two terminations of α-Bi$_4$I$_4$ can be smoothly connected to each other without closing the bulk band gap by passing through the model for β-Bi$_4$I$_4$. However, the surface gap is closed along this path because β-Bi$_4$I$_4$ is a WTI. Note that β-Bi$_4$I$_4$ is a topological phase transition point from the viewpoint of the surface invariant in Eq. (3.17), since the model for β-Bi$_4$I$_4$ can be obtained by putting $d_c = d'_c$, $m_c = m'_c$, $t_c = t'_c$ and $t = t' = 0$.

Since a BOTI does not have any bulk obstruction but has a boundary obstruction, the hinge states of a BOTI can be realized by placing 2D TIs in 3D space properly. For example, the boundary states of the B-A termination can be realized in a 3D trivial insulator sandwiched by two 2D TIs. Thus, the BOTI phase may seem equivalent to a set of 2D TIs in 3D space. However, the B-A termination of α-Bi_4I_4 does not require a special setting for the boundary conditions unlike sandwiched 3D trivial insulator, where the couplings between the 3D insulator and the 2D TIs should be negligible in order to localize the edge states at the hinges. Instead, the localization of the hinge states in the B-A termination is guaranteed topologically from the interlayer couplings in the 3D bulk Hamiltonian and the open boundary condition as shown in Eq. (3.17).

3.7.5 Domain wall argument

Although the dimerization analyses and the topological invariants above are sufficient to understand the helical hinge states of the two α phases, here we briefly discuss how to use the ZKM theory [33, 47] to construct domain walls (DW) and deduce the presence or absence of hinge states. This DW method has been employed to obtain the original higher-order chiral TI [33] and to demonstrate several more recent examples [35–37, 39–42, 64, 104, 107].

Consider the local frame of a generic surface formed by a vector $\boldsymbol{j}$ along the hinge, the outward surface normal $\boldsymbol{k}$, and the direction $\boldsymbol{i} = \boldsymbol{j} \times \boldsymbol{k}$ (at the surface). While the $\boldsymbol{j}$ axis is fixed, the $\boldsymbol{k}$ and $\boldsymbol{i}$ axes co-move with the surface. As the bulk translational symmetry is broken in the $\boldsymbol{k}$ direction by a topological boundary condition, we can derive a surface Hamiltonian that

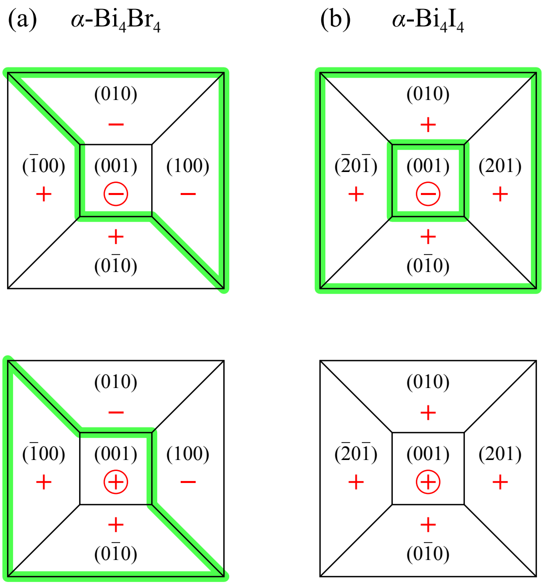

Figure 3.10: Schematics of inversion symmetric (a) α-Bi$_4$Br$_4$ and (b) α-Bi$_4$I$_4$ samples with or without helical hinge states. The relative signs of the mass term gapping the two surface Dirac cones are indicated in red. The hinge states along the domain walls switching the mass signs are indicated in green. (The other two hinge state patterns for α-Bi$_4$Br$_4$ are not shown. The $\mathcal{C}_2$ symmetry is not considered here.)

describes all the surfaces sharing the same hinge in the $\boldsymbol{j}$ direction [47]. For a generic surface, the two resulting surface Dirac cones are gapped due to a hybridization mass.

For α-Bi$_4$Br$_4$, viewed in the local frame, the $\mathcal{P}$ symmetry dictates the mass term to have the opposite signs at two opposite surfaces. This is because the dimerization of α-Bi$_4$Br$_4$ is a surface effect as revealed in Sec. 3.7.2. As a result, depending on the relative sign of the mass term at the top surface, an inversion symmetric sample exhibits one loop of hinge states in one of the two fashions, as depicted in Fig. 3.10(a). (The mass term at the (010) or $(0\bar{1}0)$ surface is odd under the $\mathcal{C}_2$ rotation, restoring the two gapless Dirac cones.) For α-Bi$_4$I$_4$, however, the $\mathcal{P}$ symmetry dictates the mass term to have the same sign at two opposite surfaces. In fact, the mass term has the same sign for all the side surfaces, since the dimerization of α-Bi$_4$I$_4$ is a bulk effect as revealed in Sec. 3.7.2. It follows that, depending on the relative sign of the mass term at the top surface, an inversion symmetric sample hosts either no hinge states or two loops of hinge states, as depicted in Fig. 3.10(b). These are consistent with the results presented in Figs. 3.6(a), 3.6(c), 3.8(a), and 3.8(c).

3.8 Experiments

A variety of experiments can be carried out to examine our predictions. This section introduces three of my collaborations with experimental groups. This section is largely based on Refs. [45, 91, 108].

3.8.1 Room-temperature topological phase transition in Bi$_4$I$_4$

In Ref. [91], we studied the phase transition between α- and β-Bi$_4$I$_4$. We firstly verified the structural transition between the high-temperature β and low-temperature α phases, which can be characterized by the resistance discontinuity and its hysteresis in bulk transport and by the bulk band splitting due to the dimerization, which are shown in Figs. 3.11(a) and 3.11(b)-

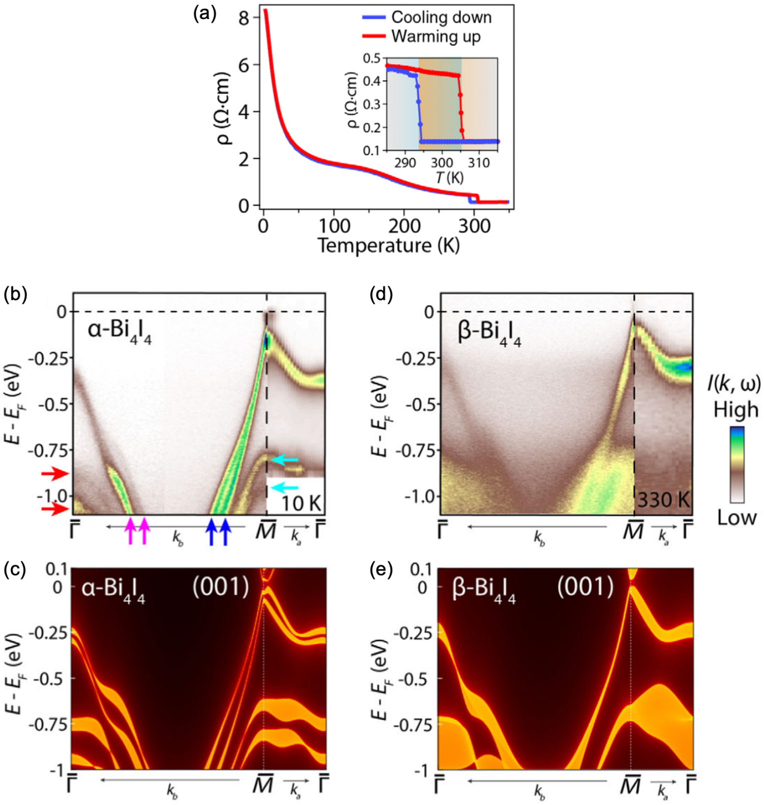

Figure 3.11: (a) Temperature-dependent resistivity data for both cooling and warming curves. The inset is the enlarged view showing the hysteresis behavior of the first-order transition. (b) Measured dispersions in α-Bi$_4$I$_4$ along high symmetry cuts. (c) Calculated bulk band structure of α-Bi$_4$I$_4$ projected onto the (001) surface. (d),(e) Same as (b),(c) but for β-Bi$_4$I$_4$. A clear doubling of the bulk valence bands is evident from β-Bi$_4$I$_4$ to α-Bi$_4$I$_4$ in both the measured and calculated dispersions. All measurement temperatures are as indicated.

(e), respectively.

Having confirmed the phase transition as observed from the electronic structure, we examine the topological proper-ties of the two phases. In Fig. 3.12 we present high-resolution measurements near E_F for both phases. We

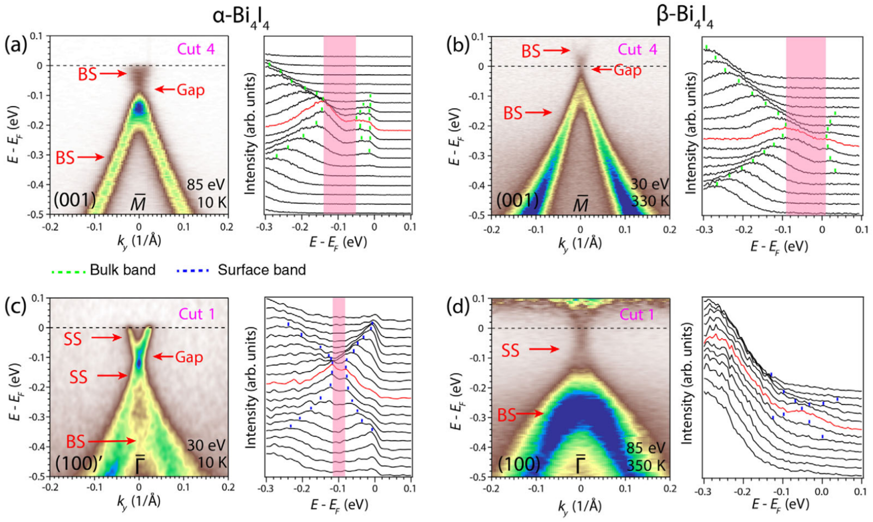

Figure 3.12: Surface states evolution across the phase transition. (a) Band image along the k_b-axis on the (001) surface of α-Bi$_4$I$_4$ as well as its corresponding EDC stacks. The red EDC corresponds to $k_b = 0$. The green dots track the peak positions of the bulk band which reveal a gap opening of $\sim$85 meV. (b) Same as (a) but of β-Bi$_4$I$_4$. A gap opens at $k_b = 0$ of $\sim$100 meV. (c) Band image along the k_b-axis on the (201) surface of α-Bi$_4$I$_4$ as well as its corresponding EDC stacks. The blue dots track the surface state which reveal a $\sim$35 meV gap opening. (d) Same as (c) but the (100) surface of β-Bi$_4$I$_4$. A gapless Dirac surface state is observed.

first examine the β phase. On the (001) surface [Fig. 3.12(b)], we observe a clear gap in all the bulk gaps and no additional surface Dirac crossings. This can be confirmed from the energy distribution curve (EDC) stacks of the bands across $\bar{\mathrm{M}}$ [Fig. 3.12(b)], where the green dots track the bulk band dispersion and reveal a gap of $\sim$100 meV. On the (100) surface, a quasi-1D Dirac surface state exists inside the bulk band gap [Fig. 3.12(d)]. Particularly at the $\bar{\Gamma}$ and $\bar{\mathrm{Z}}$ points, the surface states are gapless within the resolution of measurements at 350 K. These combined measurements on both the

(001) and (100) surfaces demonstrate that the high-temperature β-Bi$_4$I$_4$ is a weak TI where only selected surfaces possess an even number (two here) of gapless Dirac cones [15, 83]. In the α phase, all the observed bands on the (001) surface are also gapped [Fig. 3.12(a)]. A gap of $\sim$85 meV can be further seen from the bands tracked by the EDC stacks in Fig. 3.12(a). On the (201) surface, from a high-resolution measurement taken with 30 eV photons at 10 K [Fig. 3.12(c)], we observe a gap of $\sim$35 meV clearly in the EDC stacks, indicating a gapped surface state within a bulk band gap. This is consistent with our theoretical prediction and calculation of a higher-order TI scenario of α-Bi$_4$I$_4$, where both the bulk bands and surface bands are required to be gapped, hosting gapless hinge states inside the surface gap.

3.8.2 Gate-Tunable Transport in α-Bi$_4$I$_4$ Field Effect Transistors

A plethora of hinge state signatures can be obtained in a gate-tunable multi-terminal device. In such a device, the Fermi energy can be tuned by a gate voltage into the bulk, surface, and hinge states. (i) While the surface states have a much larger density of states (DOS), a 1D helical mode has a constant DOS, i.e., $1/\pi\hbar v_F$. The total DOS in the surface state gap can be used to estimate the number of hinges, step edges, or/and stacking faults that host 1D helical modes. The detailed DOS of α-Bi$_4$X$_4$ under different surface terminations are given in Appendix. A.5. (ii) The sign of Hall coefficient can indicate whether the Fermi energy crosses the electron or hole surface band and infer the size of surface state gap. (iii) In the surface state gap, nonlocal conductances can be analyzed to determine the hinge state pattern and layer stacking order. (iv) From weak antilocalization in magnetotransport, the temperature dependence of dephasing lengths can be extracted. The Nyquist length L_n and the phase coherence length L_φ should both scale as $T^{-1/3}$, $T^{-1/2}$, and $T^{-3/4}$ for the hinge, surface, and bulk states, respectively [108–110]. (v) The spatial distribution of surface and hinge conductances can be mapped by MIM. (vi) The hinge states have Fermi velocities $\sim 5 \times 10^5$ m/s[5] and confinement lengths < 1 nm, similar to the case of bismuthene [111]. The anticipated Tomonaga-Luttinger liquid behavior can be probed via the power-law dependences on energy and temperature in tunneling spectroscopy [111–113].

Josephson transport in devices with superconducting contacts also provides excellent means to probe the hinge states. The bulk supercurrent should display a rapidly decaying Fraunhofer pattern, whereas the one through the hinge (and side surface) states should exhibit slowly decaying oscillations typical for a SQUID [39, 75, 114]. While the Fraunhofer pattern is more dominant in a thicker sample, the SQUID-like behavior depends only on the area of the hinge-state loop(s). As a result, the evolution of the asymmetry of the critical current with a magnetic field can be exploited to distinguish the hinge states and determine their specific pattern.

In our recent publication Ref. [108], we observe a Dirac-like longitudinal resistance peak and a sign change in the Hall resistance; their temperature dependences suggest competing transport mechanisms: a hole-doped insulating bulk and one or more gate-tunable ambipolar boundary channels. Our combined transport, photoemission results indicate that the gate-tunable channels likely arise from novel gapped side surface states, two-dimensional (2D) TI in the bottommost layer, and/or helical hinge states of the upper layers. Markedly, a gate-tunable supercurrent is observed in an α-$\mathrm{Bi_4I_4}$ Josephson junction, underscoring the potential of these boundary channels to mediate topological superconductivity.

---

[5] For α-Bi_4Br_4 hinge states, the Fermi velocities are 4.19×10^5 m/s in Fig. 3.6(a) and 5.58×10^5 m/s in Fig. 3.6(c). For α-Bi_4I_4 hinge states, the Fermi velocities are 4.63×10^5 m/s and 3.79×10^5 m/s in Fig. 3.8(b).

3.8.3 Stacking-dependent room-temperature quantum spin Hall edge states in α-$\mathrm{Bi_4Br_4}$ thin-films

In our recent work Ref. [45], we use scanning tunneling microscopy to provide spectroscopic evidence for a room-temperature quantum spin Hall edge state on the surface of multilayer α-$\mathrm{Bi_4Br_4}$. Firstly, we find that a monolayer step edge of α-$\mathrm{Bi_4Br_4}$ exhibits a large insulating gap of over 200 meV, and hosts an in-gap gapless state.

We now consider a bilayer step edge of α-$\mathrm{Bi_4Br_4}$. From the perspective of the 2D $\mathbb{Z}_2$ invariant, the hybridization occurs between the helical edge modes in each monolayer and opens an energy gap. But as we discussed in Sec. 3.6 and 3.7, specific to this material, rooted in the fact that the inversion center is in the monolayer instead of in the center of a bilayer, the left and right bilayer edges have different geometries [Fig. 3.13(a)]. Here we call the bilayer system in Fig. 3.13(a) the BA-bilayer, following the convention in

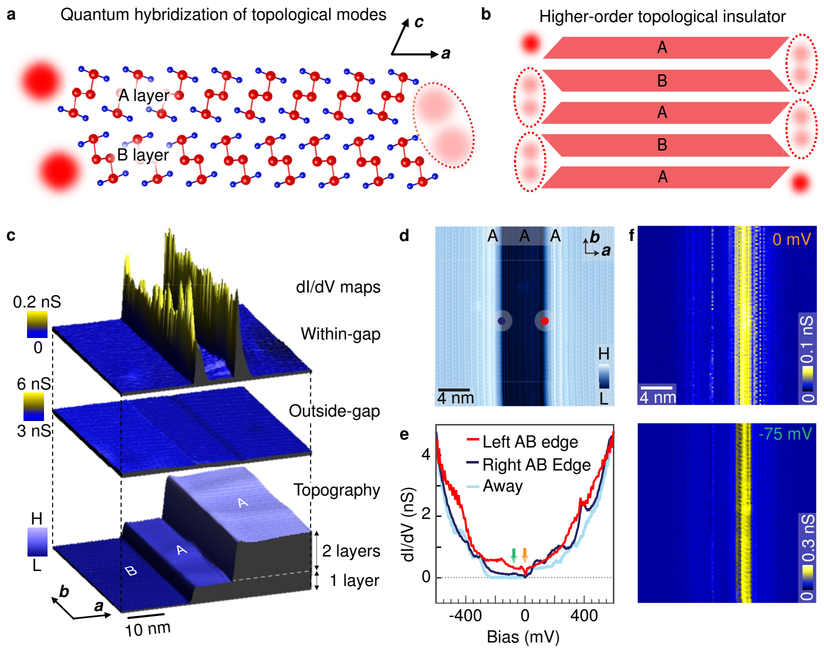

Figure 3.13: (a) Side view of an AB-bilayer. The hybridization of edge state is destructive, as illustrated by the lighter color of the edge states (red spheres). (b) Construction of a higher-order topological insulator based on the hybridization mechanism in (a). (c) Spectroscopic imaging of the crystalline steps. The bottom panel shows the topographic image of two-step edges. The middle panel shows the corresponding differential conductance map obtained at energy outside the insulating gap. The top layer shows the corresponding differential conductance map obtained at energy inside the insulating gap, revealing pronounced edge states. (d) Topographic image of two adjacent bilayer atomic step edges forming a trench. (e) Differential spectra taken at the left AB bilayer step edge (red), right AB bilayer step edge (violet), and away from the edges (blue). Red and violet dots in panel (d) denote the respective positions on the left and right AB edges where the differential spectra are taken. (f) Differential conductance map, taken at $V = 0$ mV and -75 mV [marked with color-coded arrows in the differential spectra in panel (e)] shown in two layers. $V = 0$ mV and -75 mV, both of which are inside the insulating gap.

Sec. 3.6. On the left, the edges of the A and B layers have a facing angle larger than 180°, while on the right the facing angle is smaller than 180°. This inversion asymmetry leads to stronger hybridization of the monolayer edge states on the right. Similarly, for a AB-bilayer, it can be inferred that the left side has stronger hybridization (not shown). Figure 3.13(c) shows a case region containing both a monolayer step edge and a left edge of BA-bilayer. The associated $\mathrm{d}I/\mathrm{d}V$ mapping confirms the existence of in-gap edge states in both cases. To visualize the asymmetric hybridization of the edge states depicted in Fig. 3.13(a), we extensively scan the crystal to find an area containing both left and right BA-bilayer step edges as shown in Fig. 3.13(d). The differential spectra taken at the two BA-bilayer step edges, as shown in Fig. 3.13(e), reveal their dramatically different behaviors. The in-gap state for the right-BA bilayer edge is substantially suppressed compared with that on the left-BA bilayer edge. The inversion asymmetry of the bilayer edge state is further visualized in Fig. 3.13(f), which demonstrates the $\mathrm{d}I/\mathrm{d}V$ maps of the same area as in Fig. 3.13(d), taken at two representative energies within the insulating gap. It is shown that the edge state mainly shows up for the left-BA bilayer edge, in agreement with the picture in Fig. 3.13(a).

Note that this result of the bilayer system is clearly consistent with our prediction in Figs. 3.6(b) and 3.6(d), except that the number of layers is in the bulk limit in Fig. 3.6 ($N_c > 40$). In fact, as shown in Fig. 3.14(d), we find that α-$\mathrm{Bi_4Br_4}$ very quickly reaches the limit of the HOTI with the unique stacking-dependent hinge patterns. The energy gap at the left-BA bilayer

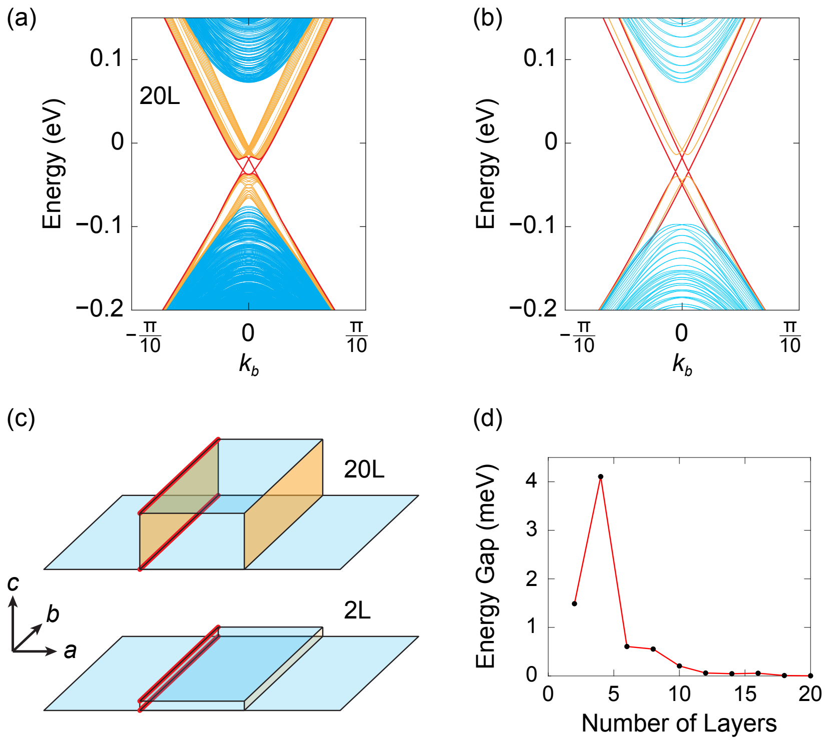

Figure 3.14: Calculated bilayer and twenty-layer step-edge states. (a) The edge-projected band structure for a (001) twenty-layer ribbon on the top surface of α-Bi$_4$Br$_4$. The cyan bands are from the bulk and (001) surfaces of the system. The orange bands are from the (100) and ($\bar{1}$00) side surfaces of the ribbon. The red bands are the gapless hinge states. Due to the inversion asymmetry of even-layer systems, the bands are singly degenerate at each k_b. The ribbon is infinitely long in the b direction and 50-chain wide in the a direction. (b) The same as a but for a bilayer ribbon. The two helical edge states from the two monolayers are gapped at one side (orange) but remain gapless at the other side (red). (c) The real space schematics of the surface and hinge/edge states in [(a) and (b)]. (d) Calculated edge gap of (001) even-layers.

edge is already $\sim$1 meV [Red bands in Fig. 3.14(b)] in large contrast to the energy gap at the right-BA bilayer edge of $\sim$20 meV [Orange bands in Fig. 3.14(b)]. In addition to the BA bilayer, we also investigated the BABA tetralayer step edge in the experiment and obtained qualitatively the same result as the BA bilayer case, which is also consistent with our prediction.

3.9 Discussion

Although both are HOTIs with helical hinge states, α-$\mathrm{Bi_4Br_4}$ is more intrinsic (bulk-obstructed) whereas α-$\mathrm{Bi_4I_4}$ is more extrinsic (boundary-obstructed) [106, 115]. As featured in Figs. 3.6 and 3.8, attaching a 2D TI to the (001) surface can annihilate an existing hinge state of α-$\mathrm{Bi_4I_4}$ but not that of α-$\mathrm{Bi_4Br_4}$. Markedly, their clear distinction in the hinge state pattern highlights the critical role played by the location of inversion center that has so far been overlooked in the literature. Fundamentally, as only the $\mathcal{T}$ symmetry is required to protect a local 1D helical mode, the helical hinge states are robust against the $\mathcal{P}$ symmetry breaking, as long as the perturbation neither closes the surface band gaps nor hybridizes the states at different hinges (or edges). This is in sharp contrast to the case of topological mirror insulators and superconductors [105, 116], in which the mirror symmetry breaking exclusively removes the gapless boundary modes. Given that the symmetry indicators of α-$\mathrm{Bi_4I_4}$ are completely trivial [29–31], our results imply that there are likely to be many topological materials beyond the scope of the current scheme for the classification of topological materials and awaiting to be discovered.

We stress that the effective models for the side surface states in Sec. 3.7 are continuum models in the chain direction but lattice models in the stacking direction. As the side surface states can be constructed by the helical edge states of (001) monolayers that are 2D $\mathbb{Z}_2$ TIs, it does not exist any lattice model to account for the surface states in the chain direction [51, 117]. However, this is not the case in the stacking direction, as there are nevertheless dual surface Dirac cones that are gapless in the WTI case but gapped in the HOTI case. Best displayed by the quasi-1D $\mathrm{Bi_4X_4}$, this special feature reflects the intimate relations between the HOTI, WTI, and 2D TIs.

Given that the (001) monolayers of the four materials are all 2D $\mathbb{Z}_2$ TIs as shown in Fig. 3.2, one may wonder whether their (100) ((201) for α-$\mathrm{Bi_4I_4}$) films are also TIs. Our MLWF-based calculations and effective tight-binding models both indicate that their monolayers and the β-$\mathrm{Bi_4X_4}$ film of any thickness are $\mathbb{Z}_2$ trivial. However, any α-$\mathrm{Bi_4Br_4}$ (100) film thicker than three layers[6] is a $\mathbb{Z}_2$ TI. This can be understood by the top panels of Fig. 3.6: each scenario has one hinge state at the top surface and one at the bottom. As the (100) thickness decreases, the two hinge states turn into the two edge states, as long as the inter-edge coupling in a (001) layer is sufficiently small compared with the inter-edge coupling between two (001) layers. On the contrary, an α-$\mathrm{Bi_4I_4}$ (201) film of any thickness is $\mathbb{Z}_2$ trivial. As each surface in the top panels of Fig. 3.8 has either zero or two hinge states, for a (201) film either there is no edge state or the dual edge states acquire a hybridized gap, though, which is small for a thick film. This offers a different perspective on the distinction between the two HOTIs.

---

[6] The thinest (100) TI film is the tetralayer in our MLWF-based computation. It is the hexalayer instead in our effective tight-binding model calculation. The latter can be adjusted to match the former without affecting the bulk and surface band topologies by changing t_a from 181.67 meV to 140.00 meV in Table A.2.

Our results establish a new TI physics paradigm and a unique quasi-1D material platform for exploring the interplay of geometry, symmetry, topology, and interaction. Besides the discussed experiments, studies on the coupling to ferromagnet, superconductor, or their linear junctions, the possible topological phase transitions under strain [83], and the influence of electron-electron interactions would be extremely interesting.

Chapter 4

Broken sublattice symmetry states in Bernal stacked multilayer graphene

4.1 Introduction

Ultrathin multilayer graphene has been extensively studied in the literature over the last decade as a promising platform for electronic devices [2, 118–120] and energy storage applications [121] that take advantage of the superlative properties of graphene. From a more fundamental physics point of view, few-layer graphenes are interesting because their band structure embodies the chiral nature of the Dirac cones near the charge neutrality point which can manifest in transport and optical experiments. Clear signatures of electron-electron interactions observed through scanning probes [122, 123] and transport experiments [124–127] have signaled interesting many-body effects. Remarkably, the predictions of interaction driven band gaps in Bernal stacked bilayer [128] and rhombohedral trilayer graphene [129] have been speculated to be accompanied by spin/valley resolved spontaneous Hall phases [130–133] for a variety of possible ground-state configurations among quasi-degenerate states. Other possible ordered phases suggested near the charge neutrality point in bilayer graphene include nematic phases with broken rotational symmetry [124, 134–139], and Fermi surface instabilities in both $\ell = 0, 1$ channels in the presence of a finite carrier doping and electric fields [140]. Recent experiments in ultraclean Bernal stacked multilayer graphenes signal the formation of electron-electron interaction driven ordered phases [141, 142].

In this chapter, we analyze the nature of the electron interaction driven ordered ground-state phases in Bernal stacked tetralayer graphene subject to perpendicular external electric fields and the associated Hall conductivities that can be measured in transport experiments. We show that the electronic structure consisting of light-mass and heavy-mass band doublets follows an effective Hund's rule of the sublattice pseudospins when a perpendicular external electric field is applied, allowing to introduce qualitative changes in the associated Hall conductivities. Interestingly, in a certain range of electric fields, a ground state with a non-vanishing charge Hall conductivity appears that should be measurable by conventional Hall experiments. Analysis of the ordered phases in Bernal stacked multilayer graphene beyond tetralayer acquires a more complex character due to the appearance of additional pseudospin doublets and mixing between them. Within a minimal multiband model, we show that the interaction driven band gap and broken sublattice symmetry can appear in even-layer graphenes, whereas the gaps for odd-layer graphenes are suppressed, exhibiting an even-odd effect for the energy gap size.

This chapter is largely based on my publication, Ref. [143].

4.2 Effective model and electron-electron interaction

We use a π-band minimal continuum model for multilayer graphene in which only nearest-neighbor intralayer hopping t_0 and interlayer hopping t_1 for the full π-bands are retained. The non-interacting Hamiltonian is

$$\hat{H}_0 = \sum_{\boldsymbol{k},\sigma,\sigma'} \hat{c}^{\dagger}_{\boldsymbol{k},\sigma} \varepsilon^{(0)}_{\sigma\sigma'}(\boldsymbol{k}) \hat{c}_{\boldsymbol{k},\sigma'}, \tag{4.1}$$

where $\boldsymbol{k}$ is the wavevector measured from a valley K or K', σ is a collective index representing spin (u/d), valley, sublattice (A/B), and layer ($n = 1, 2, \cdots$) degrees of freedom, $\hat{c}^{\dagger}_{\boldsymbol{k},\sigma}$ ($\hat{c}_{\boldsymbol{k},\sigma}$) is the electron creation (annihilation) operator for $\boldsymbol{k}$ and σ, and $\varepsilon^{(0)}_{\sigma\sigma'}(\boldsymbol{k})$ is the non-interacting Hamiltonian matrix element for Bernal stacked multilayers. For the tight-binding parameters, we use the LDA parameters of graphite $t_0 = 2.598$ eV and $t_1 = 0.377$ eV [144, 145].

We include the effect of electron-electron interactions within a mean-field Hartree-Fock approximation,

$$\hat{H}_{\mathrm{MF}} = \hat{H}_0 + \sum_{\boldsymbol{k},\sigma,\sigma'} \hat{c}^{\dagger}_{\boldsymbol{k},\sigma} \varepsilon^{(\mathrm{HF})}_{\sigma\sigma'}(\boldsymbol{k}) \hat{c}_{\boldsymbol{k},\sigma'}. \tag{4.2}$$

The matrix element of the Hartree-Fock term is given by

$$\begin{aligned} \varepsilon^{(\mathrm{HF})}_{\sigma\sigma'}(\boldsymbol{k}) &= \delta_{\sigma\sigma'} \sum_{\boldsymbol{k}',\sigma'} V_{nn'}(0) \left\langle \hat{c}^{\dagger}_{\boldsymbol{k}',\sigma'} \hat{c}_{\boldsymbol{k}',\sigma'} \right\rangle \\ &-\delta_{ss'} \sum_{\boldsymbol{k}'} V_{nn'}(|\boldsymbol{k} - \boldsymbol{k}'|) \left\langle \hat{c}^{\dagger}_{\boldsymbol{k}',\sigma'} \hat{c}_{\boldsymbol{k}',\sigma} \right\rangle, \end{aligned} \tag{4.3}$$

where n and s denote the layer and spin, respectively. $V_{nn'}(q) = \frac{2\pi e^2}{\epsilon_r q} e^{-|n-n'|qd}$ is the Coulomb interaction matrix where $d = 3.35$ Å is the interlayer separation and ϵ_r is the background dielectric constant. The first and second terms in the right-hand side of Eq. (4.3) represent the classical Hartree and exchange Fock contributions, respectively. Note that the Hartree terms reduce to potential differences between the layers when we take the proper limit at $q = 0$. Here we take a rather small value of the interaction strength $\alpha \equiv \frac{e^2}{\epsilon_r \hbar v}$, where $v = \frac{\sqrt{3}}{2}\frac{t_0 a}{\hbar}$ is the Fermi velocity of monolayer graphene and $a = 2.46$Å is the lattice constant, to effectively account for the overestimation of the exchange by long-ranged Coulomb repulsion in a Hartree-Fock theory that misses out the screening effects of π and σ orbitals in graphene. (Simple screening models such as the static Thomas-Fermi approximation for the exchange interaction do not change the qualitative picture on the sublattice symmetry breaking presented in this paper.) The specific value $\alpha = 0.1$ is adopted to match the experimentally observed gap size in bilayer graphene [123, 126, 127].

To overcome computational challenges posed by the absence of analytic form of wavefunctions in multilayer graphene, we use the rotational transformation method [146] in which the wavefunction at an arbitrary angle is obtained by a stacking dependent unitary transformation of the wavefunction at a specific angle. Moreover, we omit the inter-valley interaction which is negligibly small, and each one of the four spin/valley flavors are treated independently.

4.3 Interaction-driven gapped phases in Bernal stacked tetralayer graphene

4.3.1 Ground states with broken sublattice symmetry

The experimentally observed band gap in Bernal stacked tetralayer graphene suggests the presence of electron-electron interaction driven symmetry breaking [141, 142]. Here, we show that the band gap opens due to interaction driven sublattice symmetry breaking and its internal structure consists of light-mass and heavy-mass band doublets whose charge densities polarize towards opposite out-of-plane directions. A sufficiently strong perpendicular external electric field can flip their polarization directions in the order of increasing effective mass values.

In Fig. 4.1, we show a comparison of the non-interacting and Hartree-Fock energy band structures, and corresponding ground-state wavefunction amplitudes and charge polarizations near the Fermi energy. The electronic structure of Bernal stacked multilayer graphene can be understood from the chiral decomposition rules of arbitrarily stacked multilayers [3, 147] where the ABAB tetralayer is the simplest example involving more than one massive band. In the absence of electron-electron interactions, the low-energy band structure of ABAB stacking is described by two bilayer-like pseudospin doublets with different effective masses, whose wavefunctions near the Fermi energy are mainly localized at outer layer (1A, 4B) and inner layer (2B, 3A) sublattice sites that define the pseudospin basis for the light

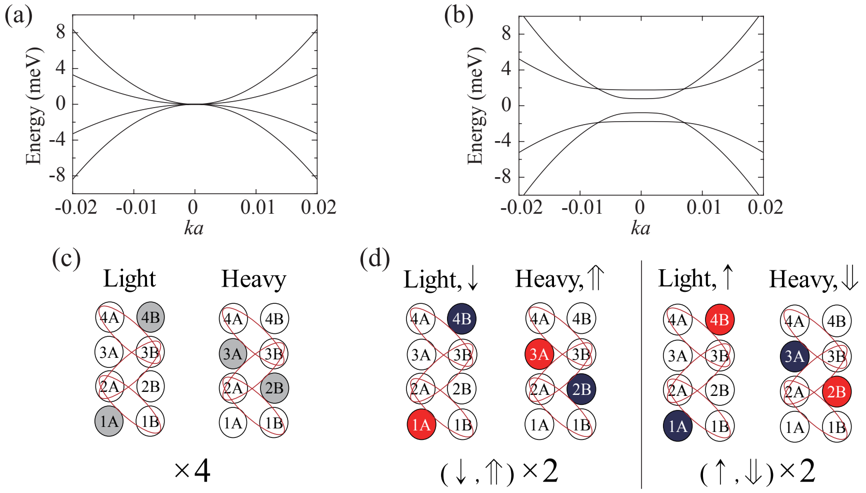

Figure 4.1: Electronic structure and zero-energy wavefunction configurations near the K or K' valley for ABAB tetralayer graphene obtained respectively from (a), (c) the non-interacting continuum model and (b), (d) a self-consistent Hartree-Fock calculation. Two pseudospin doublets are labeled by “Light” or “Heavy” depending on their effective mass of the energy band. In the case of non-interacting model, all four spin/valley flavors have the same wavefunction configuration with localized wavefunctions on the gray sublattices, as shown in (c). When electron-electron interactions are turned on, the sublattice symmetry is broken for both doublets transferring charges either from A to B sublattices or vice versa, as indicated in red (positive charge) and blue (negative charge) color in (d). The $(\downarrow, \Uparrow)$ and $(\uparrow, \Downarrow)$ labels represent two possible configurations of opposite charge polarization towards the top and bottom layers corresponding to the light and heavy mass bands.

and heavy mass bands, respectively, as shown in Fig. 4.1(c). In the presence of electron-electron interactions, the sublattice symmetry of the two-fold degenerate pseudospin doublets in the occupied bands is broken by transferring charge either from A to B sublattices or vice versa for both doublets (but not from A to B for one doublet and from B to A for other doublet), resulting in the gapped band structure with the same *sublattice* polarization direction.

Sublattice symmetry breaking in tetralayer graphene can be considered as the generalization of the case of bilayer graphene system, which has one pseudospin (per spin and valley) whose direction is out-of-plane as a result of the electron-electron interactions [128]. For each spin/valley flavor, the charge polarizations of the light-mass and heavy-mass band doublets can be represented as $(\downarrow, \Uparrow)$ or $(\uparrow, \Downarrow)$, where the first (second) arrow in the parenthesis denotes the charge polarization for the light (heavy) mass band. The charge polarizations for light and heavy bands point in opposite directions but towards the same sublattices, leading to same sign Chern numbers $(+1,+1)$ or $(-1,-1)$, as shown in the Fig. 4.1(d). Note that the Chern number changes its sign at the opposite valley. We will discuss later on the states with the same polarization directions such as $(\downarrow, \Downarrow)$ or $(\uparrow, \Uparrow)$ with a vanishing net Chern number for a single spin/valley flavor, which are possible in the presence of an external electric field. Thus, we can expect a variety of ground states as a function of an external electric field, where different types of Hall conductivities can result depending on the polarization of light-mass and heavy-mass band doublets for each flavor.

4.3.2 Spin-valley degrees of freedom

Similar to the discussions for pseudospin magnetism in bilayer graphene [128] we can classify the different states into flavor antiferro, ferri, and ferro states. Flavor antiferro states have two flavors in $(\downarrow, \Uparrow)$ configuration and the other two in $(\uparrow, \Downarrow)$ configuration at zero field, so that no net charge polarization exists.

The internal arrangement of the sublattice pseudospins has a direct impact on the Hall transport properties of the system. Whenever the charge polarization direction flips, the associated Chern number changes its sign due to the change in the sublattice potential in the doublet. We distinguish the spin Hall (SH), valley Hall (VH), charge Hall (CH), and spin resolved valley Hall (SV) contributions of the conductivities. From the Chern numbers $C_{v,s}$ ($v = K, K'$ and $s = \mathrm{u}, \mathrm{d}$) of the pseudospin doublets at each valley/spin flavor, the various quantum Hall conductivities can be evaluated as

$$\begin{aligned}
\sigma_{\mathrm{SH}} &= \frac{e^2}{h}\left(C_{K,\mathrm{u}} - C_{K,\mathrm{d}} + C_{K',\mathrm{u}} - C_{K',\mathrm{d}}\right), && \text{(4.4a)}\\
\sigma_{\mathrm{VH}} &= \frac{e^2}{h}\left(C_{K,\mathrm{u}} + C_{K,\mathrm{d}} - C_{K',\mathrm{u}} - C_{K',\mathrm{d}}\right), && \text{(4.4b)}\\
\sigma_{\mathrm{CH}} &= \frac{e^2}{h}\left(C_{K,\mathrm{u}} + C_{K,\mathrm{d}} + C_{K',\mathrm{u}} + C_{K',\mathrm{d}}\right), && \text{(4.4c)}\\
\sigma_{\mathrm{SV}} &= \frac{e^2}{h}\left(C_{K,\mathrm{u}} - C_{K,\mathrm{d}} - C_{K',\mathrm{u}} + C_{K',\mathrm{d}}\right). && \text{(4.4d)}
\end{aligned}$$

where σ_{SH}, σ_{VH}, σ_{CH}, and σ_{SV} indicates the quantum spin Hall conductivity, quantum valley Hall conductivity, quantum anomalous Hall conductivity, and quantum spin-valley Hall conductivity, respectively. Within the flavor antiferro states, we classify different Hall phases [131, 132]: layer antiferromagnetic (LAF) phase with the spin dependent but valley independent sublattice potential, quantum spin Hall (QSH) phase with both the spin and valley dependent sublattice potential, and quantum anomalous Hall (QAH)

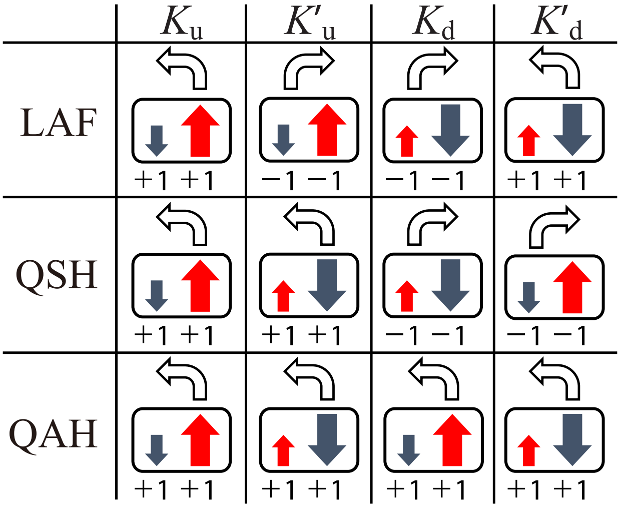

Figure 4.2: Schematic picture of the ground-state configuration and corresponding spontaneous Hall effect at zero external electric field for three possible flavor antiferro states: LAF, QSH and QAH. Arrows in the square box and numbers below the box at each spin/valley flavor represent pseudospin polarizations and corresponding Chern numbers, respectively, whereas the arrows above the box indicate the corresponding net current directions expected in the Hall measurement.

phase with the valley dependent but spin independent sublattice potential, as schematically shown in Fig. 4.2.

Flavor ferro states have all four flavors in the same pseudospin configuration. The flavor ferri states have one distinct flavor with respect to other three. Since the number of $(\downarrow, \Uparrow)$ and $(\uparrow, \Downarrow)$ configurations are different in flavor ferro and ferri states at zero field, non-zero net charge polarization exists for these states. From the Hartree energy cost considerations, the metastable states with the lowest total energy are expected to be flavor antiferro when there is no external electric field perpendicular to the graphene

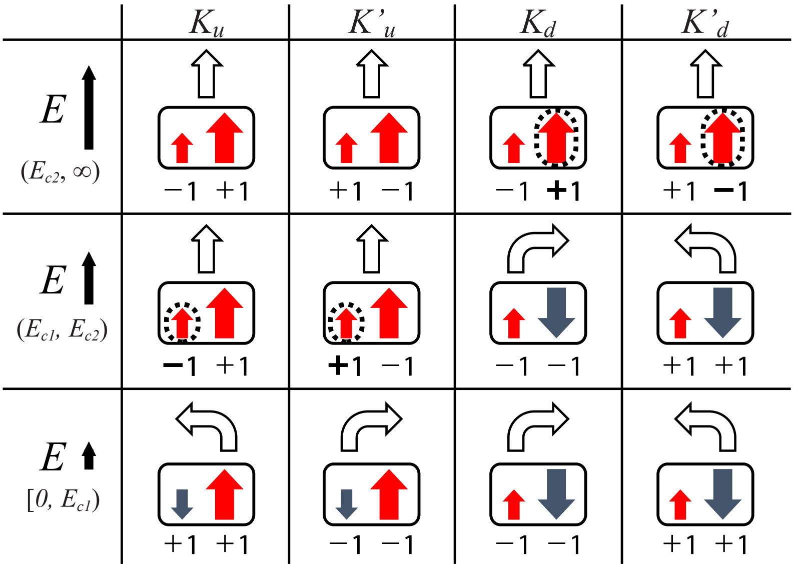

Figure 4.3: The evolution of the layer antiferromagnetic state under a perpendicular external electric field, keeping the flavor degeneracy of the system. Arrows in the square box and numbers below the box at each spin/valley flavor represent pseudospin polarizations and corresponding Chern numbers, respectively, whereas the arrows above the box indicate the corresponding net current directions expected in the Hall measurement. The change in the charge polarization by applying a perpendicular electric field is denoted by the dashed circle.

layers.

4.4 Electric field induced “Hund’s rule” and Hall effects

Now let us consider the effect of a perpendicular external electric field that can introduce a richer phase diagram. The presence of an electric field is able to reorganize the charge polarization of the sublattice pseudospins in

Table 4.1: Spontaneous quantum Hall conductivities in units of e^2/h for the antiferro states in Bernal stacked tetralayer graphene under a perpendicular external electric field. Here, $E_{\rm c1} = 0.025$ mV/Å and $E_{\rm c2} = 0.879$ mV/Å.

$E_{\rm ext}$	LAF				QSH				QAH			
	SH	VH	CH	SV	SH	VH	CH	SV	SH	VH	CH	SV
$E_{\rm c2}$	0	0	0	0	0	0	0	0	0	0	0	0
$E_{\rm c1}$	0	-4	0	4	4	-4	0	0	0	-4	4	0
0	0	0	0	8	8	0	0	0	0	0	8	0
$-E_{\rm c1}$	0	4	0	4	4	4	0	0	0	4	4	0
$-E_{\rm c2}$	0	0	0	0	0	0	0	0	0	0	0	0

each spin/valley flavor. (Here we evolve a pseudospin configuration under an electric field without changing its antiferro, ferri or ferro character keeping the same flavor degeneracy. The lowest total energy state among them is discussed in the following section.)

4.4.1 Flavor antiferro states

We begin by considering the flavor antiferro state consisting of $(\downarrow, \Uparrow) \times 2$ and $(\uparrow, \Downarrow) \times 2$ at zero field. When an external electric field is increased beyond the first critical field of $E_{\rm c1} = 0.025$ mV/Å, the polarization of the light-mass band changes its sign first due to smaller interaction-induced sublattice potential compared with that for the heavy-mass band, resulting in the $(\uparrow, \Uparrow) \times 2$ and $(\uparrow, \Downarrow) \times 2$ configuration. A second critical electric field of $E_{\rm c2} = 0.879$ mV/Å is able to flip all pseudospins leading to a ground state with four identical copies of the band doublets $(\uparrow, \Uparrow) \times 4$, and thus resulting in flavor ferro state. Figure 4.3 schematically illustrates this process and resulting transport properties in one of the flavor antiferro states, the LAF phase, assuming a spin dependent but valley independent sublattice potential. Thus, polarizations of the pseudospin doublets arising from the interaction induced sublattice symmetry breaking are aligned by the external electric field in the order of increasing effective mass. The rest of the two flavor antiferro states, QSH and QAH phases also exhibit the same behavior as the LAF phase, except for the different spontaneous quantum Hall conductivities. The change in Hall coefficients of all the three flavor antiferro states under the external field is shown in Table 4.1. We observe that the pseudospin ordering behavior under external electric field is also very similar in 6-layer Bernal-stacked graphene. Similar to the tetralayer case, the pseudospins with lighter mass flips first. See Appendix B.1 for details.

4.4.2 Flavor ferri and ferro states

It can be shown that this simple "Hund's rule" type pseudospin ordering applies also to flavor ferri and ferro states. The evolution of a flavor ferri state with the minority pseudospin configuration on K'_{d} and that of a flavor ferro state under a perpendicular external electric field are depicted in Fig. 4.4. The corresponding Chern numbers for each state are represented in Table 4.2. Note that in zero external electric field, there are eight ferri states (from the two possible choice of minority configuration between (↑,⇓) and (↓,⇑) on four possible spin/valley flavors) and two ferro states (from the two possible choice of majority configuration).

As shown in Table 4.2, in the case of ferri states, all the types of Hall

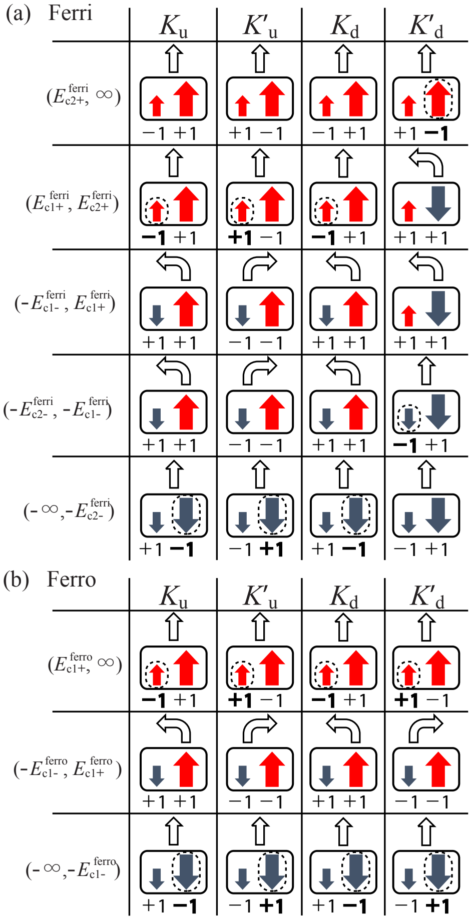
(a) Ferri
K_u
K'_u
K_d
K'_d
$(E^{ferri}_{c2+}, \infty)$
−1 +1
+1 −1
−1 +1
+1 −1
$(E^{ferri}_{c1+}, E^{ferri}_{c2+})$
−1 +1
+1 −1
−1 +1
+1 +1
$(-E^{ferri}_{c1-}, E^{ferri}_{c1+})$
+1 +1
−1 −1
+1 +1
+1 +1
$(-E^{ferri}_{c2-}, -E^{ferri}_{c1-})$
+1 +1
−1 −1
+1 +1
−1 +1
$(-\infty, -E^{ferri}_{c2-})$
+1 −1
−1 +1
+1 −1
−1 +1
(b) Ferro
K_u
K'_u
K_d
K'_d
$(E^{ferro}_{c1+}, \infty)$
−1 +1
+1 −1
−1 +1
+1 −1
$(-E^{ferro}_{c1-}, E^{ferro}_{c1+})$
+1 +1
−1 −1
+1 +1
−1 −1
$(-\infty, -E^{ferro}_{c1-})$
+1 −1
−1 +1
+1 −1
−1 +1

Figure 4.4: The evolution of ABAB tetralayer graphene under a perpendicular external electric field for (a) a flavor ferri state with the minority pseudospin configuration ($\uparrow$, $\Downarrow$) on K'_d and (b) a flavor ferro state with ($\downarrow$, $\Uparrow$) for all four flavors. Arrows in the square box and numbers below the box at each spin/valley flavor represent pseudospin polarizations and corresponding Chern numbers, respectively, whereas the arrows above the box indicate the corresponding net current directions expected in the Hall measurement. The change in the charge polarization by applying a perpendicular electric field is denoted by the dashed circle.

coefficients are non-zero for $-E^{\mathrm{ferri}}_{\mathrm{c2-}} < E < E^{\mathrm{ferri}}_{\mathrm{c2+}}$. This is the reason why the ferri state is also called “All” state [131–133]. Also note that only the

Table 4.2: Spontaneous quantum Hall conductivities in units of e^2/h under a perpendicular external electric field in ABAB tetralayer for the ferri and ferro states in Fig. 4.4. Here, $E^{\text{ferri}}_{c1+} = 0.019$, $E^{\text{ferri}}_{c2+} = 0.943$, $E^{\text{ferri}}_{c1-} = 0.031$, and $E^{\text{ferri}}_{c2-} = 0.815$ meV/Å for the ferri state, whereas $E^{\text{ferro}}_{c1+} = 0.013$ and $E^{\text{ferro}}_{c1-} = 0.753$ meV/Å for the ferro state.

E	Ferri			
	SH	VH	CH	SV
E^{ferri}_{c2+}	0	0	0	0
E^{ferri}_{c1+}	-2	-2	2	2
0	-4	4	4	4
$-E^{\text{ferri}}_{c1-}$	-2	6	2	2
$-E^{\text{ferri}}_{c2-}$	0	0	0	0

E	Ferro			
	SH	VH	CH	SV
E^{ferro}_{c1+}	0	0	0	0
0	0	8	0	0
$-E^{\text{ferro}}_{c1-}$	0	0	0	0

valley Hall coefficients change their signs in the opposite field direction. In the case of ferro states, only the valley Hall coefficients are non-zero for $-E^{\text{ferro}}_{c1-} < E < E^{\text{ferro}}_{c1+}$.

4.4.3 Multiple hysteresis of layer charge polarization

Figure 4.5 shows the external field dependence of the total charge polarization for flavor antiferro, ferri and ferro states tracing a single metastable configuration. Here we define the total charge polarization ζ in tetralayers taking into account the layer separations as

$$\zeta = \frac{\frac{3}{2}n_4 + \frac{1}{2}n_3 - \frac{1}{2}n_2 - \frac{3}{2}n_1}{n_4 + n_3 + n_2 + n_1}, \tag{4.5}$$

where n_i is the electron density at i-th layer. Note that in the case of ferri and ferro states, the evolution of states depends on the initial condition and the sweep direction of the field, exhibiting hysteretic behavior associated

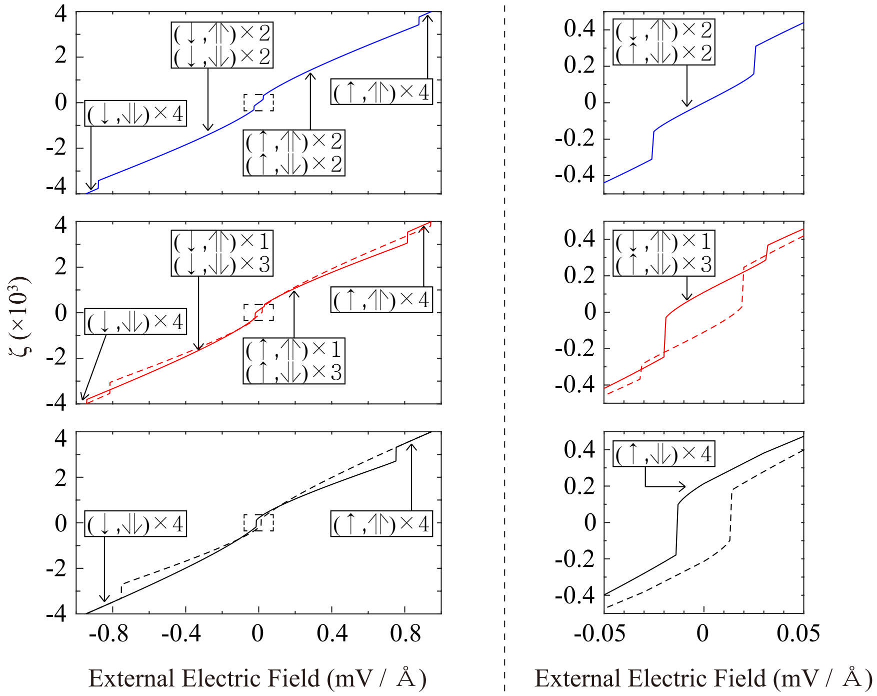

Figure 4.5: (Left) External field dependence of the total charge polarization ζ defined in Eq. (4.5) for flavor antiferro (top), ferri (middle) and ferro (bottom) states. The solid and dashed lines indicate evolutions of states from two different initial states with reversed polarization direction for each pseudospin. For each solid line, the pseudospin configurations are depicted. (Right) Zoomed view of the dashed rectangular area in the left panel.

with the broken sublattice symmetry at zero field, which is analogous to the bilayer graphene system [128].

4.5 Generalization to thicker multilayer stacks

In Bernal stacked multilayer graphene beyond tetralayer, there are several additional factors that influence electronic structure near the Fermi level

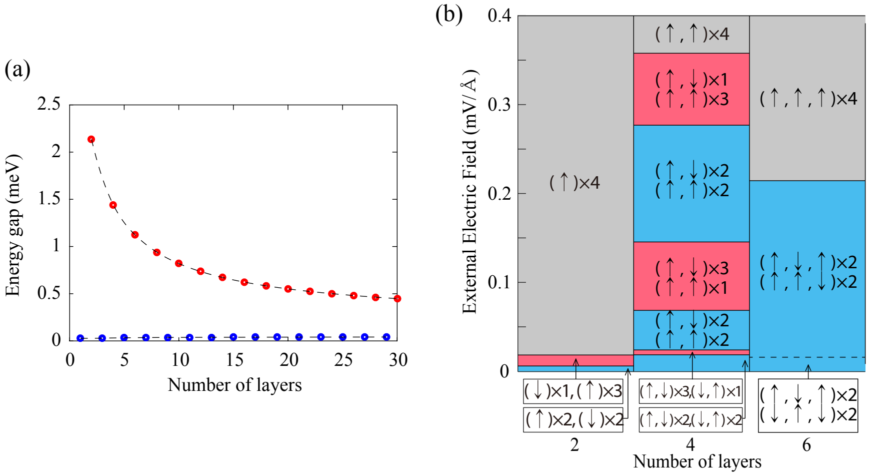

Figure 4.6: (a) Energy band gap as a function of the number of layers in the absence of a perpendicular electric field. The energy gaps of even (odd) number of layers are denoted by red (blue) circles. (b) The lowest total energy states in the presence of electric field. Flavor antiferro, ferri, and ferro states are colored in blue, red, and gray, respectively. The pseudospin polarization directions are written in increasing effective mass order.

due to the increased number of pseudospin doublets and their interactions. Here, we intend to provide a qualitative picture of the electronic structure expected in Bernal stacked multilayer graphene in the presence of electron-electron interactions and perpendicular external electric fields using a minimal continuum model for the band Hamiltonian.

In Bernal stacked multilayer graphene, the low-energy effective theory is described by a set of bilayer-like doublets for even-number of layers, while an additional monolayer-like doublet is found for odd-number of layers. The major difference in the energy gap between even- and odd-layer graphenes originates from the existence of the monolayer-like doublet in odd layered multilayers [3, 148–150]. Unlike bilayer-like doublets, monolayer-like doublets are much more robust to the interaction-induced sublattice symmetry breaking and tend to remain gapless [128], thus the gaps of odd-layer graphenes are much smaller than those of even-layer graphenes.

In Fig. 4.6 (a), we show the energy band gap as a function of the number of layers in the absence of electric field. For even number of layers the energy gap opens due to interactions and decreases as the number of layers increases, whereas for odd number of layers the energy gap almost remains closed. Note that the energy gap for odd number of layers is not exactly zero (except for a single layer) and the energy gap for both odd and even layers saturate as the number of layers increases. It is important to note that these remnant gaps are due to simplification in the minimal model and expected to be closed when remote hopping terms and screening are considered.

Restricting our attention to even-layer graphene, we summarize in Fig. 4.6 (b) the effect of a perpendicular electric field in the ground-state configurations. In general, the lowest total energy state varies from a flavor antiferro state with zero net charge polarization via a partially polarized state, and eventually to fully polarized flavor ferro state. Interestingly, for an appropriate external electric field range, the flavor ferri state (or "All" state [131–133]), which exhibits non-zero Hall conductivities of all flavors can be achieved not only in rhombohedral but also in Bernal stacked multilayer graphene. Since the total energies are almost degenerate, we expect that domains of different pseudospin configurations will form in a disordered sample [151]. Considering the large number of pseudospin flavors in tetralayers and beyond, it is also expected that a large variety of topological domain walls will arise at the interface between the ordered pseudospin domains.

4.6 Discussion

We identified the structure of the electron-electron interaction driven ordered phases in Bernal stacked multilayer graphene based on the polarization of the pseudospin doublets belonging to electronic bands with distinct effective masses. Our analysis rests on a number of simplifying assumptions such as: neglect of remote hopping terms and the energy difference between the dimer and non-dimer sites Δ, and the absence of screening and correlations in our interaction model. In our minimal model for the band Hamiltonian, only the nearest intralayer and interlayer hopping is considered for simplicity in order to conserve the rotational symmetry of the Hamiltonian. As the number of layers becomes larger, however, the remote hopping terms cannot be omitted for an accurate description of the band structure. Each remote hopping term plays a different role in multilayer graphene, but in general, it distorts the chiral character of the low energy band near the K or K' point reducing the density of states near the Fermi energy. Since the energy gap originates from the interplay of chirality and electron-electron interaction, the energy gap is expected to become smaller when the remote hopping terms are considered. Once the energy gap is closed or becomes narrower, the screening effect due to the Coulomb interaction begins to play a significant role, in a particularly notable manner for odd-layer graphenes.

For even-layer graphenes, larger interaction induced gaps open. When the gap size sets the dominant energy scale relative to the remote hopping energies, the basic picture presented in this paper should be valid at least qualitatively. It has been proposed that the electron-electron interactions will induce strains that suppress the remote interlayer coupling terms such as the γ_2 hopping [142]. The assumption of weakened remote hopping terms in few layer systems would make the minimal model an adequate ground for the analysis of interaction effects. In Appendix B.2, we investigated how the remote hopping term γ_2 modifies the ground state of the minimal model fro the ABAB graphene. We found that for a reasonable range of interaction strength and weakened γ_2, the ground states does not deviate from the minimal model qualitatively. As the number of layers increases towards the graphite limit, however, it is expected that the energy gap should show a progressive decrease until it eventually closes.

In summary, we provide a simple and comprehensive picture for the interaction induced ordered states in Bernal stacked multilayer graphene. We analyze the ground-state configurations and associated Hall conductivities that can result from the combined presence of electron-electron interactions and perpendicular external fields that could serve as guidance to future experiments.

Chapter 5

Conclusion

In this dissertation, we discussed two van der Waals materials $\mathrm{Bi}_4\mathrm{X}_4$ (X=Br, I) family and Bernal stacked multilayer graphene, focusing on their topological properties. As a summary and conclusion, we briefly review the important results in each system.

In Chap. 3, we provided a single framework to understand various topological phases found in $\mathrm{Bi}_4\mathrm{X}_4$ family. Starting from the careful analysis of the crystal structures, we constructed the effective TB models for each material of $\mathrm{Bi}_4\mathrm{X}_4$ and verified that our TB models not only reproduces the band structures but also the bulk band topology. We also investigated the (001) film systems of α-$\mathrm{Bi}_4\mathrm{X}_4$ and discovered the intriguing stacking-dependent hinge state patterns which cannot be understood from the 3D bulk band structures alone. Then we found that the non-trivial topology can be captured from the boundary Hamiltonian which has an analogy with the SSH model. We finally introduced three experimental collaborations which strongly support our theoretical predictions.

In Chap. 4, we analyze the ordered phases of Bernal stacked multilayer graphene in the presence of interaction. We find the interaction-driven ground states exhibit band gaps due to sublattice symmetry breaking, whose solutions can be analyzed in terms of light-mass and heavy-mass pseudospin doublets which have the same Chern numbers but opposite charge polarization directions. We also applied a perpendicular external electric field and find various topological ground state phases with different spin, valley, spin-valley, and/or charge quantum Hall coefficients.

Even though there have been so many amazing discoveries in topological van der Waals materials both theoretically and experimentally, we are still in the early phases of this field. From the aspects of the experiment, the progress in the fabrication of the high-quality samples now leads us to the unexpected physics. Good examples would be the discovery of the superconductivity in rhombohedral trilayer graphene and the twisted bilayer graphene. Besides experiments, there is still a long way to go in terms of theory. Though various topological phases have been extensively studied in the last two decades, most of the researches have been limited to the non-interacting single particle physics. I strongly believe that the interplay between geometry, symmetry, topology, and interaction will lead us to even more exciting new discoveries.

Appendix A

Topological phases in quasi-one-dimensional bismuth halides Bi_4X_4 (X = I, Br)

A.1 Crystal structure data

Table A.1 summarizes the crystal structure data of β-Bi_4Br_4, β-Bi_4I_4, α-Bi_4Br_4, and α-Bi_4I_4.

A.2 Model fitting

Table A.2 summarizes a set of parameter values for the Bi_4X_4 models in Sec. 3.4 that can well fit the band inversions and band structures of the MLWF data, as shown in Fig. 3.4. Below we describe our fitting procedure.

We first fit the intra-layer terms in H^L of Eq. (3.2) to the (001) monolayer Hamiltonians derived from the MLWF Hamiltonians by ignoring the inter-layer tunnelings. Informed by the bottom panels of Fig. 3.2, H^L has a band inversion at (π, π). Those terms even in momentum are fixed by the band energies at the TRI momenta, and those odd are determined by the band dispersions near (π, π). For the α phases, those terms $\propto \tau_z$ are identified by the differences between the even and odd (001) layers, e.g., the direct

Table A.1: Crystal structure data of Bi_4X_4. For α-Bi_4I_4, the second line gives the values of the angle θ_2' and the distance Bi_{in}'-Bi_{ex}'. For α-Bi_4Br_4, the two lines list the parameter values of the two symmetry unrelated (001) layers, respectively. Note that $\alpha = \gamma = 90°$ and that conventional unit cells are used.

Phase	a (Å)	b (Å)	c (Å)	β (°)	θ_1 (°)	θ_2 (°)	Bi_{in}-Bi_{in}' (Å)	Bi_{in}-Bi_{ex} (Å)
β-Bi_4Br_4	13.307	4.338	10.191	107.87	91.12	91.62	3.038	3.063
α-Bi_4Br_4	13.064	4.338	20.061	107.42	91.34	91.28	3.032	3.056
					91.51	93.07	3.028	3.052
α-Bi_4I_4	14.245	4.428	19.968	87.04[a]	93.49	92.80	3.040	3.057
						92.39		3.044
β-Bi_4I_4	14.386	4.430	10.493	107.87	93.18	92.42	3.049	3.071

---

[a] Note that β can be either $87.04°$ or $92.96°$ for α-Bi_4I_4, and that conventionally the obtuse angle is chosen. Here we choose $\beta = 87.04°$ instead for the consistency with the coordinates of the other three materials.

band gaps of $\mathrm{Bi_4Br_4}$ and the Dirac point energies of $\mathrm{Bi_4I_4}$. On top of these, we then fit the inter-layer tunnelings in Eqs. (3.2), (3.7), and (3.8) with the band inversions and band energies at the L and M points.

Table A.2: A set of parameter values in units of meV for the $\mathrm{Bi_4X_4}$ models in Sec. 3.4 that can well fit the band inversions and band structures given by the MLWF data.

Parameter	β-$\mathrm{Bi_4Br_4}$	α-$\mathrm{Bi_4Br_4}$	α-$\mathrm{Bi_4I_4}$	β-$\mathrm{Bi_4I_4}$
t_a	146.15	181.67	119.73	119.73
t_b	977.13	977.62	1075.40	1075.40
d_0	89.43	92.37	114.66	128.44
d_a	20.14	15.85	44.59	47.71
d_b	−57.50	−70.19	−19.94	−9.10
m_0	955.08	922.99	788.19	804.44
m_a	140.61	161.04	121.65	110.85
m_b	−701.98	−714.37	−589.67	−594.71
t_c	19.49	12.06	39.48	20.50
d_c	4.17	−6.62	−2.09	−11.95
m_c	−1.99	−12.96	−24.46	−21.64
d'_0		−12.00		
m'_0		21.31		
t			7.78	
t'			7.78	
t'_c		−10.33	−6.85	
d'_c		−6.62	−5.66	
m'_c		−12.96	2.47	

A.3 More accurate α-$\mathrm{Bi_4I_4}$ model

The fact that the inversion center of α-$\mathrm{Bi_4I_4}$ can only be placed in the middle of two adjacent (001) layers has two consequences. First, the inter-unit-cell layer separation is slightly different than the intra-unit-cell one, as

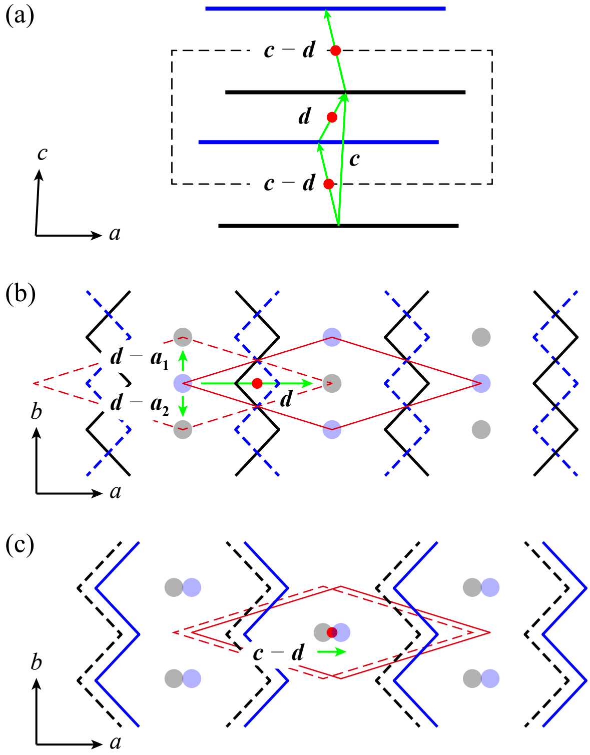

Figure A.1: (a) Stacking registry of α-Bi$_4$I$_4$. The dashed boxes are the primitive unit cells. The red dots are the inversion centers. (b) and (c) are two adjacent layers in the same and different unit cells, respectively, viewed from the $\boldsymbol{c}-\boldsymbol{a}/2$ axis. The zigzag lines sketch the atomic chains. The solid and dashed lines denote the upper and lower layers. The blue and gray dots are the centers of the unit cells of individual layers. $\boldsymbol{d}$, $\boldsymbol{d}-\boldsymbol{a}_1$, $\boldsymbol{d}-\boldsymbol{a}_2$, and $\boldsymbol{c}-\boldsymbol{d}$ connect the centers of two adjacent layers. The green arrows are vectors connecting different inter-layer NNs. Based on Table A.1, the layer spacing is nearly uniform, and $\boldsymbol{d}$ is close to $\boldsymbol{c}/2+\boldsymbol{a}/4$; the spacing variation in (a) and the layer mismatch in (c) are exaggerated.

sketched in Fig. A.1(a). Second, within the $\boldsymbol{a}$-$\boldsymbol{b}$ plane, two adjacent layers in the same unit cell are shifted by $\boldsymbol{a}/2$ relatively, while two in different unit cells remain little shifted, as sketched in Figs. A.1(b) and A.1(c). In the model in Eq. (3.8), while the first effect has been counted, the second effect is ignored for simplicity. Because of the second effect, the NN interlayer hopping processes within a unit cell are associated with the lattice vectors $\pm(\boldsymbol{d}-\boldsymbol{a}_1)$ and $\pm(\boldsymbol{d}-\boldsymbol{a}_2)$ instead of $\pm\boldsymbol{d}$, as shown in Fig. A.1(b). To take into account the second effect, in the model in Eq. (3.8), the factor τ_x in the term $(d_c+m_c\sigma_z)\tau_x$ needs to be replaced by

$$-\frac{1}{2}[\tau_x(\cos k_1+\cos k_2)+\tau_y(\sin k_1+\sin k_2)], \tag{A.1}$$

and the factor τ_y in the term $t_c\sigma_x s_y\tau_y$ needs to be replaced by

$$-\frac{1}{2}[\tau_y(\cos k_1+\cos k_2)-\tau_x(\sin k_1+\sin k_2)]. \tag{A.2}$$

In the ML line, $k_1=k_2=\pi$, these two factors reduce to τ_x and τ_y, and the model in Eq. (3.8) is recovered.

A.4 Extended winding number

The celebrated SSH model can be expressed as

$$H(q)=\begin{pmatrix} 0 & t_1+t_2e^{-iq} \\ t_1^*+t_2^*e^{iq} & 0 \end{pmatrix}, \tag{A.3}$$

where t_1 and t_2 are the NN couplings within a unit cell and between two unit cells, respectively. Because of its chiral symmetry, $H(q)$ is characterized by

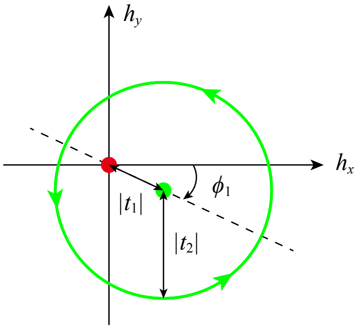

Figure A.2: The trajectory of $(h_x(q), h_y(q))$ in Eq. (A.5).

the first winding number (evaluated in the trivial gauge [105])

$$\nu_1 = \frac{i}{2\pi}\int_{\mathrm{BZ}} dq h(q)^\dagger \partial_q h(q) = \Theta\left(|t_2| - |t_1|\right), \tag{A.4}$$

where $h(q) = (t_1 + t_2 e^{-iq})/|\epsilon(q)|$, $\pm\epsilon(q)$ are eigenvalues of $H(q)$, and Θ is the Heaviside function. Although the winding numbers are not gauge invariant, their differences are gauge invariant (when evaluated in the same gauge). Thus, there are N topological zero modes localized at any boundary across which ν_1 changes by N.

In most cases t_1 and t_2 are assumed to be real, yet in general they can be extended to complex numbers and the conclusion Eq. (A.4) remains the same. To show this explicitly, let $t_1 = |t_1|e^{i\phi_1}$ and $t_2 = |t_2|e^{i\phi_2}$ with

$0 \le \phi_1, \phi_2 < 2\pi$ in Eq. (A.3), and we obtain

$$\begin{aligned} H(q) &= h_x(q)\sigma_x + h_y(q)\sigma_y, \\ h_x(q) &= |t_2| \cos(q - \phi_2) + |t_1| \cos\phi_1, \\ h_y(q) &= |t_2| \sin(q - \phi_2) - |t_1| \sin\phi_1, \end{aligned} \tag{A.5}$$

where $\boldsymbol{\sigma}$ are Pauli matrices. One can directly see from Eq. (A.5) that The trajectory of $(h_x(q), h_y(q))$ is a circle of radius $|t_2|$ centered at $(|t_1|\cos\phi_1, -|t_1|\sin\phi_1)$, as shown in Fig. A.2. Thus, the criterion for the origin being enclosed by the trajectory, i.e., $\nu_1 = 1$, remains the same as $|t_1| < |t_2|$ even for complex t_1 and t_2.

A.5 Density of states of finite-sized α-Bi$_4$X$_4$

In contrast to the most of (perhaps all the other) HOTI candidates, α-Bi$_4$X$_4$ exhibit not only a finite global bulk gap, but also a finite global surface gap, where the case of α-Bi$_4$I$_4$ is shown in Fig. A.3(a) as an example. As a result, the hinge, surface, and bulk contribution to the DOS are clearly distinguished as depicted in Fig. A.3(b). Here, note that all the hinge, surface, and bulk bands have nearly constant DOS, which is due to the quasi-1D nature of α-Bi$_4$X$_4$. Although the surface and the bulk bands are the 2D and 3D bands, respectively, the bands are much more dispersive along the $\boldsymbol{b}$ direction than the other two directions, so that the DOS of the system exhibit approximately 1D-like power law.

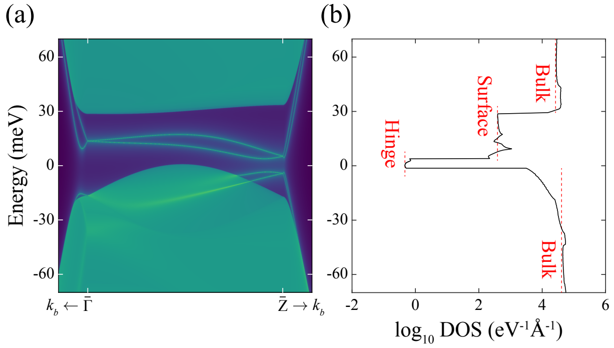

(c) α-Bi$_4$Br$_4$

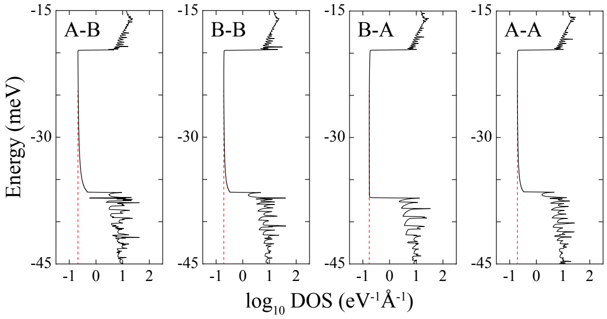

(d) α-Bi$_4$I$_4$

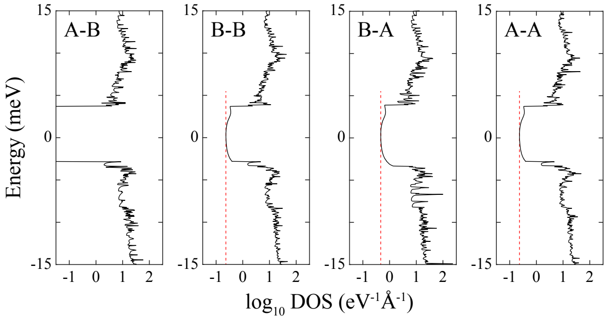

Figure A.3: (a) (201) surface states of α-Bi$_4$I$_4$. The zero energy is set at the 0 meV in Fig. 3.2(c). (b) The DOS of α-Bi$_4$I$_4$ rod which is periodic in the $\boldsymbol{b}$ direction, 1000-unit-cell long in the $\boldsymbol{a}$ and $\boldsymbol{c}$ direction. (c), (d) The DOS of α-Bi$_4$Br$_4$ and α-Bi$_4$I$_4$ near the surface gap. The systems in Figs. 3.6 and 3.8 are used here.

In the surface gap, one can measure the DOS of the 1D helical hinge states, where each Kramer pair of hinge states contributes a constant $1/\pi\hbar v_F$

to the DOS. In the case of α-Bi_4Br_4, the number of helical hinge modes are independent of the (001) termination, as shown in Fig. 3.6. As a result, the DOS in the surface gap are nearly the same for all the types of (001) terminations, which are shown in Fig. A.3(c). However, as one can verify from Fig. 3.8, the number of hinge states depends on the (001) termination in α-Bi_4I_4 and thus the DOS in the surface gap also varies with the (001) terminations in Fig. A.3(d). This clear difference can be used to distinguish the bulk- and boundary-obstructed phases in quasi-1D TIs.

Appendix B

Broken sublattice symmetry states in Bernal stacked multilayer graphene

B.1 Ground-state configurations for 6-layer graphene

Similarly as tetralayer graphene, the low-energy band structure of Bernal stacked 6-layer graphene (ABABAB) at low energies is described by three bilayer-like pseudospin doublets with different masses. Because of the sublattice symmetry breaking, charge polarizations of the three pseudospins have alternating directions, $(\downarrow, \uparrow, \downarrow)$ or $(\uparrow, \downarrow, \uparrow)$ where arrows in the parenthesis represent the charge polarization of pseudospins with increasing effective mass order. The corresponding Chern numbers are (+1,+1,+1) or (−1,−1,−1) because of the same sign of sublattice potential generated by the sublattice symmetry breaking. Similarly, we can understand the ground-state configurations of 8-layer graphene (ABABABAB) as $(\downarrow, \uparrow, \downarrow, \uparrow)$ or $(\uparrow, \downarrow, \uparrow, \downarrow)$ with the Chern numbers (+1,+1,+1,+1) or (−1,−1,−1,−1) at zero field.

Table B.1 shows the external field dependence of the ground-state configurations in the LAF state for 6-layer graphene. In Tab. B.2, the corresponding Hall conductivities are calculated for the three possible anti-

Table B.1: Charge polarizations and corresponding Chern numbers in the presence of a perpendicular electric field in Bernal stacked 6-layer graphene for the LAF state. The pseudospins are written in increasing effective mass order from the left to the right. Here, $E_{\text{c1}}^{(6)} = 0.017$, $E_{\text{c2}}^{(6)} = 0.251$, and $E_{\text{c3}}^{(6)} = 0.281$ meV/Å. Red arrows indicate flipped pseudospin polarizations with field.

E	Flavor I $(K_{\text{u}}, K'_{\text{u}})$			Flavor II $(K_{\text{d}}, K'_{\text{d}})$			Chern Number			
							K_{u}	K_{d}	K'_{u}	K'_{d}
$E_{c3}^{(6)}$	↑	↑	↑	↑	↑	↑	1	1	-1	-1
$E_{c2}^{(6)}$	↑	↑	↑	↑	↑	↓	1	-1	-1	1
$E_{c1}^{(6)}$	↑	↓	↑	↑	↑	↓	3	-1	-3	1
0	↑	↓	↑	↓	↑	↓	3	-3	-3	3
$-E_{c1}^{(6)}$	↓	↓	↑	↓	↑	↓	1	-3	-1	3
$-E_{c2}^{(6)}$	↓	↓	↑	↓	↓	↓	1	-1	-1	1
$-E_{c3}^{(6)}$	↓	↓	↓	↓	↓	↓	-1	-1	1	1

ferro states, respectively. When the external electric field E_{ext} is zero, pseudospins with increasing effective mass have alternating charge polarization directions for 6-layer graphene, which is consistent with the tetralayer case. As E_{ext} increases, each pseudospin flips from the one with lighter effective mass following the Hund's rule. As the number of layers increases, however, there are deviations from this rule in the intermediate field region resulting from the greater complexity of the intermediate states and the interaction between the bands near the Fermi energy.

B.2 Effect of the remote hopping terms

In even-layer graphenes, the energy gap is the dominant energy scale, thus when the gap is large enough, the effect of other energy scales asso-

Table B.2: Spontaneous quantum Hall conductivities in units of e^2/h for the antiferro states in Bernal stacked 6-layer graphene under a perpendicular external electric field.

E_{ext}	LAF				QSH				QAH			
	SH	VH	CH	SV	SH	VH	CH	SV	SH	VH	CH	SV
$E_{\mathrm{c3}}^{(6)}$	0	4	0	0	0	4	0	0	0	4	0	0
$E_{\mathrm{c2}}^{(6)}$	0	0	0	4	4	0	0	0	0	0	4	0
$E_{\mathrm{c1}}^{(6)}$	0	4	0	8	8	4	0	0	0	4	8	0
0	0	0	0	12	12	0	0	0	0	0	12	0
$-E_{\mathrm{c1}}^{(6)}$	0	-4	0	8	8	-4	0	0	0	-4	8	0
$-E_{\mathrm{c2}}^{(6)}$	0	0	0	4	4	0	0	0	0	0	4	0
$-E_{\mathrm{c3}}^{(6)}$	0	-4	0	0	0	-4	0	0	0	-4	0	0

ciated with remote hopping terms could be neglibible and the basic picture presented in this paper remains valid at least qualitatively. However, when the remote hopping terms are not negligible compared to the energy gap, the ground state is no longer described by the sublattice symmetry breaking and the effective Hund's rule, and the detailed ground state configurations will be determined by combined effects of the remote hopping terms and screening. Figure B.1 shows the phase diagram between the gap dominant and remote-hopping dominant regions as a function of the interaction strength α and the next-nearest interlayer coupling between non-dimer sites γ_2, neglecting other remote hopping terms for simplicity, in tetralayer graphene. Here, the gap (remote-hopping) dominant region represent a region where the ground state is (not) described by the sublattice symmetry breaking and the effective Hund's rule. As expected, broken sublattice symmetry occurs at large α and small size of γ_2. It has been proposed that the remote hopping terms in multilayer graphene could be different from those in graphite and suppressed by interaction induced strains [142], justifying the use of the minimal model. Considering that $\alpha \sim 1$ for conventional SiO_2 substrates and $\alpha \sim 2.6$ for suspended samples, we expect that the remote hopping terms do not change the basic picture drawn from the minimal model.

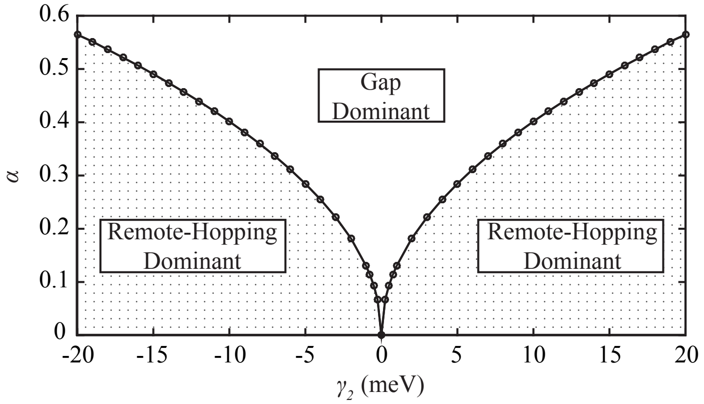

Figure B.1: The phase diagram for the ground state configuration of tetralayer graphene on α and γ_2 plane. Here, the gap (remote-hopping) dominant region denotes a region where the ground state is (not) described by the sublattice symmetry breaking and the effective Hund's rule.

Bibliography

[1] K. S. Novoselov, A. K. Geim, S. V. Morozov, D. Jiang, Y. Zhang, S. V. Dubonos, I. V. Grigorieva, and A. A. Firsov, Science **306**, 666–669 (2004).

[2] A. H. Castro Neto, F. Guinea, N. M. R. Peres, K. S. Novoselov, and A. K. Geim, Rev. Mod. Phys. **81**, 109–162 (2009).

[3] H. Min and A. H. MacDonald, Phys. Rev. B **77**, 155416 (2008).

[4] A. K. Geim and I. V. Grigorieva, Nature **499**, 419–425 (2013).

[5] Y. Cao, V. Fatemi, S. Fang, K. Watanabe, T. Taniguchi, E. Kaxiras, and P. Jarillo-Herrero, Nature **556**, 43–50 (2018).

[6] Y. Cao, V. Fatemi, A. Demir, S. Fang, S. L. Tomarken, J. Y. Luo, J. D. Sanchez-Yamagishi, K. Watanabe, T. Taniguchi, E. Kaxiras, R. C. Ashoori, and P. Jarillo-Herrero, Nature **556**, 80–84 (2018).

[7] R. Bistritzer and A. H. MacDonald, Proceedings of the National Academy of Sciences **108**, 12233–12237 (2011).

[8] C. L. Kane and E. J. Mele, Phys. Rev. Lett. **95**, 146802 (2005).

[9] C. L. Kane and E. J. Mele, Phys. Rev. Lett. **95**, 226801 (2005).

[10] B. A. Bernevig, T. L. Hughes, and S.-C. Zhang, Science **314**, 1757–1761 (2006).

[11] M. König, S. Wiedmann, C. Brüne, A. Roth, H. Buhmann, L. W. Molenkamp, X.-L. Qi, and S.-C. Zhang, Science **318**, 766–770 (2007).

[12] D. Hsieh, Y. Xia, D. Qian, L. Wray, J. H. Dil, F. Meier, J. Osterwalder, L. Patthey, J. G. Checkelsky, N. P. Ong, A. V. Fedorov, H. Lin,

A. Bansil, D. Grauer, Y. S. Hor, R. J. Cava, and M. Z. Hasan, Nature **460**, 1101–1105 (2009).

[13] M. Z. Hasan and C. L. Kane, Rev. Mod. Phys. **82**, 3045–3067 (2010).

[14] F. D. M. Haldane, Phys. Rev. Lett. **61**, 2015–2018 (1988).

[15] L. Fu and C. L. Kane, Phys. Rev. B **76**, 045302 (2007).

[16] J. E. Moore and L. Balents, Phys. Rev. B **75**, 121306 (2007).

[17] R. Roy, Phys. Rev. B **79**, 195322 (2009).

[18] H. Min, J. E. Hill, N. A. Sinitsyn, B. R. Sahu, L. Kleinman, and A. H. MacDonald, Phys. Rev. B **74**, 165310 (2006).

[19] H. Zhang, C.-X. Liu, X.-L. Qi, X. Dai, Z. Fang, and S.-C. Zhang, Nat. Phys. **5**, 438–442 (2009).

[20] M. G. Vergniory, B. J. Wieder, L. Elcoro, S. S. P. Parkin, C. Felser, B. A. Bernevig, and N. Regnault, Science **376**, eabg9094 (2022), https://www.science.org/doi/pdf/10.1126/science.abg9094 .

[21] J. C. Y. Teo, L. Fu, and C. L. Kane, Phys. Rev. B **78**, 045426 (2008).

[22] L. Fu, Phys. Rev. Lett. **106**, 106802 (2011).

[23] J. Liu, T. H. Hsieh, P. Wei, W. Duan, J. Moodera, and L. Fu, Nat. Mater. **13**, 178–183 (2014).

[24] L. Fu and C. L. Kane, Phys. Rev. B **74**, 195312 (2006).

[25] R. Yu, X. L. Qi, A. Bernevig, Z. Fang, and X. Dai, Phys. Rev. B **84**, 075119 (2011).

[26] J. Kruthoff, J. de Boer, J. van Wezel, C. L. Kane, and R.-J. Slager, Phys. Rev. X **7**, 041069 (2017).

[27] H. C. Po, A. Vishwanath, and H. Watanabe, Nat. Commun. **8**, 50 (2017).

[28] B. Bradlyn, L. Elcoro, J. Cano, M. G. Vergniory, Z. Wang, C. Felser, M. I. Aroyo, and B. A. Bernevig, Nature **547**, 298–305 (2017).

[29] T. Zhang, Y. Jiang, Z. Song, H. Huang, Y. He, Z. Fang, H. Weng, and C. Fang, Nature **566**, 475–479 (2019).

[30] M. G. Vergniory, L. Elcoro, C. Felser, N. Regnault, B. A. Bernevig, and Z. Wang, Nature **566**, 480–485 (2019).

[31] F. Tang, H. C. Po, A. Vishwanath, and X. Wan, Nature **566**, 486–489 (2019).

[32] X.-L. Qi, T. L. Hughes, and S.-C. Zhang, Phys. Rev. B **78**, 195424 (2008).

[33] F. Zhang, C. L. Kane, and E. J. Mele, Phys. Rev. Lett. **110**, 046404 (2013).

[34] W. A. Benalcazar, B. A. Bernevig, and T. L. Hughes, Science **357**, 61–66 (2017).

[35] F. Schindler, A. M. Cook, M. G. Vergniory, Z. Wang, S. S. P. Parkin, B. A. Bernevig, and T. Neupert, Sci. Adv. **4**, eaat0346 (2018).

[36] J. Langbehn, Y. Peng, L. Trifunovic, F. von Oppen, and P. W. Brouwer, Phys. Rev. Lett. **119**, 246401 (2017).

[37] Z. Song, Z. Fang, and C. Fang, Phys. Rev. Lett. **119**, 246402 (2017).

[38] M. Ezawa, Phys. Rev. Lett. **120**, 026801 (2018).

[39] F. Schindler, Z. Wang, M. G. Vergniory, A. M. Cook, A. Murani, S. Sengupta, A. Y. Kasumov, R. Deblock, S. Jeon, I. Drozdov, H. Bouchiat, S. Guéron, A. Yazdani, B. A. Bernevig, and T. Neupert, Nat. Phys. **14**, 918–924 (2018).

[40] E. Khalaf, Phys. Rev. B **97**, 205136 (2018).

[41] Q. Wang, C.-C. Liu, Y.-M. Lu, and F. Zhang, Phys. Rev. Lett. **121**, 186801 (2018).

[42] Z. Yan, F. Song, and Z. Wang, Phys. Rev. Lett. **121**, 096803 (2018).

[43] Z. Wang, B. J. Wieder, J. Li, B. Yan, and B. A. Bernevig, Phys. Rev. Lett. **123**, 186401 (2019).

[44] R. Noguchi, M. Kobayashi, Z. Jiang, K. Kuroda, T. Takahashi, Z. Xu, D. Lee, M. Hirayama, M. Ochi, T. Shirasawa, P. Zhang, C. Lin, C. Bareille, S. Sakuragi, H. Tanaka, S. Kunisada, K. Kurokawa, K. Yaji, A. Harasawa, V. Kandyba, A. Giampietri, A. Barinov, T. K. Kim, C. Cacho, M. Hashimoto, D. Lu, S. Shin, R. Arita, K. Lai, T. Sasagawa, and T. Kondo, Nat. Mater. **20**, 473–479 (2021).

[45] N. Shumiya, M. S. Hossain, J.-X. Yin, Z. Wang, M. Litskevich, C. Yoon, Y. Li, Y. Yang, Y.-X. Jiang, G. Cheng, Y.-C. Lin, Q. Zhang, Z.-J. Cheng, T. A. Cochran, D. Multer, X. P. Yang, B. Casas, T.-R. Chang, T. Neupert, Z. Yuan, S. Jia, H. Lin, N. Yao, L. Balicas, F. Zhang, Y. Yao, and M. Z. Hasan, Nat. Mater. , DOI:10.1038/s41563–022–01304–3 (2022).

[46] C.-X. Liu, X.-L. Qi, H. Zhang, X. Dai, Z. Fang, and S.-C. Zhang, Phys. Rev. B **82**, 045122 (2010).

[47] F. Zhang, C. L. Kane, and E. J. Mele, Phys. Rev. B **86**, 081303 (2012).

[48] M. P. L. Sancho, J. M. L. Sancho, and J. Rubio, J. Phys. F: Met. Phys. **14**, 1205–1215 (1984).

[49] M. P. L. Sancho, J. M. L. Sancho, and J. Rubio, J. Phys. F: Met. Phys. **15**, 851–858 (1985).

[50] L. Fu, C. L. Kane, and E. J. Mele, Phys. Rev. Lett. **98**, 106803 (2007).

[51] X.-L. Qi and S.-C. Zhang, Rev. Mod. Phys. **83**, 1057–1110 (2011).

[52] C.-K. Chiu, J. C. Y. Teo, A. P. Schnyder, and S. Ryu, Rev. Mod. Phys. **88**, 035005 (2016).

[53] N. P. Armitage, E. J. Mele, and A. Vishwanath, Rev. Mod. Phys. **90**, 015001 (2018).

[54] F. Zhang, Nat. Phys. **14**, 111–113 (2018).

[55] L. Lu, J. D. Joannopoulos, and M. Soljačić, Nat. Phys. **12**, 626–629 (2016).

[56] J. Lu, C. Qiu, L. Ye, X. Fan, M. Ke, F. Zhang, and Z. Liu, Nat. Phys. **13**, 369–374 (2017).

[57] S. D. Huber, Nat. Phys. **12**, 621–623 (2016).

[58] P. Delplace, J. B. Marston, and A. Venaille, Science **358**, 1075–1077 (2017).

[59] C. Yue, Y. Xu, Z. Song, H. Weng, Y.-M. Lu, C. Fang, and X. Dai, Nat. Phys. **15**, 577–581 (2019).

[60] R.-X. Zhang, F. Wu, and S. Das Sarma, Phys. Rev. Lett. **124**, 136407 (2020).

[61] R. Yu, W. Zhang, H.-J. Zhang, S.-C. Zhang, X. Dai, and Z. Fang, Science **329**, 61–64 (2010).

[62] C.-Z. Chang, J. Zhang, X. Feng, J. Shen, Z. Zhang, M. Guo, K. Li, Y. Ou, P. Wei, L.-L. Wang, Z.-Q. Ji, Y. Feng, S. Ji, X. Chen, J. Jia, X. Dai, Z. Fang, S.-C. Zhang, K. He, Y. Wang, L. Lu, X.-C. Ma, and Q.-K. Xue, Science **340**, 167–170 (2013).

[63] X. Wu, W. A. Benalcazar, Y. Li, R. Thomale, C.-X. Liu, and J. Hu, Phys. Rev. X **10**, 041014 (2020).

[64] R.-X. Zhang, W. S. Cole, and S. Das Sarma, Phys. Rev. Lett. **122**, 187001 (2019).

[65] M. J. Gray, J. Freudenstein, S. Y. F. Zhao, R. O'Connor, S. Jenkins, N. Kumar, M. Hoek, A. Kopec, S. Huh, T. Taniguchi, K. Watanabe,

R. Zhong, C. Kim, G. D. Gu, and K. S. Burch, Nano Lett. **19**, 4890–4896 (2019).

[66] C. W. Peterson, W. A. Benalcazar, T. L. Hughes, and G. Bahl, Nature **555**, 346–350 (2018).

[67] S. Imhof, C. Berger, F. Bayer, J. Brehm, L. W. Molenkamp, T. Kiessling, F. Schindler, C. H. Lee, M. Greiter, T. Neupert, and R. Thomale, Nat. Phys. **14**, 925–929 (2018).

[68] J. Noh, W. A. Benalcazar, S. Huang, M. J. Collins, K. P. Chen, T. L. Hughes, and M. C. Rechtsman, Nat. Photon. **12**, 408–415 (2018).

[69] S. Mittal, V. V. Orre, G. Zhu, M. A. Gorlach, A. Poddubny, and M. Hafezi, Nat. Photon. **13**, 692–696 (2019).

[70] M. Serra-Garcia, V. Peri, R. Süsstrunk, O. R. Bilal, T. Larsen, L. G. Villanueva, and S. D. Huber, Nature **555**, 342–345 (2018).

[71] H. Xue, Y. Yang, F. Gao, Y. Chong, and B. Zhang, Nat. Mater. **18**, 108–112 (2019).

[72] X. Ni, M. Weiner, A. Alù, and A. B. Khanikaev, Nat. Mater. **18**, 113–120 (2019).

[73] X. Zhang, H.-X. Wang, Z.-K. Lin, Y. Tian, B. Xie, M.-H. Lu, Y.-F. Chen, and J.-H. Jiang, Nat. Phys. **15**, 582–588 (2019).

[74] Y.-B. Choi, Y. Xie, C.-Z. Chen, J. Park, S.-B. Song, J. Yoon, B. J. Kim, T. Taniguchi, K. Watanabe, J. Kim, K. C. Fong, M. N. Ali, K. T. Law, and G.-H. Lee, Nat. Mater. **19**, 974–979 (2020).

[75] A. Kononov, G. Abulizi, K. Qu, J. Yan, D. Mandrus, K. Watanabe, T. Taniguchi, and C. Schönenberger, Nano Lett. **20**, 4228–4233 (2020).

[76] Z. Song, T. Zhang, Z. Fang, and C. Fang, Nat. Commun. **9**, 3530 (2018).

[77] E. Khalaf, H. C. Po, A. Vishwanath, and H. Watanabe, Phys. Rev. X **8**, 031070 (2018).

[78] M. Hellenbrandt, Crystallogr. Rev. **10**, 17–22 (2004).

[79] A. Zunger, Nature **566**, 447–449 (2019).

[80] F. Tang, H. C. Po, A. Vishwanath, and X. Wan, Nat. Phys. **15**, 470–476 (2019).

[81] C.-H. Hsu, X. Zhou, Q. Ma, N. Gedik, A. Bansil, V. M. Pereira, H. Lin, L. Fu, S.-Y. Xu, and T.-R. Chang, 2D Mater. **6**, 031004 (2019).

[82] H. G. von Schnering, H. von Benda, and C. Kalveram, Z. Anorg. Allg. Chem. **438**, 37–52 (1978).

[83] C.-C. Liu, J.-J. Zhou, Y. Yao, and F. Zhang, Phys. Rev. Lett. **116**, 066801 (2016).

[84] R. Noguchi, T. Takahashi, K. Kuroda, M. Ochi, T. Shirasawa, M. Sakano, C. Bareille, M. Nakayama, M. D. Watson, K. Yaji, A. Harasawa, H. Iwasawa, P. Dudin, T. K. Kim, M. Hoesch, V. Kandyba, A. Giampietri, A. Barinov, S. Shin, R. Arita, T. Sasagawa, and T. Kondo, Nature **566**, 518–522 (2019).

[85] A. Pisoni, R. Gaál, A. Zeugner, V. Falkowski, A. Isaeva, H. Huppertz, G. Autès, O. V. Yazyev, and L. Forró, Phys. Rev. B **95**, 235149 (2017).

[86] X. Wang, J. Wu, J. Wang, T. Chen, H. Gao, P. Lu, Q. Chen, C. Ding, J. Wen, and J. Sun, Phys. Rev. B **98**, 174112 (2018).

[87] Y. Qi, W. Shi, P. Werner, P. G. Naumov, W. Schnelle, L. Wang, K. G. Rana, S. Parkin, S. A. Medvedev, B. Yan, and C. Felser, npj Quantum Mater. **3**, 4 (2018).

[88] X. Li, D. Chen, M. Jin, D. Ma, Y. Ge, J. Sun, W. Guo, H. Sun, J. Han, W. Xiao, J. Duan, Q. Wang, C.-C. Liu, R. Zou, J. Cheng, C. Jin, J. Zhou, J. B. Goodenough, J. Zhu, and Y. Yao, Proc. Natl. Acad. Sci. U.S.A. **116**, 17696–17700 (2019).

[89] E. V. Dikarev, B. A. Popovkin, and A. V. Shevelkov, Russ. Chem. Bull. Int. Ed. **50**, 2304–2309 (2001).

[90] A. Weiz, M. L. Anh, M. Kaiser, B. Rasche, T. Herrmannsdörfer, T. Doert, and M. Ruck, Eur. J. Inorg. Chem. **2017**, 5609–5615 (2017).

[91] J. Huang, S. Li, C. Yoon, J. S. Oh, H. Wu, X. Liu, N. Dhale, Y.-F. Zhou, Y. Guo, Y. Zhang, M. Hashimoto, D. Lu, J. Denlinger, X. Wang, C. N. Lau, R. J. Birgeneau, F. Zhang, B. Lv, and M. Yi, Phys. Rev. X **11**, 031042 (2021).

[92] W. P. Su, J. R. Schrieffer, and A. J. Heeger, Phys. Rev. Lett. **42**, 1698–1701 (1979).

[93] C. Yoon, C.-C. Liu, H. Min, and F. Zhang, arXiv:2005.14710 .

[94] H. von Benda, A. Simon, and W. Bauhofer, Z. Anorg. Allg. Chem. **438**, 53–67 (1978).

[95] G. Autès, A. Isaeva, L. Moreschini, J. C. Johannsen, A. Pisoni, R. Mori, W. Zhang, T. G. Filatova, A. N. Kuznetsov, L. Forró, W. Van den Broek, Y. Kim, K. S. Kim, A. Lanzara, J. D. Denlinger, E. Rotenberg, A. Bostwick, M. Grioni, and O. V. Yazyev, Nat. Mater. **15**, 154–158 (2016).

[96] G. Kresse and J. Furthmüller, Phys. Rev. B **54**, 11169–11186 (1996).

[97] J. P. Perdew, K. Burke, and M. Ernzerhof, Phys. Rev. Lett. **77**, 3865–3868 (1996).

[98] G. Kresse and D. Joubert, Phys. Rev. B **59**, 1758–1775 (1999).

[99] J. Heyd, G. E. Scuseria, and M. Ernzerhof, J. Chem. Phys. **118**, 8207–8215 (2003).

[100] N. Marzari and D. Vanderbilt, Phys. Rev. B **56**, 12847–12865 (1997).

[101] I. Souza, N. Marzari, and D. Vanderbilt, Phys. Rev. B **65**, 035109 (2001).

[102] A. A. Mostofi, J. R. Yates, Y.-S. Lee, I. Souza, D. Vanderbilt, and N. Marzari, Comput. Phys. Commun. **178**, 685–699 (2008).

[103] J.-J. Zhou, W. Feng, C.-C. Liu, S. Guan, and Y. Yao, Nano Lett. **14**, 4767–4771 (2014).

[104] C. Fang and L. Fu, Sci. Adv. **5**, eaat2374 (2019).

[105] F. Zhang, C. L. Kane, and E. J. Mele, Phys. Rev. Lett. **111**, 056403 (2013).

[106] E. Khalaf, W. A. Benalcazar, T. L. Hughes, and R. Queiroz, Phys. Rev. Res. **3**, 013239 (2021).

[107] X.-L. Sheng, C. Chen, H. Liu, Z. Chen, Z.-M. Yu, Y. X. Zhao, and S. A. Yang, Phys. Rev. Lett. **123**, 256402 (2019).

[108] Y. Liu, R. Chen, Z. Zhang, M. Bockrath, C. N. Lau, Y.-F. Zhou, C. Yoon, S. Li, X. Liu, N. Dhale, B. Lv, F. Zhang, K. Watanabe, T. Taniguchi, J. Huang, M. Yi, J. S. Oh, and R. J. Birgeneau, Nano Lett. **22**, 1151–1158 (2022).

[109] B. L. Altshuler and A. G. Aronov, *Electron–electron interaction in disordered conductors,* in *Electron–electron interaction in disordered systems*, Modern Problems in Condensed Matter Sciences, Vol. 10, edited by A. Efros and M. Pollak (Elsevier, 1985) pp. 1–153.

[110] P. Gehring, K. Vaklinova, A. Hoyer, H. M. Benia, V. Skakalova, G. Argentero, F. Eder, J. C. Meyer, M. Burghard, and K. Kern, Sci. Rep. **5**, 11691 (2015).

[111] R. Stühler, F. Reis, T. Müller, T. Helbig, T. Schwemmer, R. Thomale, J. Schäfer, and R. Claessen, Nat. Phys. **16**, 47–51 (2020).

[112] V. V. Deshpande, M. Bockrath, L. I. Glazman, and A. Yacoby, Nature **464**, 209–216 (2010).

[113] T. Li, P. Wang, H. Fu, L. Du, K. A. Schreiber, X. Mu, X. Liu, G. Sullivan, G. A. Csáthy, X. Lin, and R.-R. Du, Phys. Rev. Lett. **115**, 136804 (2015).

[114] W. Wang, S. Kim, M. Liu, F. A. Cevallos, R. J. Cava, and N. P. Ong, Science **368**, 534–537 (2020).

[115] M. Geier, L. Trifunovic, M. Hoskam, and P. W. Brouwer, Phys. Rev. B **97**, 205135 (2018).

[116] T. H. Hsieh, H. Lin, J. Liu, W. Duan, A. Bansil, and L. Fu, Nat. Commun. **3**, 982 (2012).

[117] H. Nielsen and M. Ninomiya, Nucl. Phys. B **185**, 20–40 (1981).

[118] S. Das Sarma, S. Adam, E. H. Hwang, and E. Rossi, Rev. Mod. Phys. **83**, 407–470 (2011).

[119] D. N. Basov, M. M. Fogler, A. Lanzara, F. Wang, and Y. Zhang, Rev. Mod. Phys. **86**, 959–994 (2014).

[120] H. Raza, ed., *Graphene Nanoelectronics* (Springer, 2012).

[121] H. Ji, X. Zhao, Z. Qiao, J. Jung, Y. Zhu, Y. Lu, L. L. Zhang, A. H. MacDonald, and R. S. Ruoff, Nat. Commun. **5**, 3317 (2014).

[122] R. T. Weitz, M. T. Allen, B. E. Feldman, J. Martin, and A. Yacoby, Science **330**, 812–816 (2010).

[123] B. E. Feldman, J. Martin, and A. Yacoby, Nat. Phys. **5**, 889–893 (2009).

[124] A. S. Mayorov, D. C. Elias, M. Mucha-Kruczynski, R. V. Gorbachev, T. Tudorovskiy, A. Zhukov, S. V. Morozov, M. I. Katsnelson, null null, A. K. Geim, and K. S. Novoselov, Science **333**, 860–863 (2011).

[125] J. Velasco, L. Jing, W. Bao, Y. Lee, P. Kratz, V. Aji, M. Bockrath, C. N. Lau, C. Varma, R. Stillwell, D. Smirnov, F. Zhang, J. Jung, and A. H. MacDonald, Nat. Nanotech. **7**, 156–160 (2012).

[126] F. Freitag, J. Trbovic, M. Weiss, and C. Schönenberger, Phys. Rev. Lett. **108**, 076602 (2012).

[127] A. Veligura, H. J. van Elferen, N. Tombros, J. C. Maan, U. Zeitler, and B. J. van Wees, Phys. Rev. B **85**, 155412 (2012).

[128] H. Min, G. Borghi, M. Polini, and A. H. MacDonald, Phys. Rev. B **77**, 041407 (2008).

[129] J. Jung and A. H. MacDonald, Phys. Rev. B **88**, 075408 (2013).

[130] R. Nandkishore and L. Levitov, Phys. Rev. Lett. **104**, 156803 (2010).

[131] F. Zhang, J. Jung, G. A. Fiete, Q. Niu, and A. H. MacDonald, Phys. Rev. Lett. **106**, 156801 (2011).

[132] J. Jung, F. Zhang, and A. H. MacDonald, Phys. Rev. B **83**, 115408 (2011).

[133] F. Zhang, Synth. Met. **210**, 9–18 (2015).

[134] K. Sun, H. Yao, E. Fradkin, and S. A. Kivelson, Phys. Rev. Lett. **103**, 046811 (2009).

[135] F. Zhang, H. Min, M. Polini, and A. H. MacDonald, Phys. Rev. B **81**, 041402 (2010).

[136] O. Vafek and K. Yang, Phys. Rev. B **81**, 041401 (2010).

[137] O. Vafek, Phys. Rev. B **82**, 205106 (2010).

[138] R. Nandkishore and L. Levitov, Phys. Rev. B **82**, 115124 (2010).

[139] Y. Lemonik, I. L. Aleiner, C. Toke, and V. I. Fal'ko, Phys. Rev. B **82**, 201408 (2010).

[140] J. Jung, M. Polini, and A. H. MacDonald, Phys. Rev. B **91**, 155423 (2015).

[141] A. L. Grushina, D.-K. Ki, M. Koshino, A. A. L. Nicolet, C. Faugeras, E. McCann, M. Potemski, and A. F. Morpurgo, Nat. Commun. **6**, 6419 (2015).

[142] Y. Nam, D.-K. Ki, M. Koshino, E. McCann, and A. F. Morpurgo, 2D Materials **3**, 045014 (2016).

[143] C. Yoon, Y. Jang, J. Jung, and H. Min, 2D Materials **4**, 021025 (2017).

[144] J.-C. Charlier, X. Gonze, and J.-P. Michenaud, Phys. Rev. B **43**, 4579–4589 (1991).

[145] J. Jung and A. H. MacDonald, Phys. Rev. B **89**, 035405 (2014).

[146] Y. Jang, E. H. Hwang, A. H. MacDonald, and H. Min, Phys. Rev. B **92**, 041411 (2015).

[147] H. Min and A. H. MacDonald, Prog. Theor. Phys. Suppl. **176**, 227–252 (2008).

[148] F. Guinea, A. H. Castro Neto, and N. M. R. Peres, Phys. Rev. B **73**, 245426 (2006).

[149] S. Latil and L. Henrard, Phys. Rev. Lett. **97**, 036803 (2006).

[150] B. Partoens and F. M. Peeters, Phys. Rev. B **75**, 193402 (2007).

[151] X. Li, F. Zhang, Q. Niu, and A. H. MacDonald, Phys. Rev. Lett. **113**, 116803 (2014).

국문초록

그래핀의 성공적인 박리 이래로, 원자 사슬이나 원자 층이 약한 반 데르 발스 힘으로 결합된 반 데르 발스 물질에 많은 관심이 쏟아지고 있다. 반 데르 발스 물질은 층 간 혹은 사슬 간의 약한 결합 덕분에 임의의 두께의 다층 구조를 만드는 것이 가능하다. 흥미롭게도, 다층 반 데르 발스 물질은 쌓인 층 수에 따라 완전히 다른 물리적인 특징을 나타낸다. 본 학위 논문에서는 두 가지 반 데르 발스 물질 Bi_4X_4 (X=Br, I)와 버널 적층 구조를 갖는 다층 그래핀을 적층 양상에 다른 위상적 특징과 전자 간 상호작용 효과에 초점을 맞추어 다룬다.

첫 번째 부분에서는 우리는 준일차원 물질군인 Bi_4X_4를 다룬다. Bi_4X_4는 베타 상이 약한 위상 부도체가 되는 것으로 인해 처음 주목받은 물질 군으로, 최근 무기물질 데이터베이스 대규모 조사 연구에서 알파 상 Bi_4Br_4는 희소한 고차 위상 부도체로 밝혀지는 한편 알파 상 Bi_4I_4는 자명한 대칭 지시자를 가지는 것으로 밝혀졌다. 본 연구에서 우리는 기존에 알려진 것과는 다르게 실제로는 두 알파 상 모두 브릴루앙 존 전체에서 에너지 띠 간격을 갖는 한편 물질의 경계에 의존하는 힌지 상태 패턴을 나타내는 고차 위상 부도체임을 제일 원리 계산, 엣지 이합체화, 표면 격자 구조 조사, 밀접 결합 모델 설계, 그리고 경계 위상 불변량 도입과 같은 다양한 방법을 통해 보인다. 우리는 Bi_4Br_4와 Bi_4I_4의 반전 중심이 이 물질의 위상적 특징을 결정짓는 것에 있어서 핵심적인 역할을 함을 보인다. 우리는 또한 각분해능 광전자 분광 기법, 가변 게이트 수송, 주사 터널링 현미경 측정과 같은 다양한 실험을 통해 우리의 이론적 예측을 뒷받침한다. 본 물질에

대한 연구 결과는 현재 분류 범위를 넘어서서 새로운 다양한 위상 물질의 존재 가능성을 암시하는 것 외에도 원자 사슬 구조에 따른 이상적인 힌지 환경, 실온에서의 구조적 전이, 세 축 방향으로의 극도의 이방성과 같은 측면에서 새로운 위상 부도체의 패러다임을 제시하는 한편, 구조, 대칭, 위상, 그리고 상호작용을 연구하기 위한 이상적인 플랫폼이 될 수 있을 것으로 기대된다.

두 번째 부분에서 우리는 상호작용에 기인한 부분격자 대칭 붕괴 퍼텐셜로 띠 간격이 있는 상태에서 버널 적층 다층 그래핀의 상을 분석한다. 상호작용으로 인해 나타나는 이 상은 동일한 천 수를 갖지만 전하 분극 방향이 반대인 두 다른 질량을 갖는 유사스핀 쌍으로 설명된다. 수직 외부 전기장을 가하게 되면 사층 버널 그래핀에서 부분격자 유사스핀 쌍의 방향은 훈트의 규칙과 비슷한 양상으로 정렬되지만 층수가 증가함에 따라 더 복잡한 규칙을 가지는 것으로 나타난다.

주요어 : 위상 물질, 반 데르 발스 계, 박막

학번 : 2015-20342